POVM Rekentechnieken

FEM Analysis of Uplift

Author: Christian Hoffman

Version: 1.0

Date: July 2019

Title
POVM Rekentechnieken – FEM Analysis of Uplift

Projectnummer
11201267

Keywords (in Dutch)
Eindige-elementenmethode, Opdrijven, dijkversterking, HWBP, POV Macrostabiliteit, opbarsten, DIANA FEA, scheurvorming, uitknikken, drukstaaf

Summary
The current WBI regulations prescribe application of the slip-surface based *Limit Equilibrium Method* (LEM) for the slope stability analysis of primary flood defenses. The WBI regulations require that the shear strength of the cover layer in LEM analysis is reduced to zero, if the cover thickness is less than 4m and if the uplift safety factor is below 1,2. The reason for this reduction is the fear of loss of strength due to deformations and the associated geometrical nonlinear effects (buckling) during uplift, which LEM methods cannot take into account. The POVM has therefore commissioned Deltares and its subcontractors to study such behavior with the help of the *Finite Element Method* (FEM).

The report in hand describes the FEM model and the results of an embankment stability analysis for a simple case, when considering deformation effects during uplift. A number of coupled analyses of geometrical nonlinear deformations and ground water flow were executed with a development version of the finite element software DIANA. In these analyses, the interface model between the sand and the cover layer captures the special uplift behavior after the effective stress at the interface has become zero. This special behavior includes the horizontal hydraulic shortcut during gap opening and the effect of the water storage in the gap on both flow and deformations. The simple linear elastic characterization of the clay has been combined with undrained shear strength and a cracking model. A “proof of concept” was followed by analyses for three cover layer thicknesses (3m, 2m and 1 m) and by an additional sensitivity study on the influence of cover layer stiffness, permeability of the sand layer and thickness of the sand layer.

Results show that the “critical undrained clay cohesion” value, below which sliding failure occurs, lays in all cases between the upper and lower bound values as found with LEM. The upper bound has been determined by ignoring the cover layer strength contribution. The lower bound has been determined by including the cover layer strength contribution. The critical value moves more to the upper bound when the clay stiffness decreases. In most cases, the deformation mode at sliding failure of the slope involves compression of the cover layer along the uplifted zone. A combination with buckling and cracking of the cover layer was only observed for a clay thickness of 1m.

Regarding the decision rule, it seems debatable to reduce the cover layer strength in LEM abruptly to zero if the uplift safety factor is between 1,2 and 1, especially because the piezometric heads and the cover layer thickness should be schematized conservatively already. For uplift safety factors close to 1, the FEM results show that equivalent residual shear strength in LEM should mimic not only the effect of buckling/cracking but also the effect of compression, which is apparently dominant in most cases. Ignoring the residual strength contribution is on the safe side. A less conservative choice for the critical thickness or the amount of strength reduction can however not be underpinned sufficiently. The current numerical results are too limited and also not supported by physical evidence. Extended sensitivity analysis is therefore recommended, as well as further variation studies using more realistic geometries and soil layering, and also using a more sophisticated model for the clay stiffness. If such further numerical analyses would show a clear potential for less conservative choices, it is finally also recommended to compare the numerical results with the results from a physical test set-up.

Title
POVM Rekentechnieken – FEM Analysis of Uplift

Projectnummer
11201267

References (in Dutch)

- Offerte Deltares, met kenmerk 11201267-001.
- Opdrachtbrief Rivierenland, met kenmerk 2017030198/2017060568 en ordernummer 649516.

Version	Date	Author	Initials	Review	Initials	Approval	Initials
0.1	August 2018	dr. C. Hoffmann ir. M.A.T. Visschedijk		ir. A. van Hoven		ir. L. Voogt	
1.0	July	dr. C. Hoffmann ir. M.A.T. Visschedijk		ir. A. van Hoven		ir. L. Voogt	

Status
final

12 July 2019, version 1.0, final

Content

Symbols

c	Cohesion [kPa]
K_0	The ratio between the initial horizontal and vertical effective stress
p'	The isotropic effective stress (positive in tension) [kPa]
q	The deviatoric stress [kPa]
ε	Strain (positive in tension) [-]
γ	Shear strain [-]
ϕ	Effective angle of friction [°]. The ‘ superscript has been dropped for convenience
ϕ	Piezometric head [m]. Equal to pressure head plus elevation head.
ψ	Angle of dilatancy [°]
σ'	Effective stress (positive in tension) [Pa]

Abbreviations

FEM	Finite Element Method
LEM	Limit Equilibrium Method (Bishop, Uplift Van, Spencer)
MC	Mohr-Coulomb
POVM	Projectoverstijgende Verkenning Macrostabiliteit
S.F.	Stability Factor
WBI	Wettelijk Beoordelingsinstrumentarium

12 July 2019, version 1.0, final

1 Introduction

1.1 POVM project “Opbarsten”

The current WBI regulations (Ministerie van Infrastructuur en Milieu, 2016b) prescribe application of the *Limit Equilibrium Method* (LEM) for the slope stability analysis of primary flood defenses. Typically applied LEM models for this purpose are: *Bishop*, *LiftVan* and *Spencer*. The LEM searches for the slip plane position with minimal stability factor (SF), based on the shear strength along the slip plane that can be mobilized maximally at the considered stress state during high water conditions. The WBI regulations require that the shear strength of the cover layer is reduced to zero in case of a thickness less than 4 m in combination with an uplift safety factor lower than 1,2. The uplift safety factor is defined by the cover layer weight divided by the water pressure at the interface between sand and cover layer. The reason for this reduction is the fear of loss of strength in thin cover layers due to buckling, as LEM methods cannot take deformations and associated geometrical nonlinear effects into account. With advanced *Finite Element Method* (FEM) analysis however, it might be possible to study the total failure behavior during uplift numerically. The POVM has therefore commissioned Deltares and its subcontractors to study such behavior with the help of FEM analysis. This study should firstly increase the understanding of the actual behavior. Secondly, and if feasible, the study should tentatively result in a proposal for a modified decision rule for LEM analysis, based on the FEM results (product 1). If such a proposal proves to be feasible, the integration in the total safety format (product 2) and the dependencies with the piping assessment regulations (product 3) should be determined additionally, before actual implementation in practice can take place.

1.2 Objective

The report in hand is to be considered as the background report to “Product 1”. It describes the FEM model and the results of embankment stability analysis for a simple case, for which the behavior during uplift of the cover layer is studied. The objective of the reported study has been to take the geometrical nonlinear deformations into account, in order to see whether failure of the cover layer can occur premature to the occurrence of a passive failure plane through the cover layer, and if so in which cases. For this purpose, a number of coupled analyses of geometrical nonlinear deformations and ground water flow were executed. In these analyses, the interface model between sand and cover layer captures the special uplift behavior after the effective stress has become zero. This special behavior includes the horizontal hydraulic shortcut during gap opening and the effect of the water storage in the gap on both flow and deformations. The analysis was executed with a development version of the finite element software DIANA. This development version has been modified to capture the required combination of features. A “proof of concept” was therefore executed first, to check if all required features performed as expected. This proof of concept was followed by evaluation of the failure mode for three cover layer thicknesses and by executing an additional sensitivity study on the influence of cover layer stiffness, permeability of the sand layer and thickness of the sand layer.

1.3 Content

The current report comprises the following sections:

1. Initial case definition by Deltares (Chapter 2).
2. Description of the finite element model (Chapter 3).
3. Proof of Concept (Chapter 4).
4. Results for basic cases with different thicknesses (Chapter 5).
5. Results of the sensitivity analysis, with variations of cover layer stiffness, sand layer thickness and sand layer permeability (Chapter 6).
6. Conclusions and recommendations (Chapter 7).

1.4 Reference documents

The following reference documents have been used in this report:

- Base case definition (Deltares, 2017).
- DIANA User's Manual -- Release 10.2 (DIANA FEA, 2017).

2 Initial case definition

2.1 Geometry

At the start of the study, Deltares provided the following specifications for the simplified case to use for both the “proof of concept” and the follow-up (Deltares, 2017).

The case consists of a homogenous embankment, resting on a clay layer that is positioned on top of a deep sand stratum, see Figure 2.1.

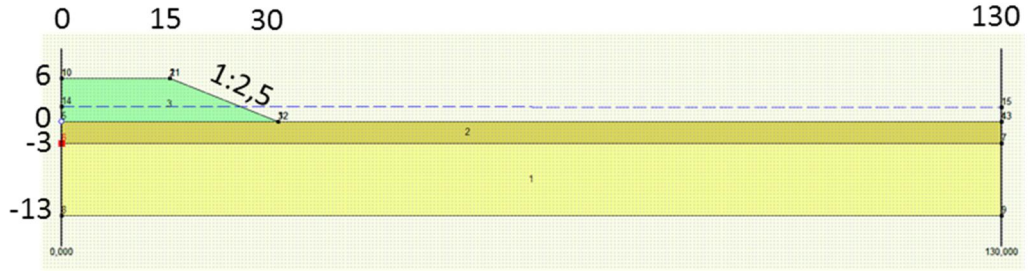

Figure 2.1 Geometry of analysis and different soil layers (dimensions in meters)

The clay in the embankment and cover layer is modelled as a homogeneous cohesive material, while the sand is modeled as a purely frictional material. The thickness of the clay and sand layers is 3m and 10m, respectively. The initial water level is at ground surface level (GWL=+0.00). The reference level is the ground surface level of the cover layer.

2.2 Materials

The material parameters for the simplified case are listed in Table 2.1.

Table 2.1 Material parameters

Material	γ (kN/m^3)	c (kN/m^2)	ϕ (°)	ν (-)	E (kN/m^2)
Embankment	17	17.5	0	0.3	3000
Clay	17	17.5	0	0.3	3000
Sand	20	0	32	0.3	10000

2.3 Hydraulic boundary conditions and properties

2.3.1 Boundary conditions

The hydraulic boundary conditions are shown in Figure 2. The piezometric heads (PR) are defined as follows:

- PR = ground surface for the top embankment and clay layer (red).
- PR = GWL (+0.00) for the right-hand side “far field” boundary (blue).
- No flow (q=0) at the bottom sand and left-hand side clay boundary (black).
- PR(t) variable in time for the sand at the left-hand side boundary (blue).

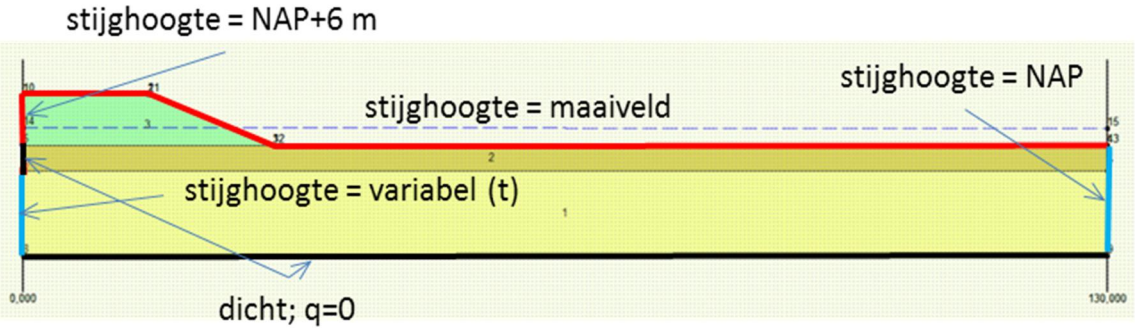

Figure 2.2 Hydraulic boundary conditions

The piezometric head at the left-hand sand boundary, PR(t), varies in time as is shown in Figure 2.3. This transient boundary condition development was derived using the '*waterstandverloop tool*', which is provided within the WBI 2017 framework. The actual curve is from a location somewhat west of the city of Arnhem.

The hydraulic boundary condition is chosen such that the uplift condition of the cover layer will occur within the high water time frame.

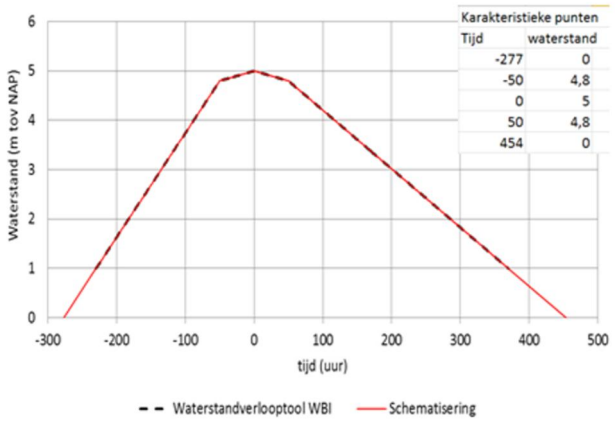

Figure 2.3 Piezometric head varying in time at the sand layer, PR(t)

2.3.2 Hydraulic properties

The applied hydraulic material properties are listed in Table 2.2.

Table 2.2 Hydraulic parameters

Material	**$k_{vertical}$ (m/s)**	**$k_{horizontal}$ (m/s)**	**Porosity n (-)**
Embankment	$1x10^{-10}$	$1x10^{-10}$	0,4
Clay	$1x10^{-10}$	$1x10^{-10}$	0,4
Sand	$1x10^{-3}$	$1x10^{-3}$	0,4

Permeability dependency on porosity was not considered in this study.

3 Finite Element Model

3.1 Introduction

For a sufficiently realistic FEM modeling, the initial case definition as provided by Deltares has been modified and extended with regard to the following aspects:

1. The geometry and boundary conditions.
2. The load transfer and hydraulic conditions at the contact between the clay and the sand.
3. The water loading in the reservoir. This loading was mimicked by schematization of the water as a material with very low elasticity, consisting almost only of pores (n=0.99).
4. Geometrically nonlinear effects were included.
5. The effect of clay cracking after exceedance of the tensile strength was included.

Details are discussed in the following sections.

3.2 Geometry

In order to get a realistic distribution of stress and water pressure, the model was extended by a reservoir on the left side of the geometry and the embankment was doubled in width, see Figure 3.1. The geometry is such that the embankment slope and cover layer and the boundary conditions in the aquifer can be regulated as required. The initial and modified (center) geometry and boundary conditions are show in Figure 3.2.

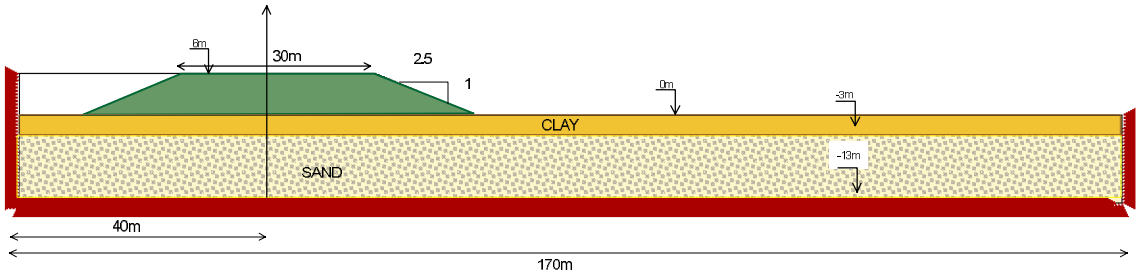

Figure 3.1 FEM schematization of geometry.

3.3 Boundary conditions

The hydraulic boundary conditions are defined according to the specifications in the Deltares simplified case.

- A constant piezometric head at the ground surface was specified at the right side (far field boundary).
- A constant piezometric head at the maximum water level (H=6m) in the reservoir was specified at the left side (reservoir)
- A varying piezometric head in the sand was specified at the left side.

The displacement boundary conditions are defined as follows:

- No displacement (vertical and horizontal) at the base and no horizontal displacement at the right and left-hand sides.

The applied hydraulic and displacement boundary conditions are shown in Figure 3.3 and Figure 3.4, respectively.

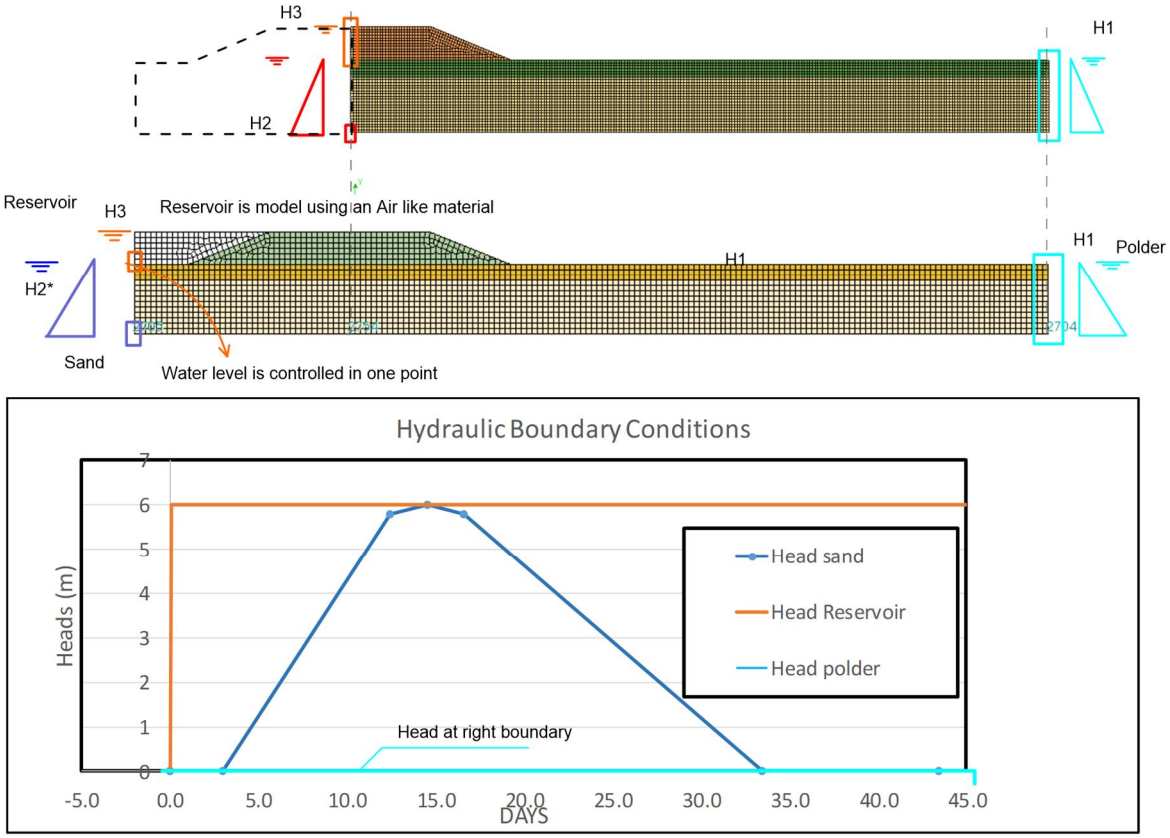

Figure 3.2 Modified geometry and boundary conditions. Top: model as provided by Deltares, Middle: model as used in this study, Bottom: Hydraulic boundary conditions

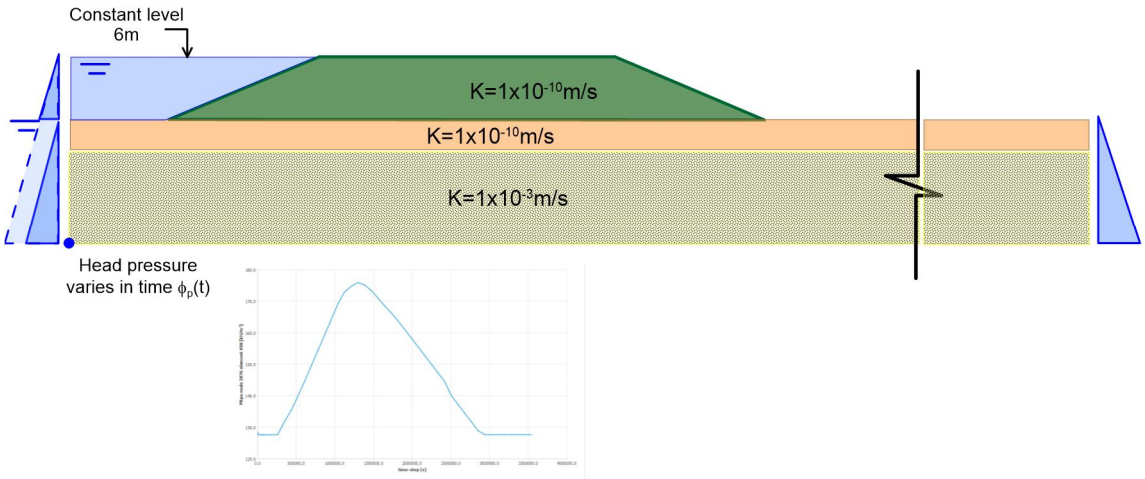

Figure 3.3 Hydraulic Boundary conditions

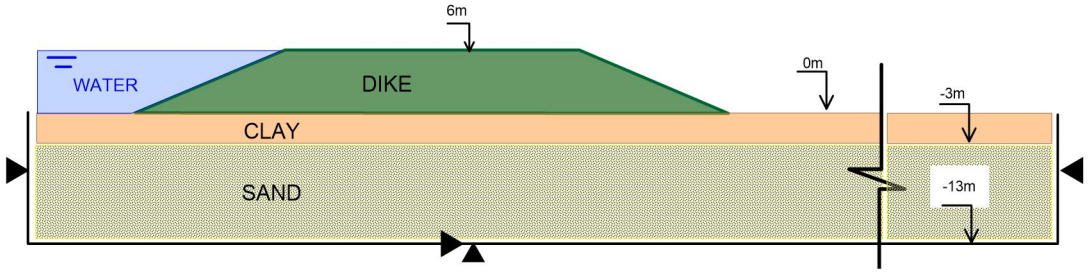

Figure 3.4 Support Boundary conditions

3.4 Mesh

The domain is meshed using quadrilateral elements with quadratic displacement interpolation functions (Element type Q16E). The element size is chosen such that there is a minimum of three elements over the thickness of the clay layer. Interface elements (Element type CL12I) are defined along the connection of sand and clay layer. Figure 3.5 shows the mesh defined for the cover layer with a thickness of 3 m.

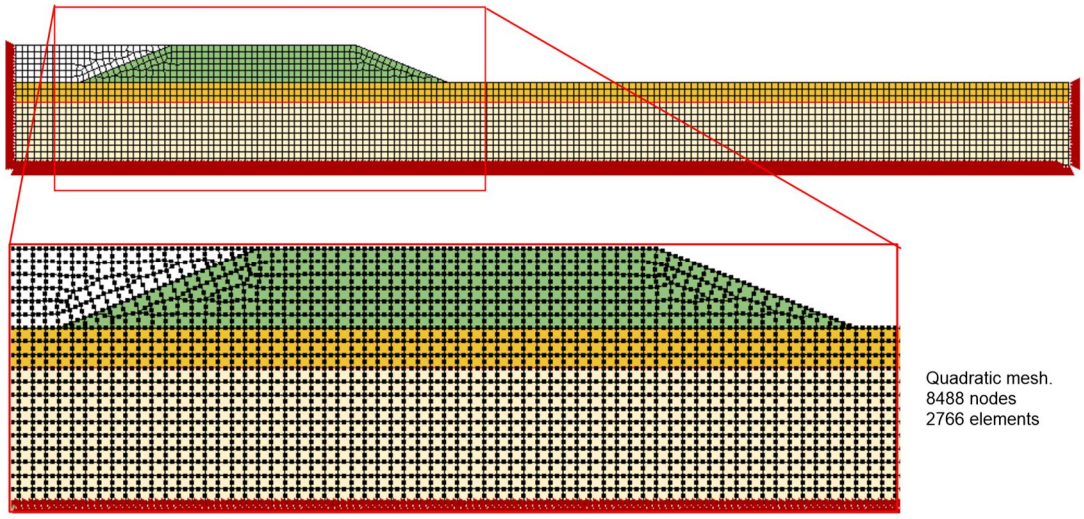

Figure 3.5 Mesh as defined for the 3m cover layer thickness

The mesh density is considered sufficiently fine to capture the relevant mechanisms of slope instability, uplift and compression of the cover layer, cracking and or buckling of the cover layer.

3.5 Phased Analysis

The applied stages are as follows (Figure 3.6):

- Phase 1: Initial conditions sand-layer and clay-layer.
- Phase 2: Embankment construction.
- Phase 3: Impounding the reservoir, applying hydrostatic loading from reservoir with no changes of pore-pressure in sand-layer. At the end of this phase the hydraulic conditions are in agreement with initial conditions defined by Deltares and depicted in Figure 2.2 and Figure 2.3.
- Phase 4: Pressure head increase in the sand-layer according to Figure 3.2.

Through the phases 1 to 3, the initial stress and pore pressure fields are constructed. The conditions of phase 3 are maintained until an almost steady state seepage has been reached. To get equilibrium (steady state) within reasonable times an increased permeability has been assumed for the clay in phase 3. The permeability values were set to the specified ones at the end of phase 3 and before applying variations in the pressure head in phase 4. The pressure head in the sand layer was increased to a maximum value of 6m in order to get a maximum pressure head around 5m at the axis of the embankment (x=0). The pressure head of 5 m at the axis of the dam was defined in the Deltares reference case. Figure 3.6 shows the evolution of the pressure head in the 4 phases.

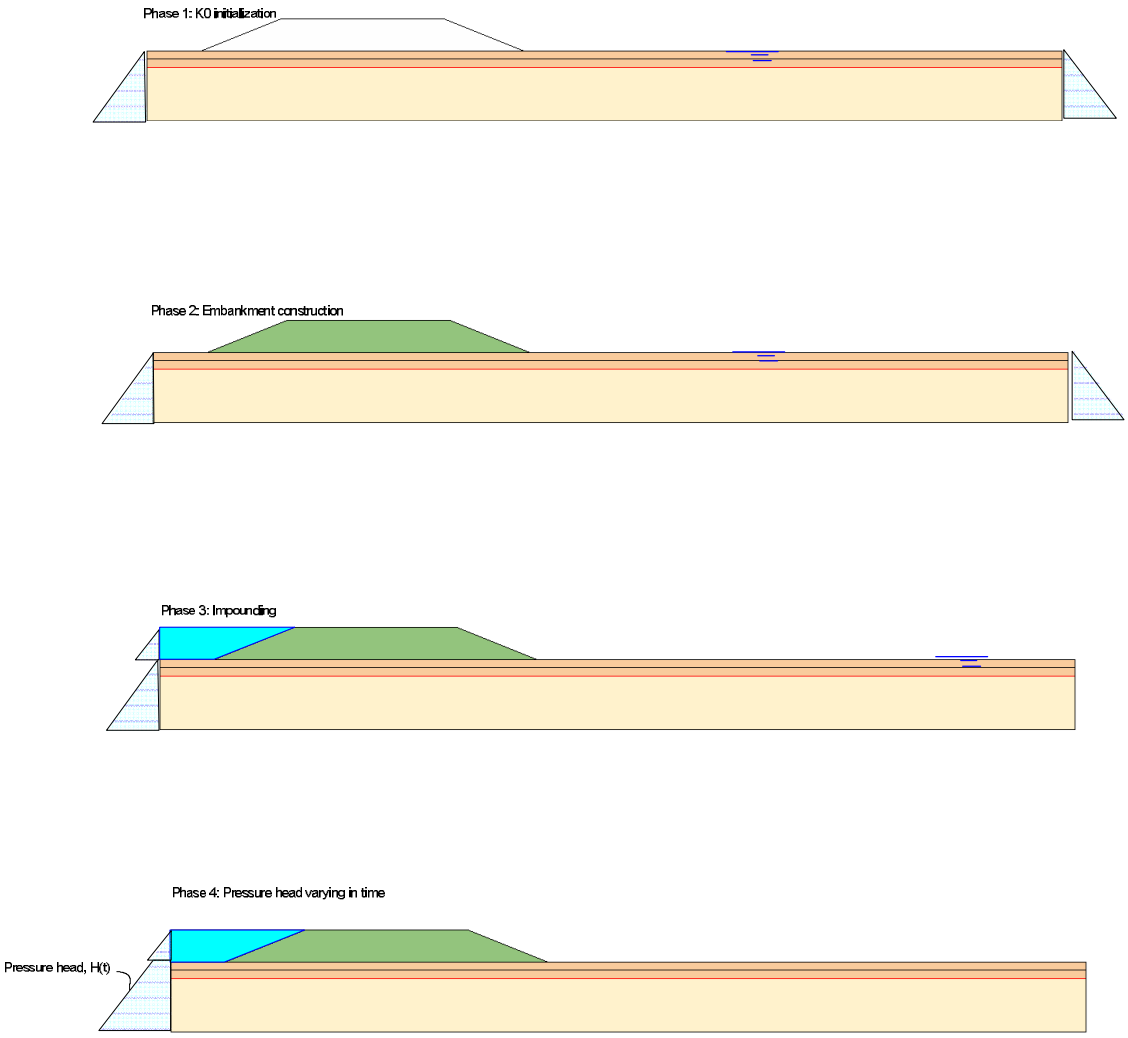

Figure 3.6 Phased analysis

Details per phase are given below.

- *Phase 1 (Day 0): Initial conditions*.
  The sand and the cover layer are considered fully saturated (GWL @ ground surface) and initial stresses are computed based on the dead weight load and the assigned K0 values.

- *Phase 2 (Day 0+): Embankment construction*.
  The embankment is placed. Initial stresses for the embankment are computed considering the dead-weight load and applying the corresponding K0 value.
- *Phase 3 (Day 0 to 3): Transient analysis (Impounding from reservoir to steady state).*
  The water level in the reservoir is increased and seepage is computed, until an almost steady state ground water flow state is reached.
- *Phase 4 (Day 3 to 43): Pressure head changes @ bottom sand.*
  The pressure head in the sand layer at the left-hand side boundary is varied in time, according to the diagram shown in Figure 3.7.

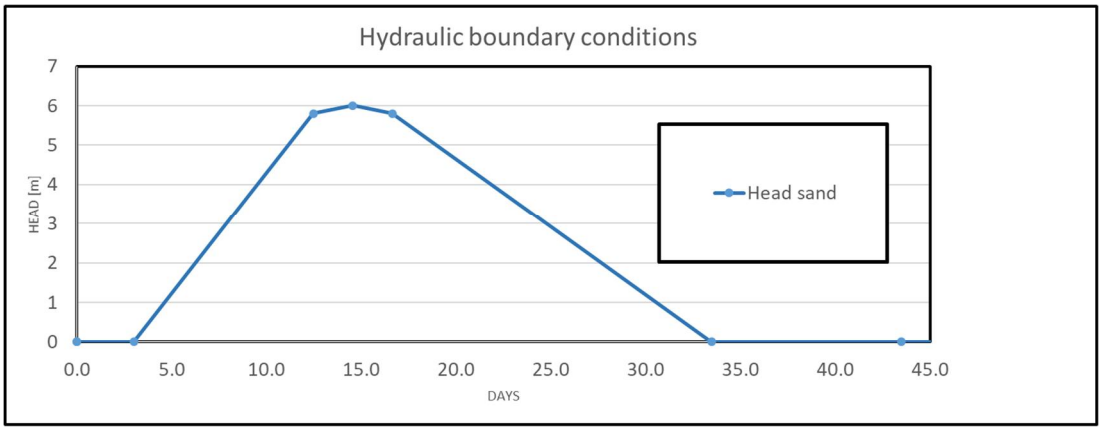

Figure 3.7 Evolution of the piezometric head in the sand layer at the left-hand side boundary

3.6 Material modeling

3.6.1 Pore pressures

The fully coupled Hydro-Mechanical formulation in DIANA has been used, see Chapter 72 of the DIANA User's Manual (DIANA FEA, 2017). This means that the calculated pore pressures will affect the displacements and vice versa. It means also that the calculated pore pressures will affect the soil strength if the shear strength depends on effective stress. Table 2.1 shows that this applies only for the sand (shear strength defined by friction angle) and not for the clay (shear strength defined by cohesion).

3.6.2 Shear strength of clay and sand

The actually applied cohesion value for the clay has been chosen differently per cover layer thickness. The applied value equals the (iteratively determined) largest cohesion value at which slope instability will occur. The derived "critical" cohesion values vary in the basic cases between 14 kPa for a thickness of 1m to 17.5kPa for a thickness of 3m. See § 5.5 for a comparison of the derived "critical" values of cohesion in combination with the head at which failure occurs for the FEM and LEM analysis.

Application of the K0 initialization procedure requires in DIANA the use of a Mohr Coulomb model for both the sand and the clay. The Mohr-Coulomb model in DIANA requires furthermore a positive (non-zero) friction angle ϕ. Therefore, a small value of 3º has been applied, in deviation of the Deltares specification of a zero friction angle. The dilatancy angle ψ has been chosen equal to 0º.

3.6.3 Coulomb friction at the interface between clay and sand

A Coulomb friction model has been applied at the interface between clay and sand. The interface friction angle has been chosen equal the friction angle of sand, with zero cohesion and zero dilatancy angle. When the interface opens, the shear strength is reduced to zero.

3.6.4 Cracking of clay

When the cover layer is uplifted, tensile stresses will appear in different zones of the clay. These zones are indicated with red-double sided arrows in Figure 3.8.

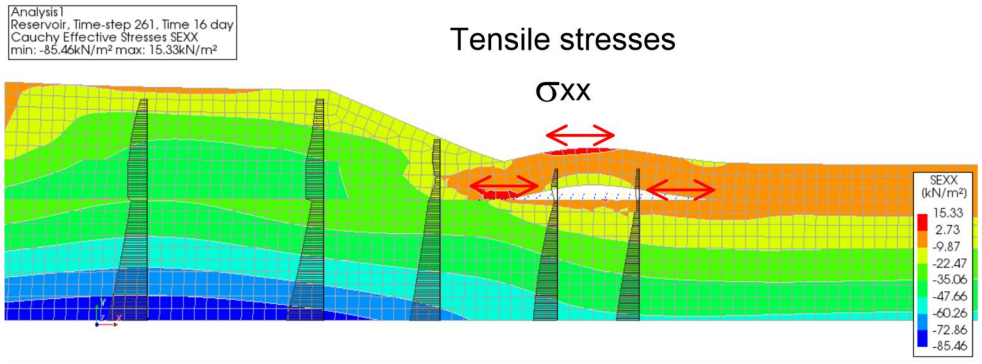

Figure 3.8 Tensile stresses occurring in the soil induced by the uplift (Tension stress=positive)

In order to account for the limited tensile capacity of the clay, DIANA's multi-directional fixed crack model with tension softening has been applied, in combination with the Mohr-Coulomb shear-failure criterion.

To highlight the differences in the behavior predicted with the conventional cut-off (plasticity) and with the softening cut-off (cracking), two elementary tests were executed. In these tests, a pure tensile stress-condition was defined and the corresponding stress-displacement curves were computed. Figure 3.9 shows the stress-displacement curves computed in tensile tests when using a conventional cut-off (no softening) and when using a multi-directional fixed crack model with strain-softening. In the analyses a limited tensile strength of 3 kPa was used. This is low compared to experimental tensile strength values as found in literature (Ávila, 2004; Tang, Pei, Wang, Shi, & Li, 2015).

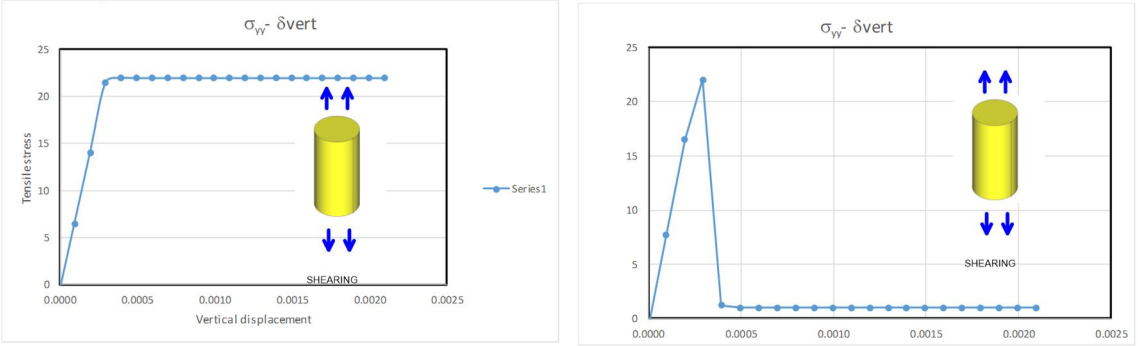

Figure 3.9 Stress-strain curves computed with conventional cut off and with softening on the tensile strength

The combined tensile and shear yield surfaces in the p-q plane are depicted in Figure 3.10. As indicated before, the shear yield surface is assumed to have an almost pure cohesive character, with a small value for the internal friction angle of 3°.

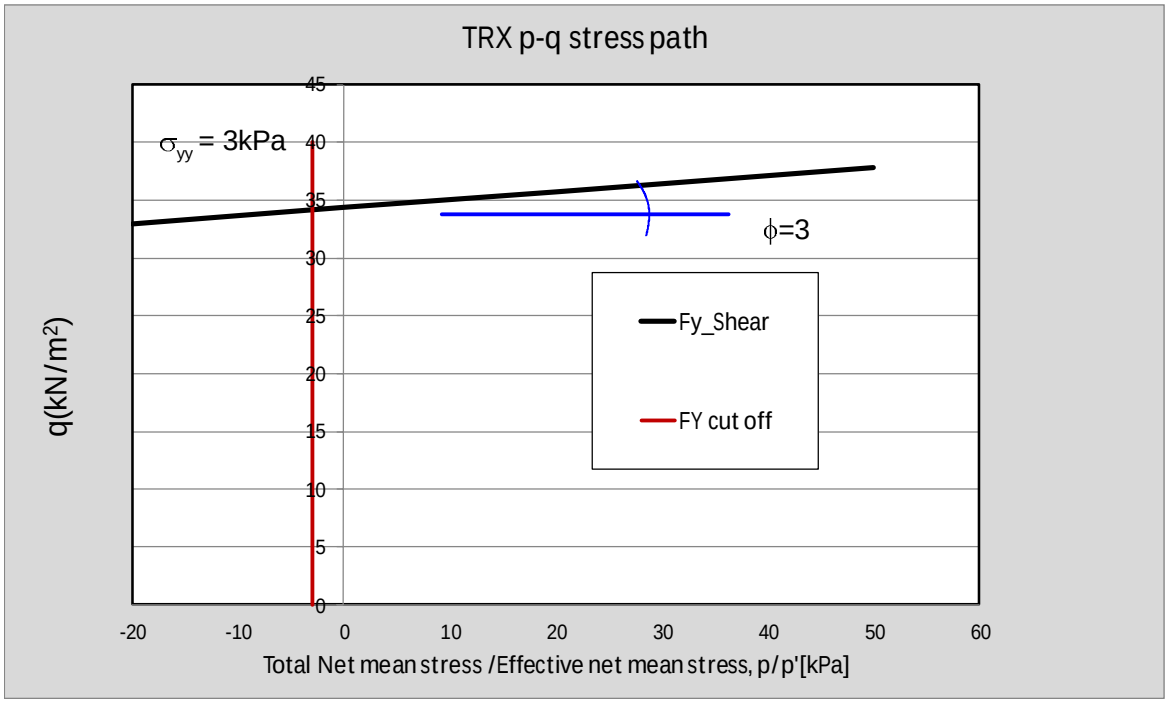

Figure 3.10. Yield surfaces for the clay material in the graph of deviator stress q versus mean effective stress p', in case of a cohesion value of 17,5 kPa

3.6.5 Overview table

Table 3.1 summarizes the applied material parameters for the different soil types.

Table 3.1 Overview of the applied material parameters

Material		Density	Cohesion	Internal Friction angle	Saturated Initial permeability	Young Modulus	Poisson (*)	Initialization	Cut off (Tensile limit)
		γ	c'	ϕ'	k	E	ν	K0	
		kN/m3	(kN/m2)	(o)	m/sec	MN/m2			[kPa]
1	sand	20	0	32	10^-3	10	0.30	0.40	0
2	dike	17	14 to 17.5	3	10^-10	3	0.30	0.40	3
3	clay	17	14 to 17.5	3	10^-10	3	0.30	0.40	3
4	Interface		0	32	kvert=10^-3 kh=0 /100 *Kv				

4 Proof of concept

4.1 Potential failure modes

A first series of computations has been performed for an initial proof of concept. The main purpose of these computations was to investigate if DIANA can capture all relevant failure modes of the embankment. All these modes involve slope instability, with a curved (almost circular) slip surface in the embankment. The following failure modes are distinguished in the cover layer, see also Figure 4.1:

1. Passive failure in the cover layer, starting at the toe of the embankment. No major uplift in the cover layer is produced. Sub-types 1a and 1b consider different shapes of the passive shear plane (circular and wedge, respectively).
2. Uplift next to the toe of the embankment. The cover layer is able to bridge the force along the “uplifted” zone. The passive failure occurs some distance from the toe.
3. Tensile cracks develop in the cover layer, induced by uplift displacements. The bending limit capacity of the clay is reached and buckling/cracking failure occurs prior to the occurrence of type 1 or 2 failure modes.
4. The cover layer is compressed by the sliding embankment and failure associated to the compressive deformations occurs along the cover layer, prior to type 1 or 2 failure modes occurring. No or minimal “uplift” is produced at failure.

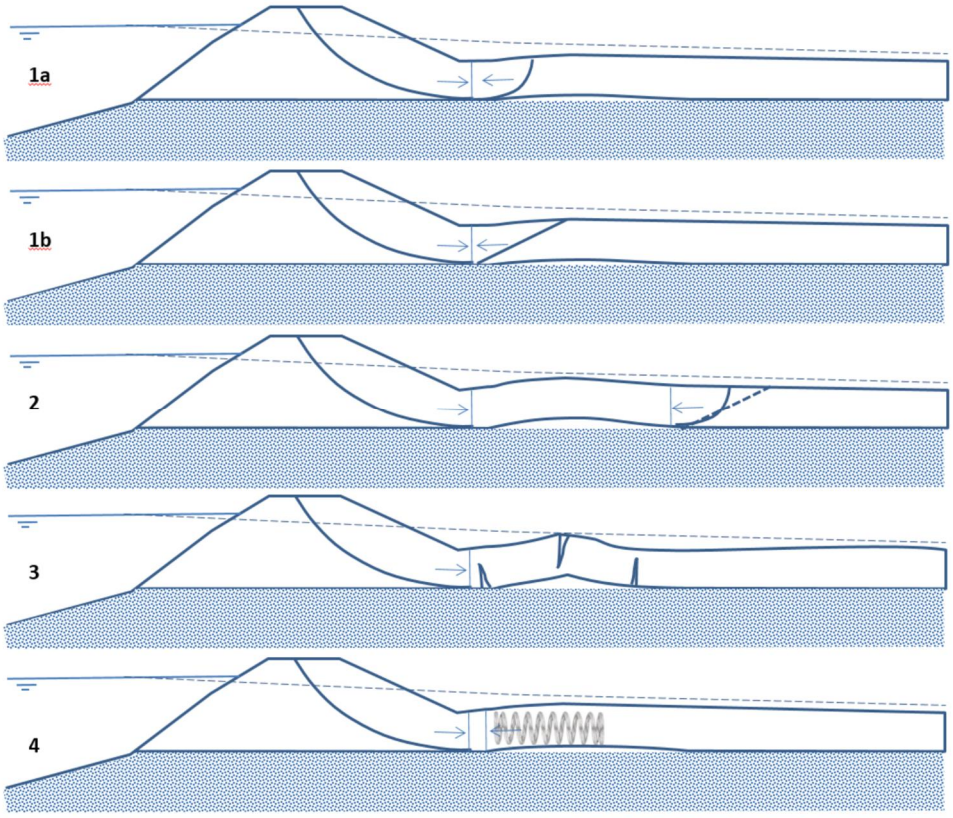

Figure 4.1 Failure mechanisms considered for the proof of concept analyses

Type 1 and 2 failure modes are covered by the current LEM analyses with calculation methods Bishop, LiftVan and or Spencer. The fear that other failure modes will occur prior to modes 1 or 2 is the reason for reducing the shear strength of thin cover layers under uplift conditions to zero in LEM analysis. The initial scope involved only mode 3. During the cause of the project was found however that mode 4 is also of importance. The “proof of concept” will therefore show that both type 3 and 4 can be modelled using FEM analysis.

In this study, the cover layer thickness and the strength parameters of the clay materials (cohesion) are varied in order to investigate the model capabilities to reproduce the mentioned failure modes. Further, some additional special features are included in the model to provide a more realistic representation of the different physical phenomena present in the problem.

4.2 Slope instability and compression of the cover layer (type 4)

Figure 4.2 and Figure 4.3 show the results of the model with a cover layer of 3m thickness and a clay cohesion equal to 17.5kPa. The analysis with these values results in slope instability, combined with high elastic compression deformations in the cover layer, with minor uplift.

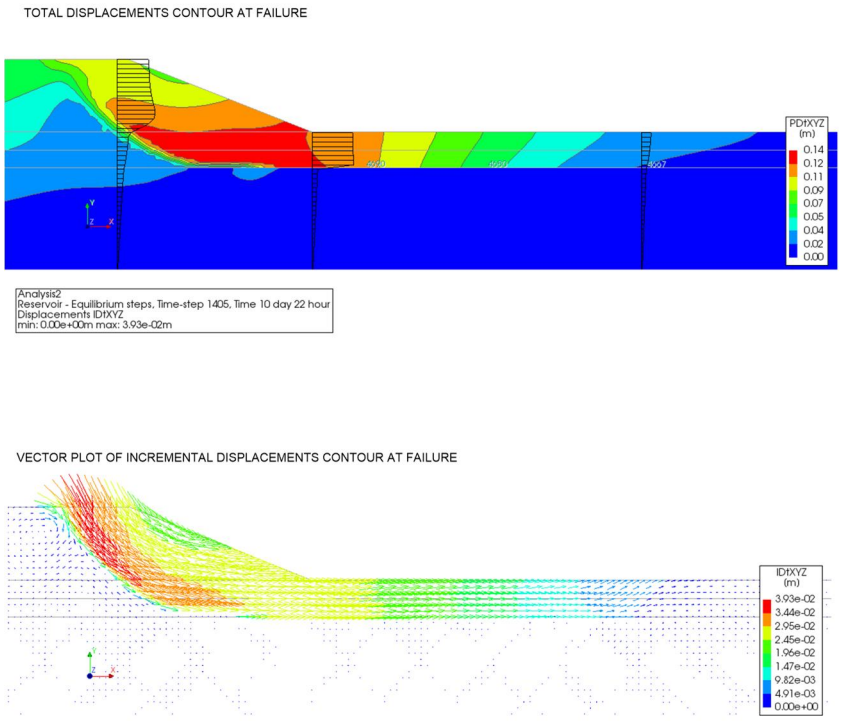

Figure 4.2 Total displacements contour at failure (top) and vector plot of incremental displacements at failure (bottom)

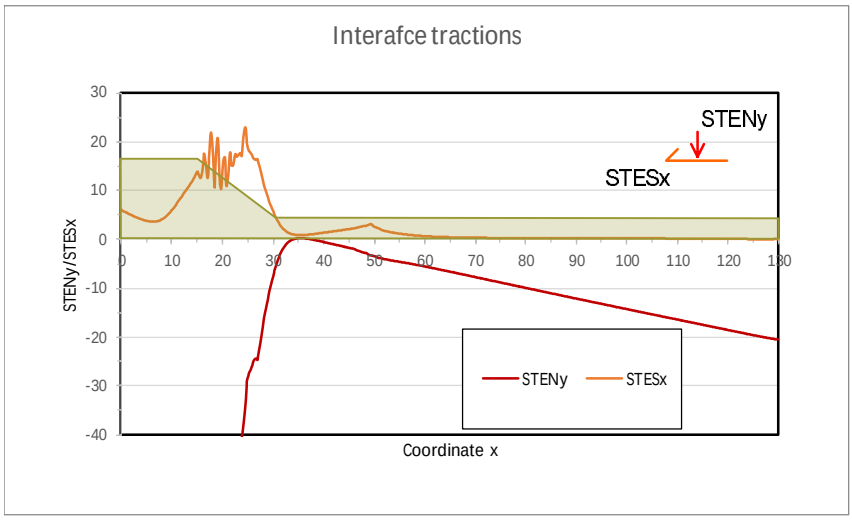

Figure 4.3 Effective stresses along the interface sand-clay. STENy is the normal effective stress/traction in the interface and STESx is the shear stress in the interface

4.3 Uplift without slope instability (type 3)

Results for the model with a cover layer of 2m and a cohesion value of 18kPa are shown in Figure 4.4. In this analysis, failure occurs due to the limited capacity of the cover layer in resisting uplift actions. Failure occurs when the bending capacity of the clay-layer is exceeded and equilibrium can no longer be computed. Figure 4.5 shows the deformed shape at failure and the horizontal effective stresses at the top and bottom of the cover layer. It is observed that the tensile capacity of 3kPa is reached at the top of the cover layer and locally at the bottom of the cover layer under the toe of the slope. Here, the tensile capacity is reached along a length of 10m at the top of the cover layer. Note that the tensile limit of 0kPa is also reached at the top of the sand layer. Note also that the embankment slope remains stable, and in this case does not need the support of the cover layer.

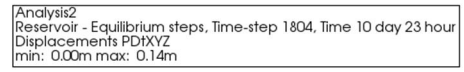

TOTAL DISPLACEMENTS CONTOUR AT FAILURE

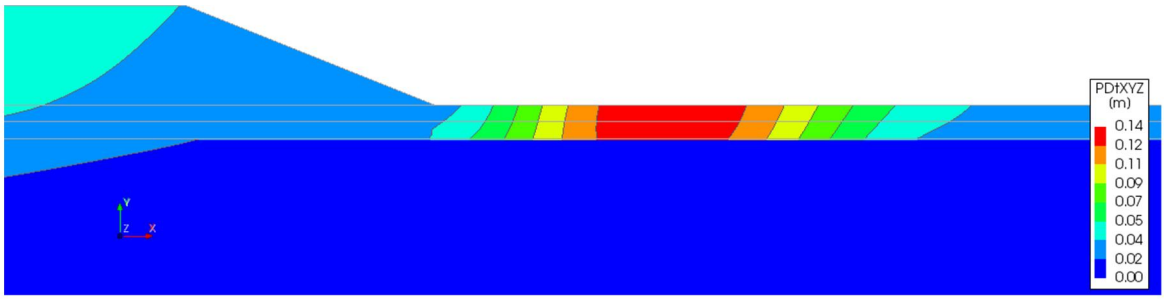

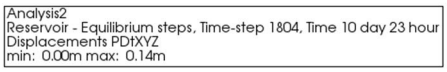

VECTOR PLOT DISPLACEMENTS AT FAILURE

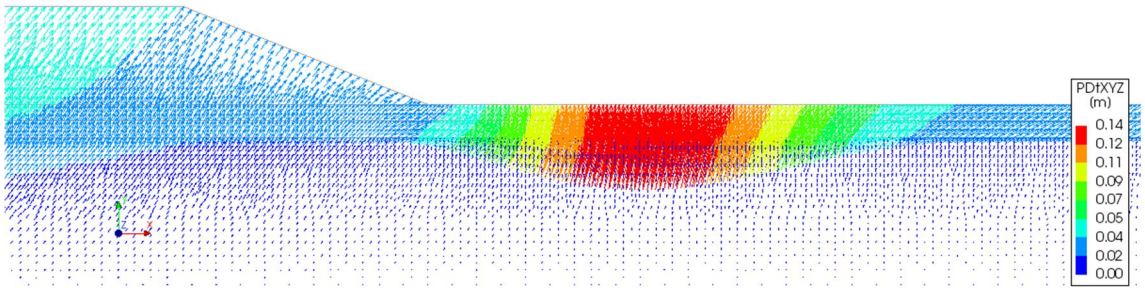

Figure 4.4 Local failure mechanism occurring for a cover layer with a thickness of 2m and a cohesion of 18kPa. Contour of total displacements (top) and vector displacements at failure (bottom).The displacements are plotted with the top of the arrow at the position of the node

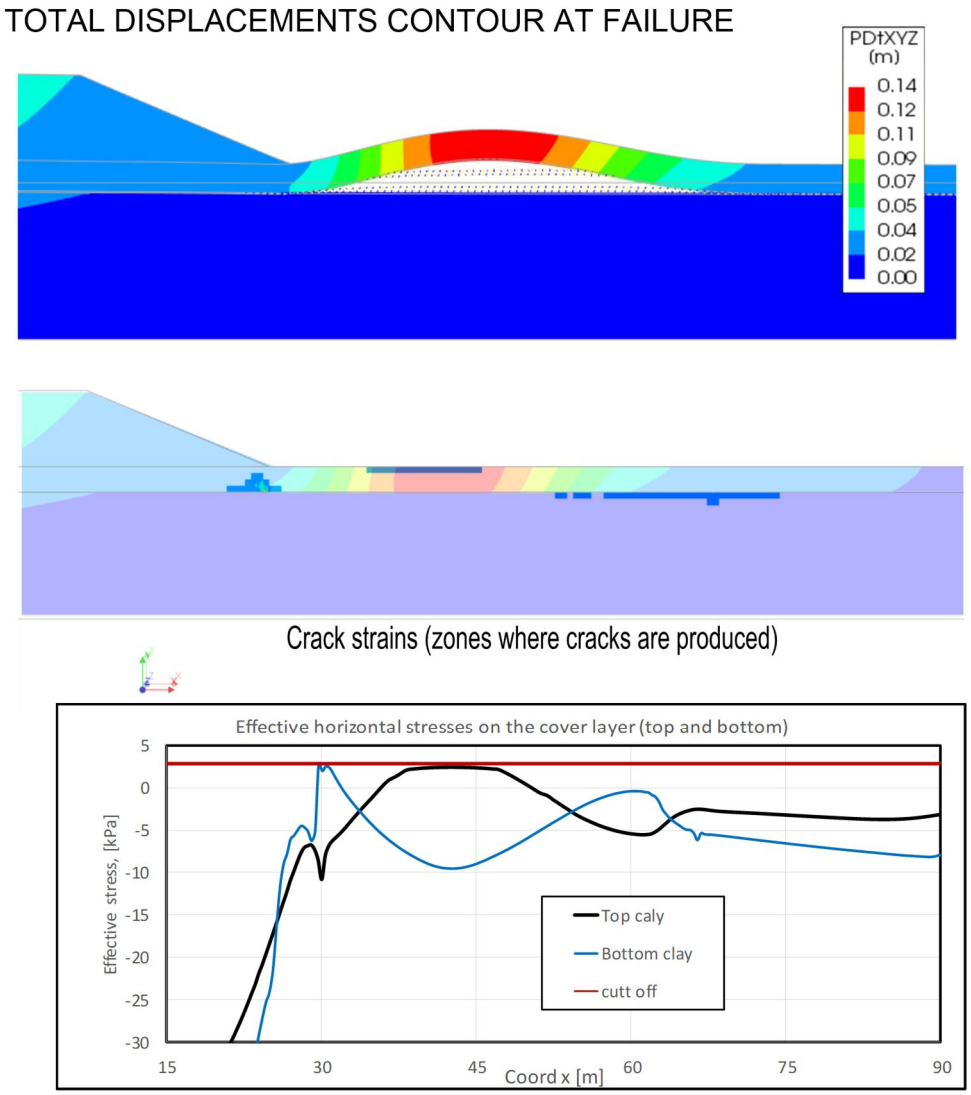

Figure 4.5 Local failure mode computed for a cover layer=2m and a cohesion of 18kPa. Effective horizontal stresses just after failure. Contour plot (top) and stresses at top and bottom of cover layer (bottom)

4.4 Uplift with slope instability (type 3)

Results considering a cover layer of 1m thickness and a cohesion value of 14kPa are shown in Figure 4.6. In this case, a combination of uplift failure and slope instability is observed. As the pressure head increases, the cover layer is lifted, and a rapid increase in the vertical displacements is observed. During this phase, no major horizontal displacements are found. As the cover layer continues to deform in bending, the tensile strength of the clay is reached, and slope failure is triggered. This is shown in the incremental displacement vector plot in Figure 4.6. The effective horizontal stresses in the clay layer prior to failure are shown in Figure 4.7.

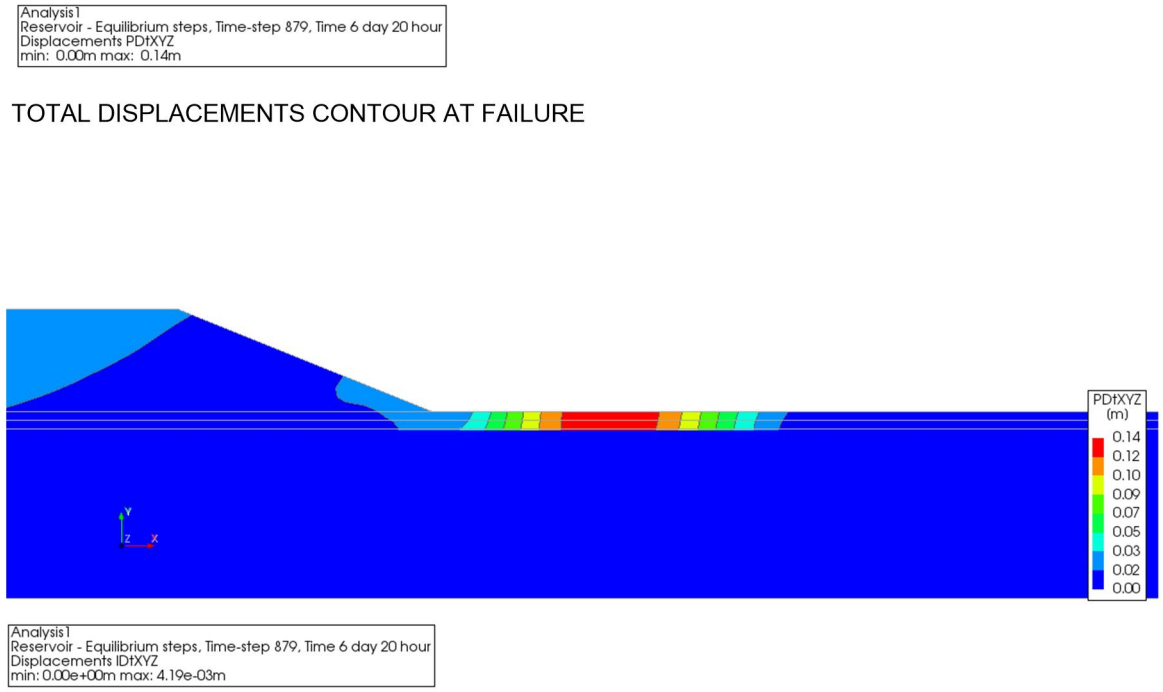

Figure 4.6 Combined failure mode computed considering a cover layer thickness=1m and a cohesion of 14kPa. Total displacements contour (top) and incremental displacements vector plot at failure (bottom). The incremental displacements are plotted with the top of the arrow at the position of the node. Downward incremental displacement of the cover layer close to the toe changes to upward incremental displacement further from the toe. Uplift and cracking occurs prior to slope instabiliy

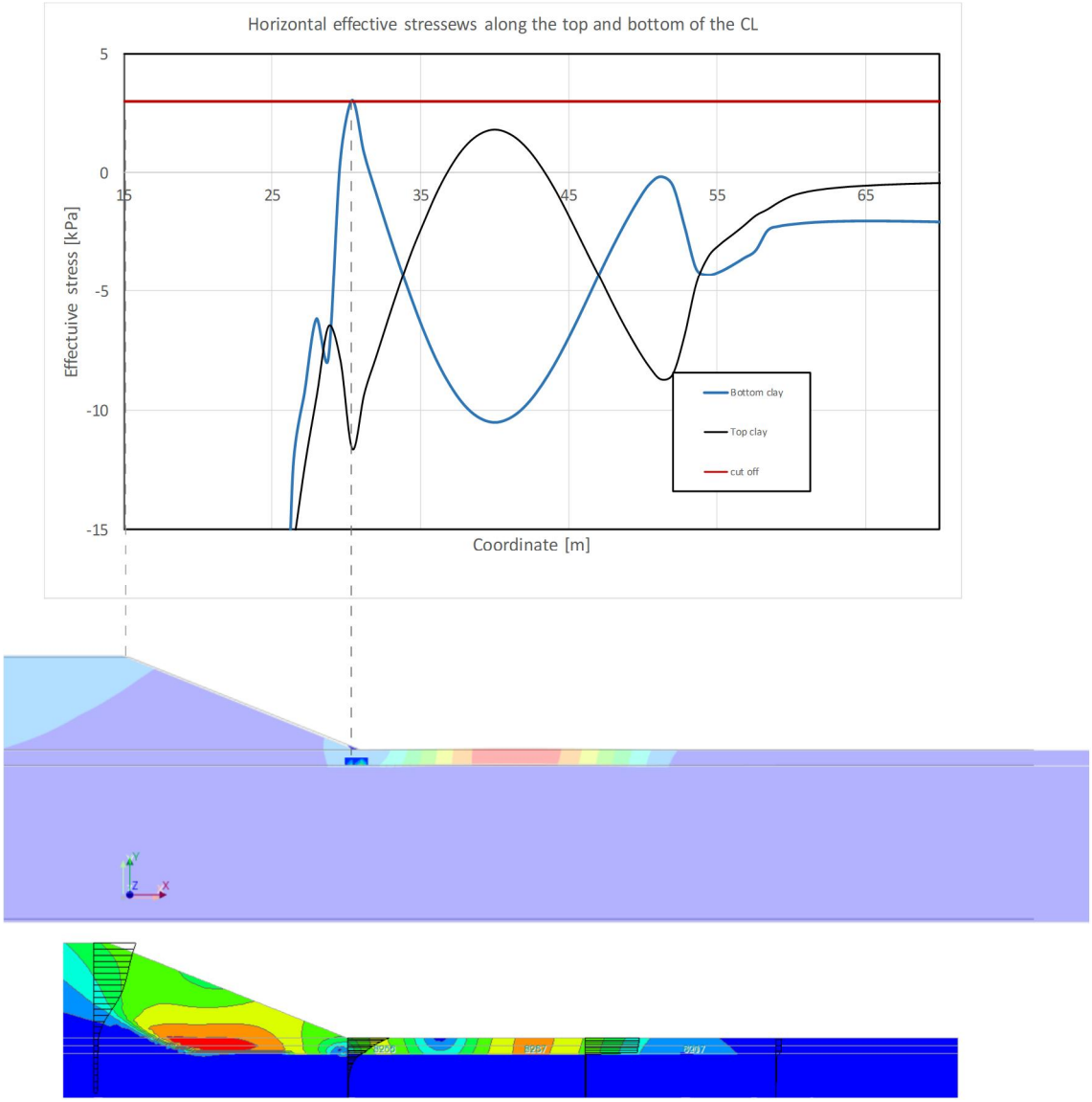

Figure 4.7 Incremental displacements contour and horizontal effective stresses at failure corresponding to a combined failure mode. The clay zone where the tensile limit is reached is also indicated (middle contours)

4.5 Special model features

A series of special features has been used to provide a sufficiently realistic representation of the different physical phenomena. In the following sections these special features are described for the case with a cover layer thickness of 3m. The different aspects are incorporated sequentially and the effect on stability is inspected.

4.5.1 Geometrical nonlinearity

When the pore pressure below the cover layer increases beyond the total vertical stress at the base of the clay, the cover layer is detached from the sand and “uplift’ occurs. The pressure head below the clay, the weight of the cover layer and its elastic modulus are main factors controlling the vertical uplift displacements of the cover layer. In Figure 4.8 the vertical displacements are

presented, as computed for clay materials with different Young modulus. It is observed that the vertical displacements increase for low values of the elastic modulus.

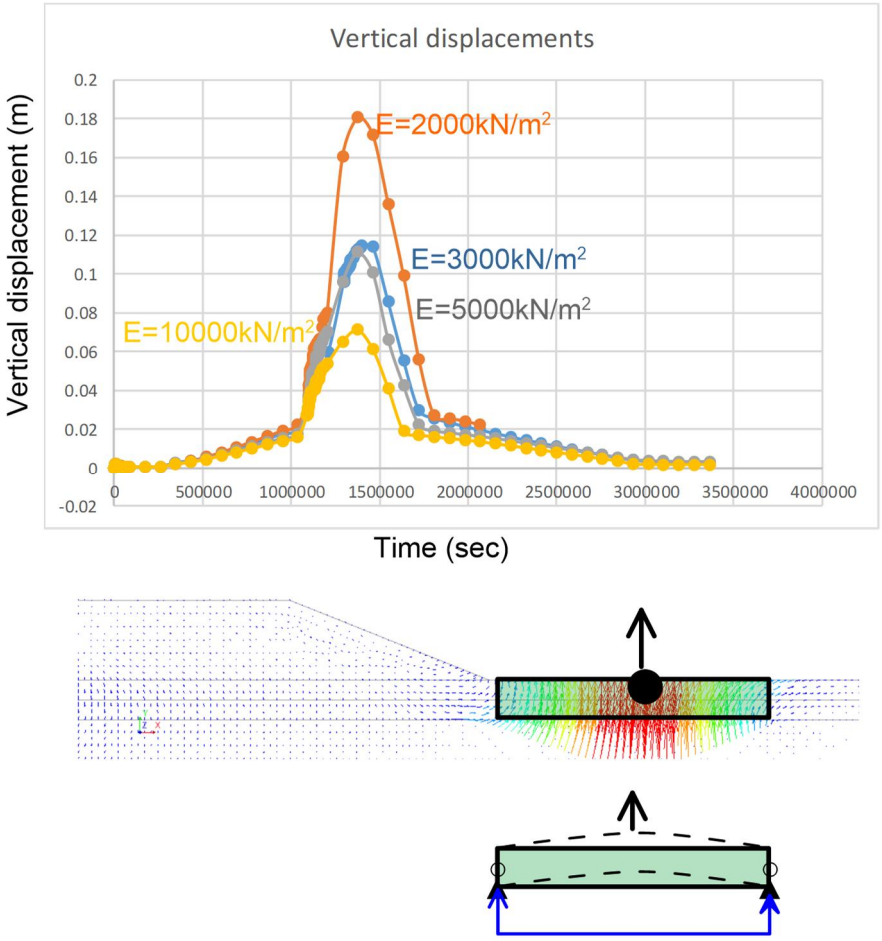

Figure 4.8 Computed upward displacements in a point located at ground surface in the "uplifted" zone. Effect of varying the elastic modulus on upwards displacements

In relation to the uplift displacements, a second order effect from the vertical displacements to the horizontal forces acting on the clay must be considered. A schematic representation of this effect is presented in Figure 4.9, where the cover layer is considered as a beam of length L (= uplifted length subjected to the upward action of the water) and compressive axial forces coming from the slope.

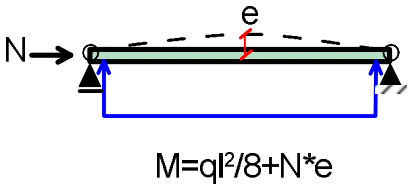

Figure 4.9 Schematic representation of the section of clay layer subjected to bending

To investigate these “geometrical nonlinear effects”, a series of computations were performed with and without geometrical nonlinearity. In a geometrically non-linear computation, the stresses and strains are calculated based on the deformed shape. A Total Lagrange formulation was used. Compared to “Updated Lagrange”, a “Total Lagrange” formulation is applicable as long as the geometrical nonlinear behavior involves merely the nonlinear effect by large displacements and rotations (as in buckling), and not so much the nonlinear effect by large strains (as in confined compression).

4.5.1.1 *Effect on deformation*

In this case the strength parameters of the clay were defined with a cohesion of 22kPa, in order to prevent either local or global failure. Vertical displacements computed without and with geometrical non-linear formulation are presented in Figure 4.10. It is observed that including the geometrical nonlinear effects results in an increase in the upward displacements of the cover layer.

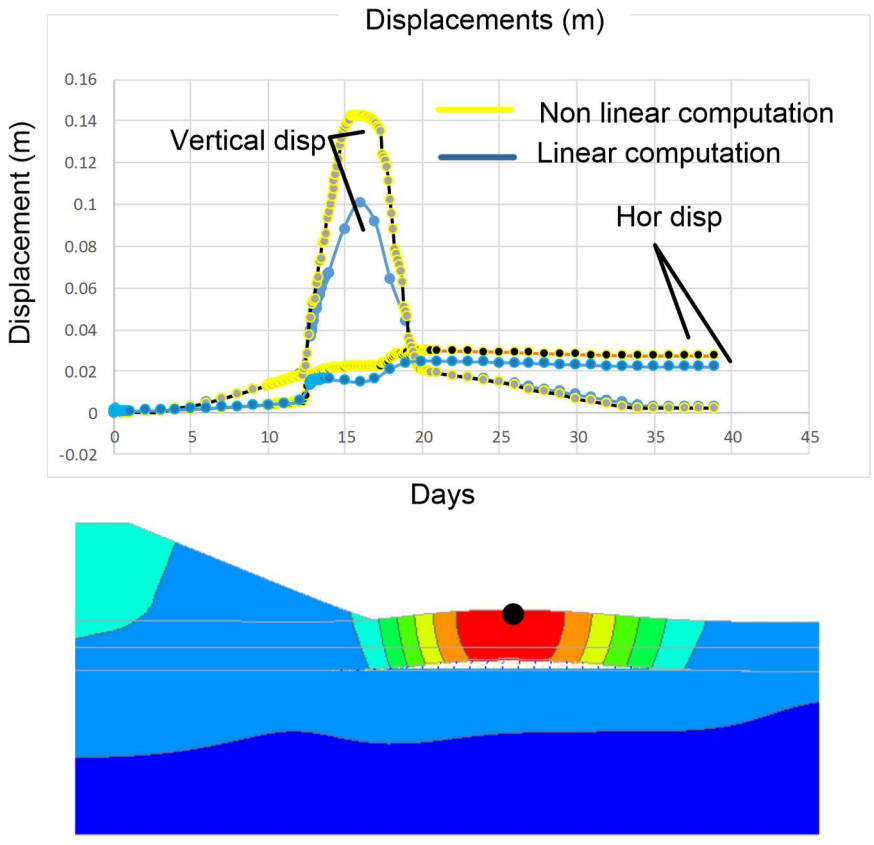

Figure 4.10 Vertical and horizontal displacements at the top of the cover layer, computed with and without the geometrically non-linear formulation

4.5.1.2 *Effect on failure*

In the second analysis, cohesion is reduced to 18kPa in order to induce failure. It is observed that the geometrically non-linear formulation results in an increase in the vertical displacements but also results in failure, which was not triggered when geometrically non-linear formulation was not

considered. Figure 4.11 shows the evolution of vertical and horizontal displacements computed and the displacements contours corresponding to the maximum displacement.

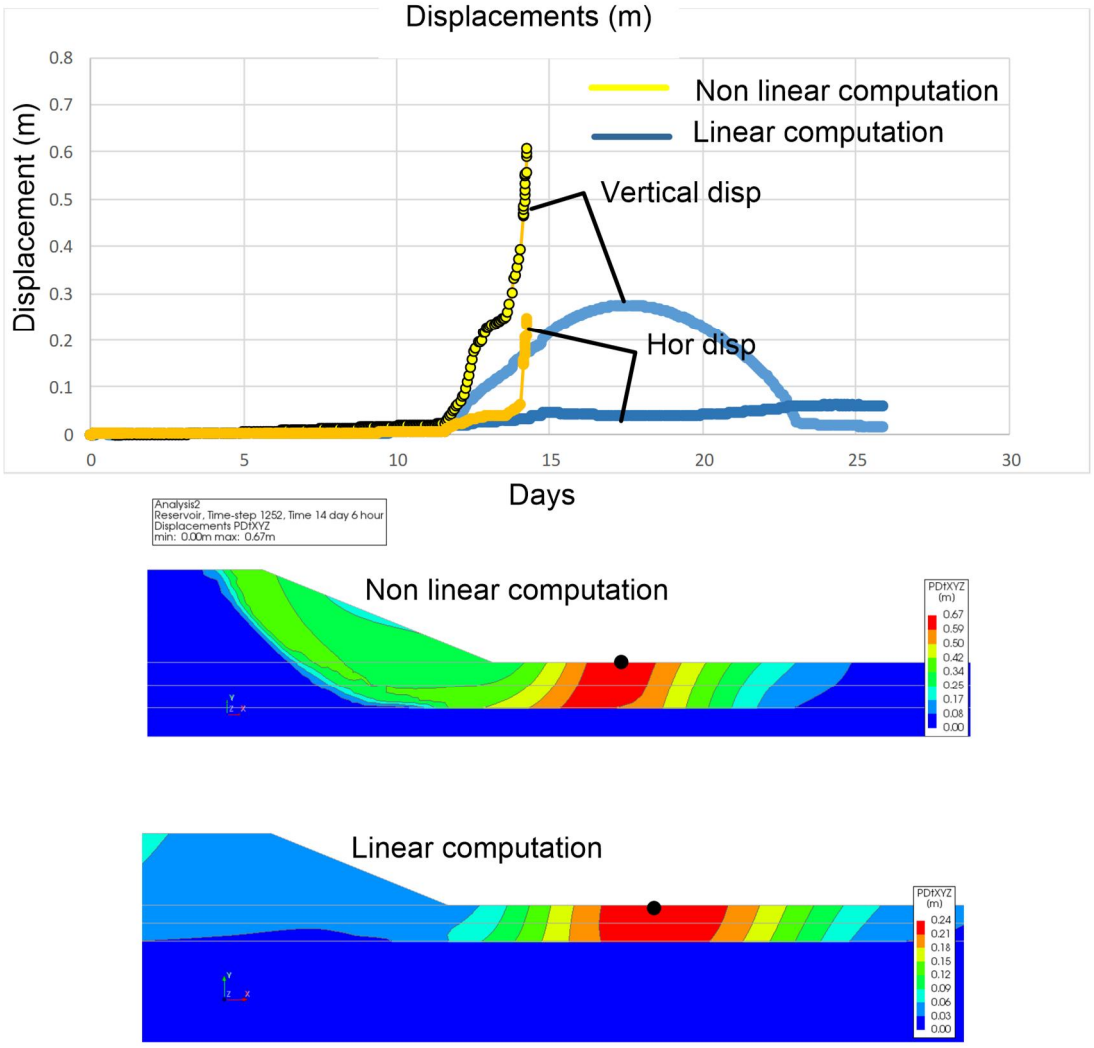

Figure 4.11 Displacements computed, with and without geometrically non-linear formulation

4.5.2 Horizontal flow along the interface gap

In the first set-up of the interface model, the water flow could only occur in the vertical direction, normal to the interface between the clay and the sand. Therefore, no longitudinal (horizontal) flow in the gap was considered. In order to provide a sufficiently realistic representation of the flow in the "uplift" zone (the zone with a gap between the clay and the sand), an extended model was implemented in DIANA. This extension considers two different situations:

(i) Closed interface, where no horizontal flow is assumed.
(ii) Open interface, where horizontal flow along the interface is taken into account.

The flow conditions are changed from closed to open as soon as the gap size becomes larger than a threshold value (b0), which has been chosen equal to 3mm. A schematic formulation of the model is shown in Figure 4.12.

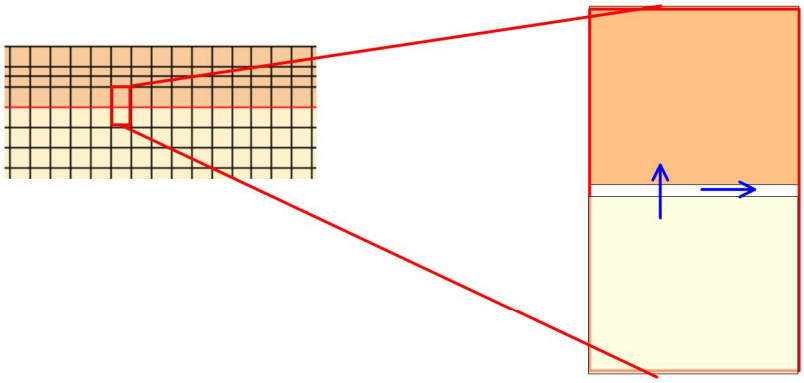

Kn: Permeability normal to the interface

Kt: Permeability along to the interface

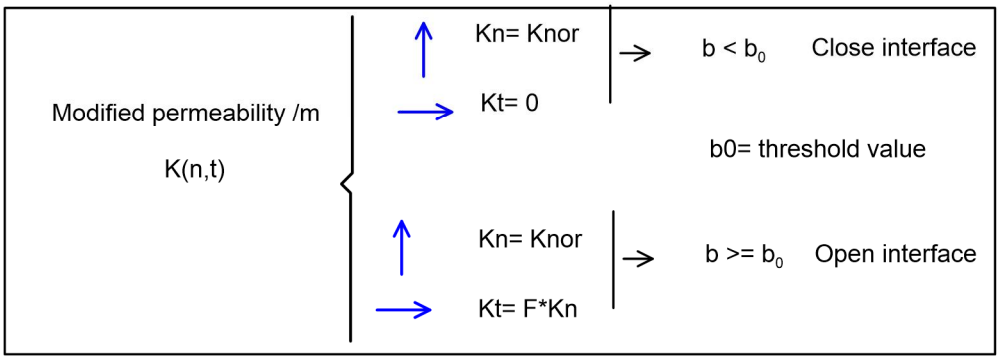

b0= threshold value defining the "opening"condition (b0=3mm)
F: multiplication factor. Assumed to be 100

Figure 4.12 Conceptual schematization of the applied interface model. Kn is the permeability of the interface in normal (vertical) direction. Kt is the permeability of the interface in tangential (horizontal) direction

4.5.2.1 *Effect on the flow pattern*

The flow pattern and the pressure head in the sand are affected by the changed flow conditions along the gap. This results in a “quiet zone” (constant head) immediately below the open interface, with the open part of the interface acting as a “hydraulic shortcut”. This zone extends to at least half the sand layer. The top part of Figure 4.13 shows the flow pattern for cases not considering flow along the interface. The bottom part of Figure 4.13 shows the flow pattern when including the effect of flow along the interface. Figure 4.14 shows pore pressure along horizontal lines located at top, middle and bottom of the sand layer in case of the “hydraulic shortcut” by an open interface. These graphs show that there is no horizontal pressure gradient close to the aquifer, whereas lower in the sand the pressure gradient increase gradually.

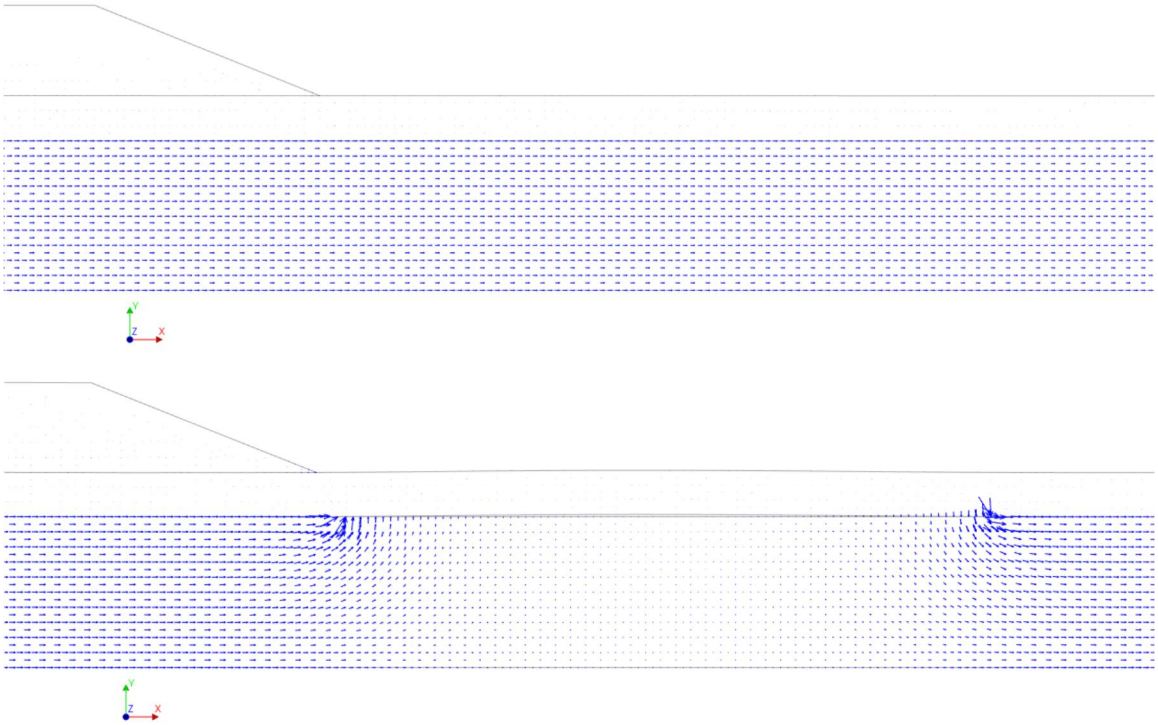

Figure 4.13 Top: Flow pattern computed without the horizontal hydraulic shortcut. Flow occurs only in the direction normal to the interface. Bottom: Flow pattern computed with the horizontal hydraulic shortcut along the open part

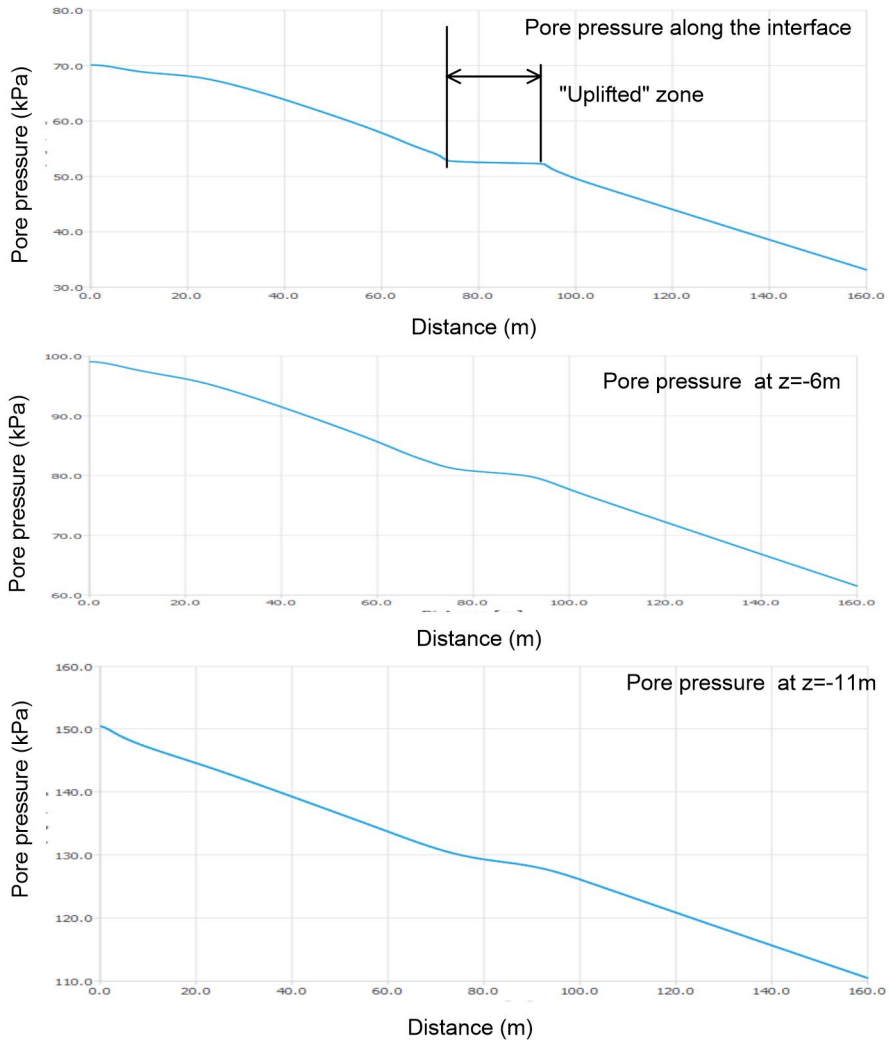

Figure 4.14 Pore pressure along different horizontal lines in the sand layer, in case of a hydraulic shortcut along the open part of the interface (the uplifted part of the cover layer)

4.5.2.2 Effect on displacements

When comparing results for displacements for the model with and without the horizontal hydraulic shortcut in the open part of the interface, is observed that high displacement rates are computed in the case where no horizontal flow is allowed (yellow series in Figure 4.15).
Figure 4.15 shows the evolution of the displacements (horizontal and vertical) for both cases and the contour plot of the incremental displacements at failure. Failure occurs for both cases closely to the maximum head value in time in the sand layer. In case of no horizontal flow along the interface however, failure is computed before reaching the maximum head value, whereas it computed after reaching the maximum value in case of horizontal flow allowed.

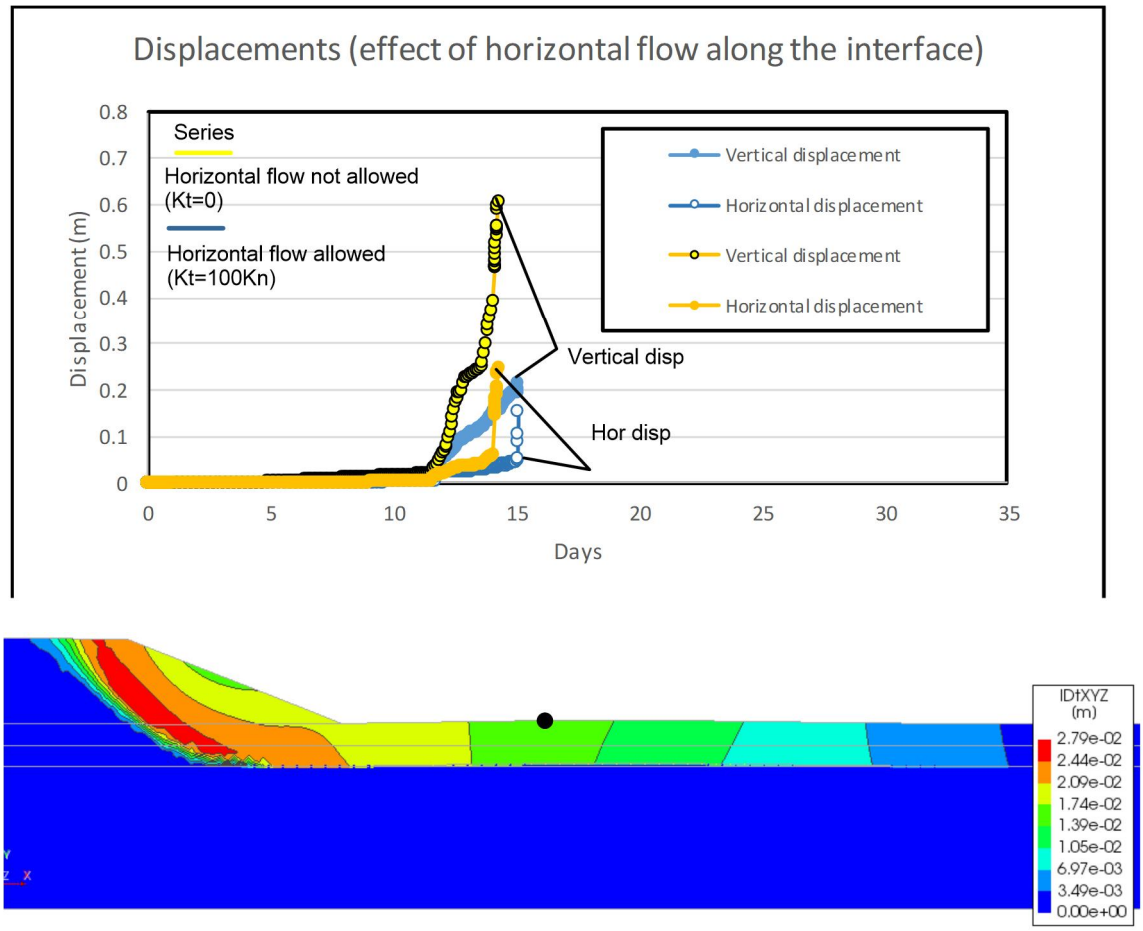

Figure 4.15 Comparison of displacements for cases with and without aquifer

4.5.3 Cracking of clay

Tension softening was used instead of a conventional plastic tension cut off, in order to account sufficiently realistic for the effect of tension cracks in the cover layer during "uplift". To highlight the differences, two cases were computed with and without softening on the cut off. For illustrative purposes only, the tensile strength was limited here to 22kPa in both cases[1]. The cover layer thickness was assumed to be 1m and the strength parameters cohesion and friction angle were c= 22kPa and ϕ=3°, respectively.

Figure 4.16 shows the evolution of the computed vertical displacements of a point located at the top of the cover layer. Both computations produce the same displacement curve, but failure is only predicted in the case with softening cut-off. Using the conventional cut-off results in an unrealistic soil behavior.

The evolution of the effective horizontal stress on top of the cover clay layer for both computations is shown in Figure 4.17. It is observed that, after reaching the tensile strength, the horizontal stresses remain constant (perfect plasticity) in the case of no softening (Figure 4.17a). In the case

[1] *This large value has been applied here only for illustrative purposes. The already reported small value of 3 kPa has been used in the actual simulations, which are reported in chapter 5 and chapter 6.*

where softening is considered, a decay in the stress is observed after reaching the tensile strength (soil cracks), and stresses redistribute (Figure 4.16b).

In case of softening (Figure 4.17b), the cracks propagate deep into the cover layer, until the bending capacity of the cover layer is reached. This behavior is also evident from the distribution of the horizontal effective stresses at the top of the cover layer.

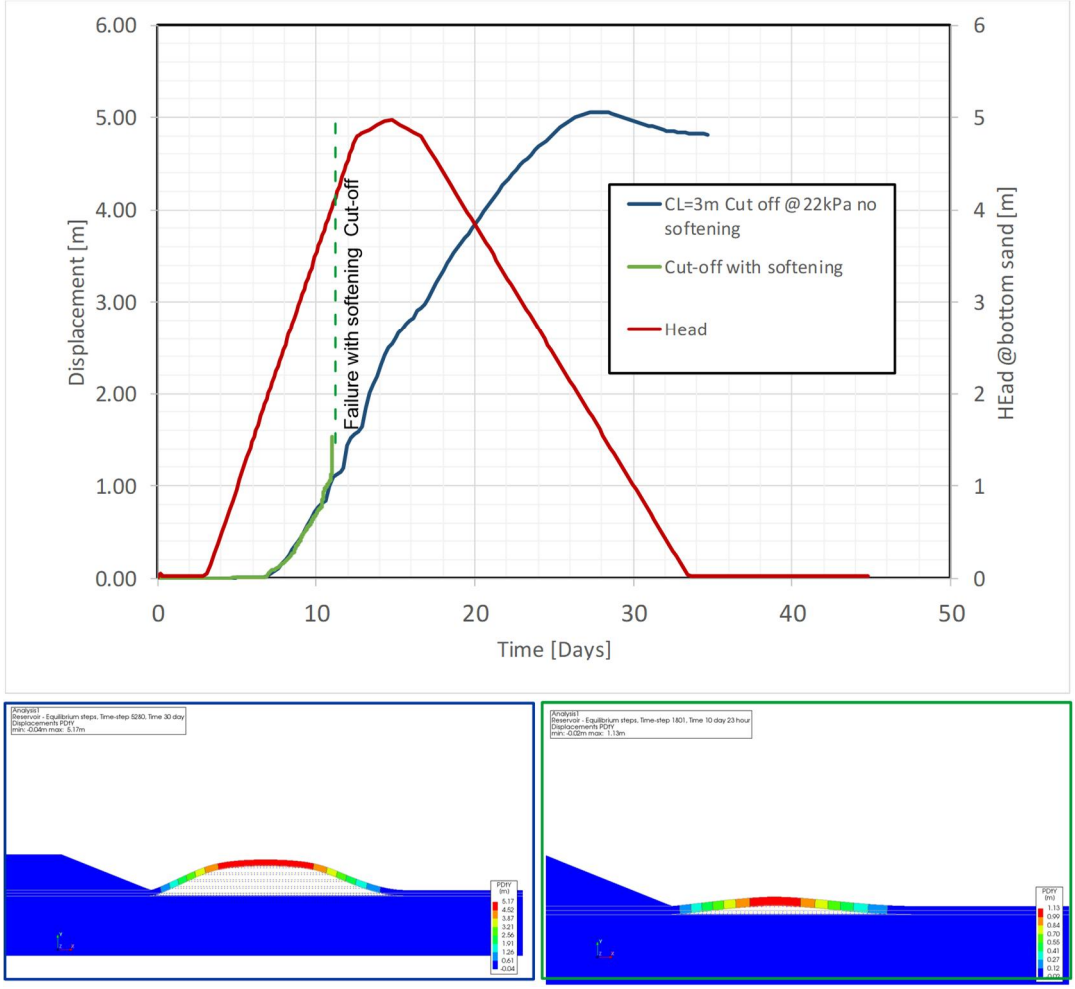

Figure 4.16 Vertical displacement at failure computed without (left-hand side) and with (right-hand side) tension softening

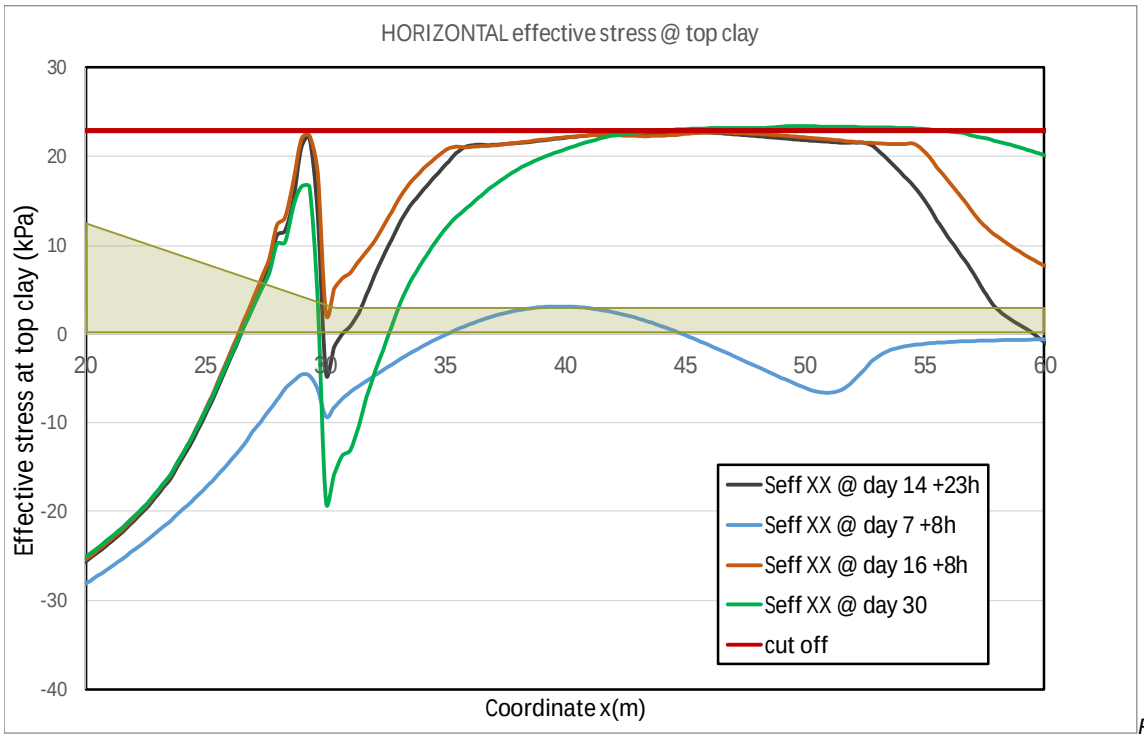

Figure 4.17a Effective horizontal stress at the top portion of the cover clay layer. No tension softening

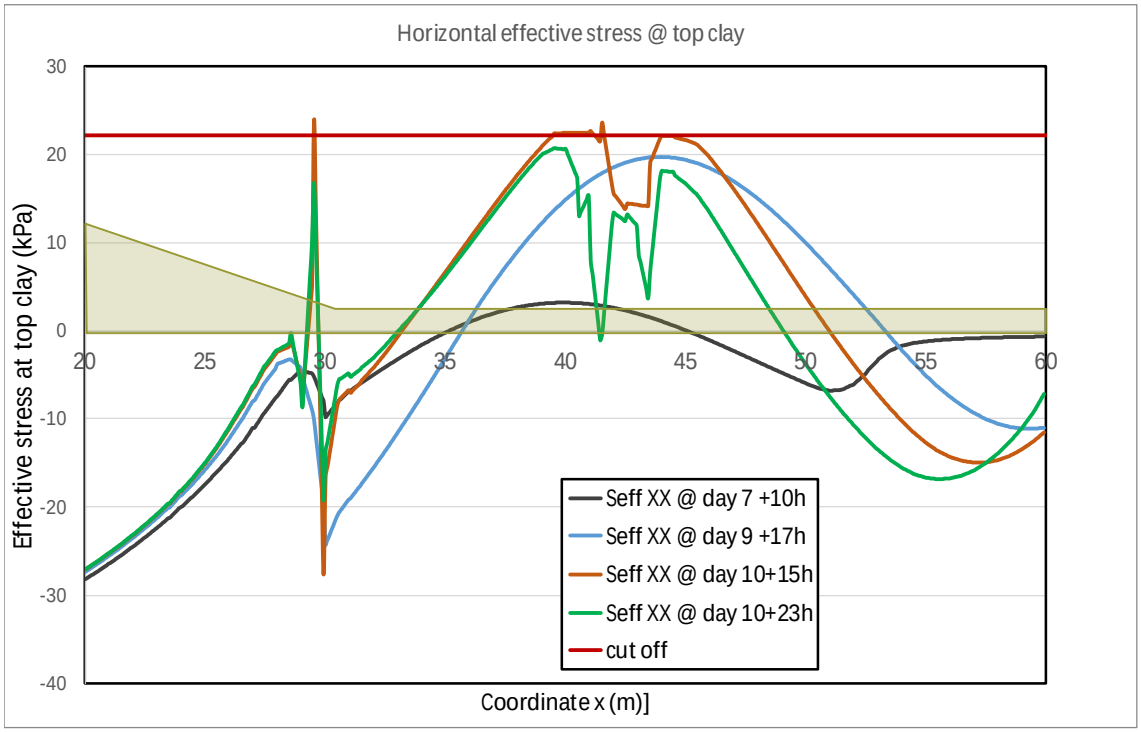

Figure 4.17b Effective horizontal stress at the top portion of the cover clay layer. Tension softening

5 Results for different cover layer thicknesses

5.1 Introduction

In the following sections, the computed failure behaviour will be reported for three basic computations, considering a cover layer thickness of 3m, 2m and 1m. See Table 3.1 for the parameter set that has been applied for each of these cases. For each case, an initial computation was performed with a “high” cohesion value. In this case, uplift can occur without slope instability as a result. Then the cohesion was reduced in steps of 0.5kPa and results were recomputed, until slope instability occurred. The cohesion value resulting in slope instability is defined in the present report as the “critical cohesion”. This critical value is reported in the next paragraphs for the three different cover layer thicknesses. Results show globally that the failure mode proves to be “type 4” for larger cover thicknesses and “type 3” for smaller thicknesses.

5.2 Cover layer thickness of 3 m

5.2.1 Geometry, mesh and boundary conditions

The applied geometry, mesh and boundary conditions for this case are shown in Figure 5.1.

5.2.2 Piezometric head in the sand layer

Figure 5.2 shows the piezometric head in the sand layer as applied at the left-hand side (x=-40m), together with the computed head below the embankment center (x=0). When failure occurs, the computed head at x=0 is 3,1m and the computed head at the toe (x=30m) is 2,27m. Note that, when ignoring stress redistribution, uplift will occur if the water pressure in the interface becomes equal to the weight of the cover layer. The associated “critical piezometric head” ϕ_{critical} is therefore equal to the sum of the “elevation head” at the interface position (-3m) and the cover layer weight divided by the water weight.

$$\phi_{\text{critical}} = -3 + 3 \cdot \frac{17}{9{,}81} = 2{,}2\ \text{m}$$

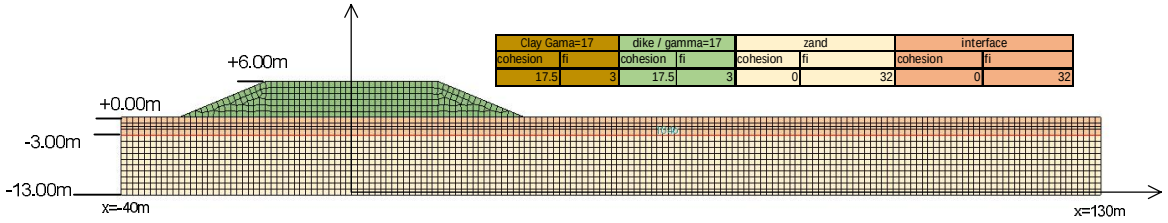

Figure 5.1. Mesh for the Basic Case (3m Cover Layer)

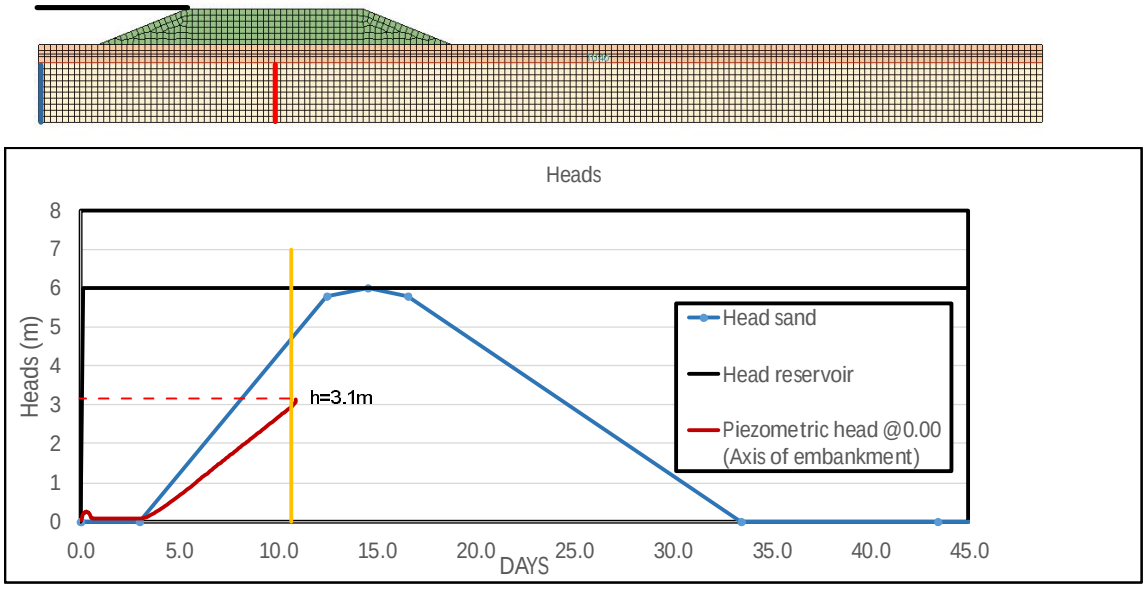

Figure 5.2. Piezometric head variation at the reservoir and in the sand layer. The latter at the left-hand side (x=-40m) and at the embankment axis (x=0)

5.2.3 Material strength parameters

Executing a sequence of analyses while lowering the clay cohesion value in steps of 0,5 kPa resulted in slope instability for a cohesion value of 17,5 kPa. The applied strength parameters for this case are listed in Table 5.1.

Table 5.1 Material Strength parameters (Cover Layer thickness of 3m)

Clay Gama=17		dike / gamma=17		zand		interface	
cohesion	fi	cohesion	fi	cohesion	fi	cohesion	fi
17.5	3	17.5	3	0	32	0	32

5.2.4 Displacements

The temporal displacement evolution of a point located at the toe of the embankment is shown in Figure 5.3. Figure 5.4 shows a vector plot and a contour plot of the total displacements at failure. Figure 5.5 shows a vector plot of the incremental displacements at failure. Uplift and bending do not occur.The incremental displacement pattern seems to suggest that the failure mode is type 4. This is supported by the observation in § 5.2.5 that the state of the cover layer is fully elastic.

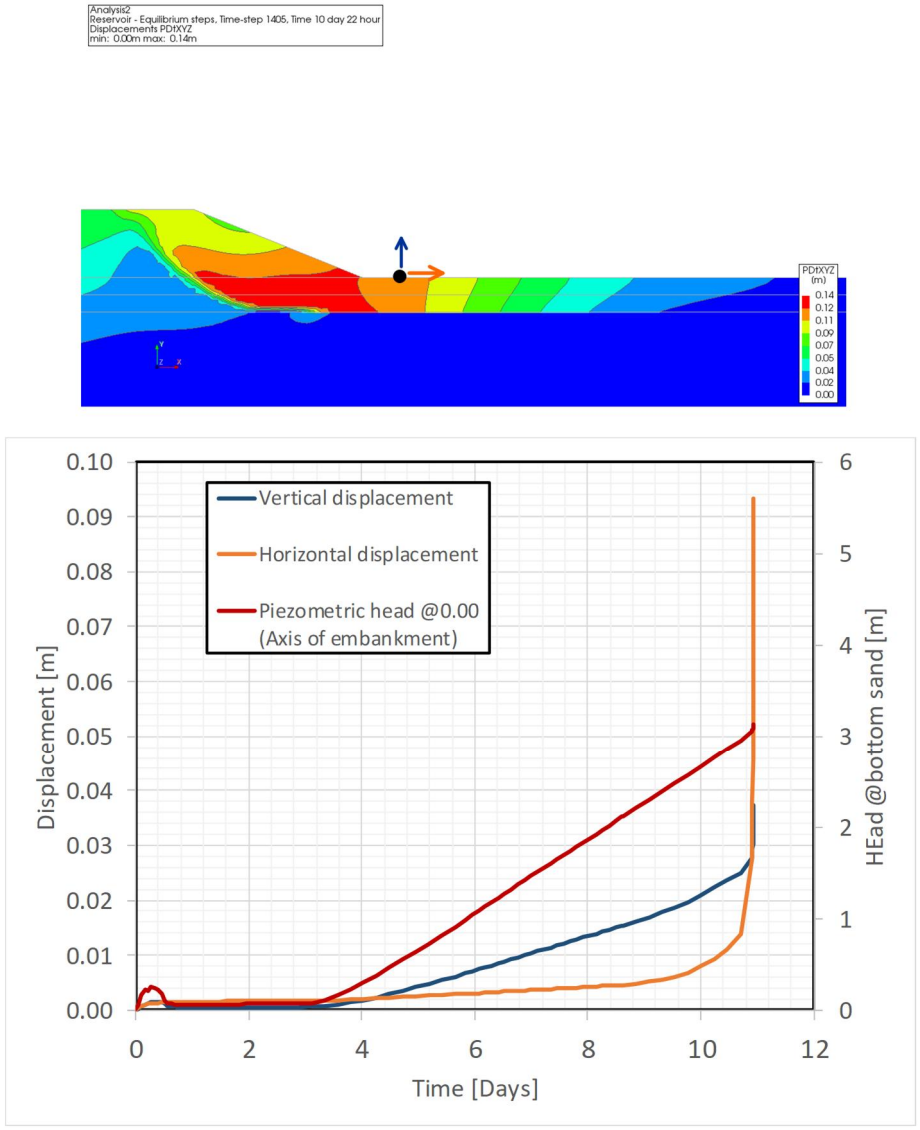

Figure 5.3. The displacements of a point located on top of the cover layer near the toe of the embankment and the piezometric head at the axis of the embankment, as a function of time

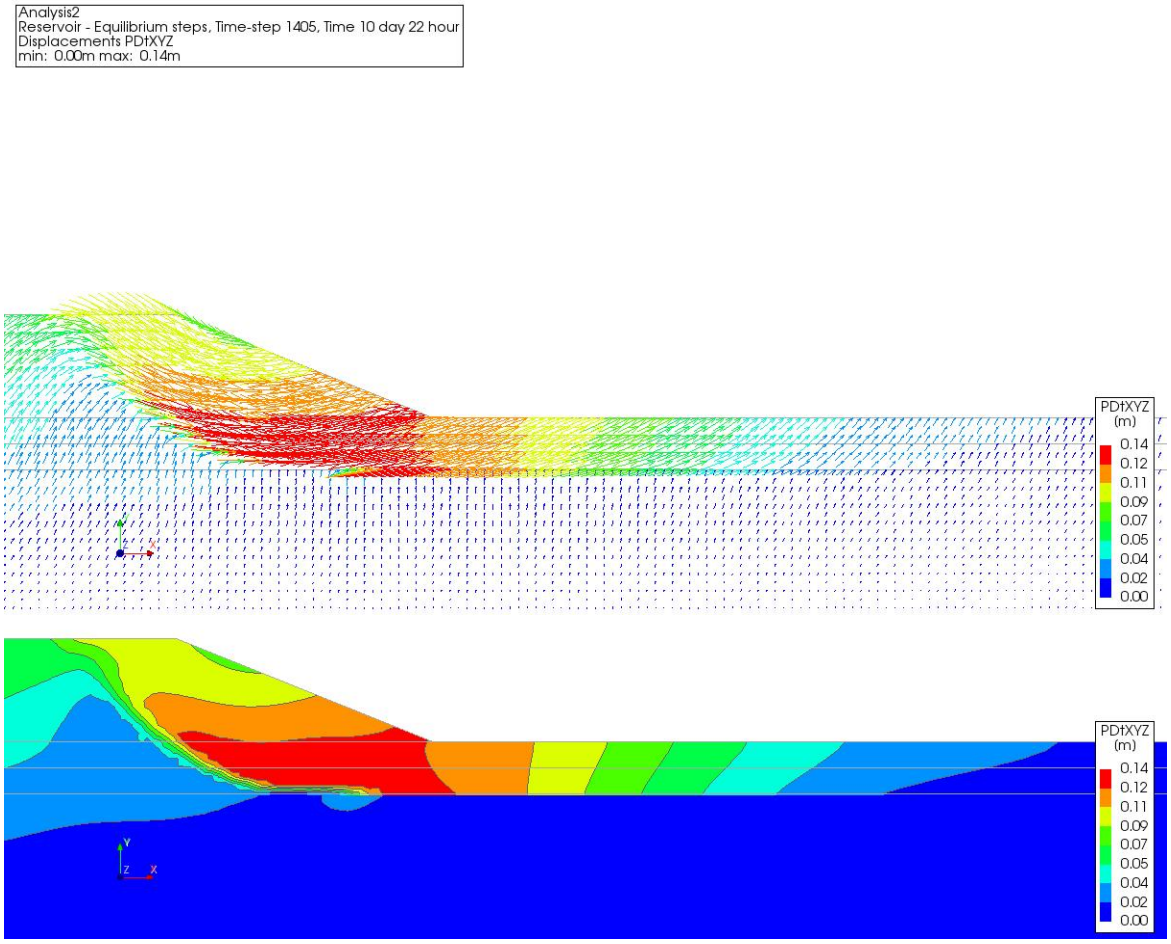

Figure 5.4. Total displacements at failure (vector plot and contour plot)

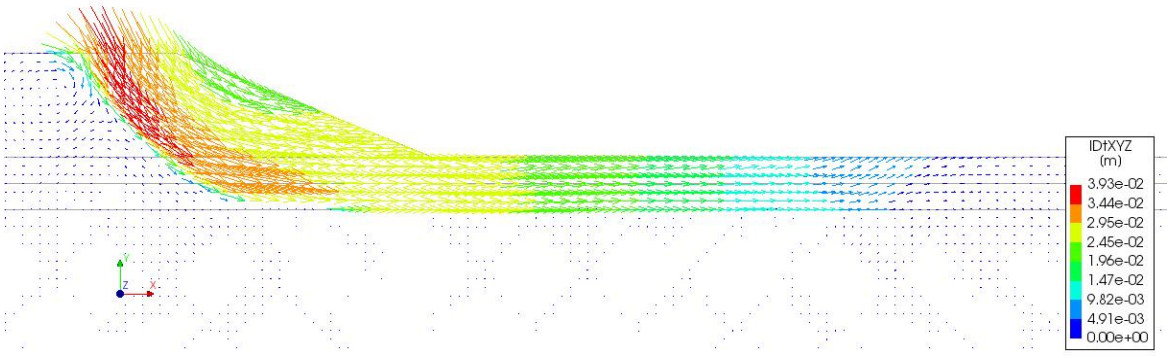

Figure 5.5. Incremental displacements at failure (vector plot)

5.2.5 Pressure field

Figure 5.6 shows the pore pressure and the piezometric head distribution along horizontal lines located at the top, middle and bottom of the sand layer. A linear distribution is observed, corresponding to the fact that the interface is not opening and therefore does not influence the pore pressure distribution.

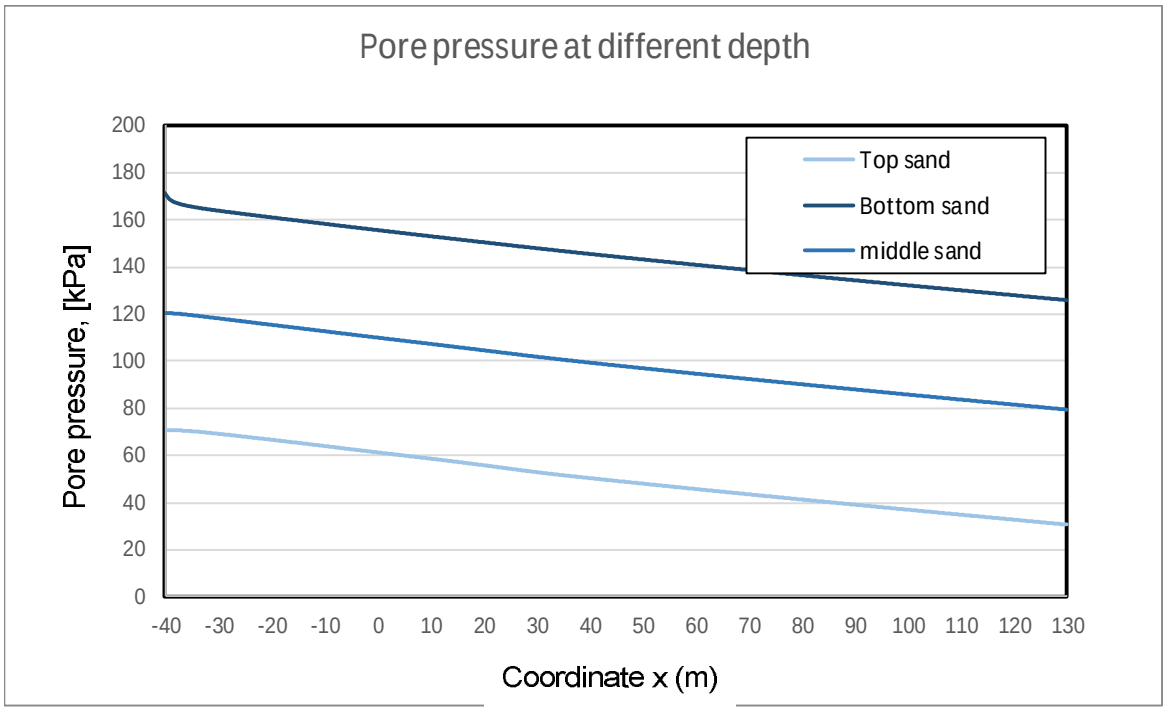

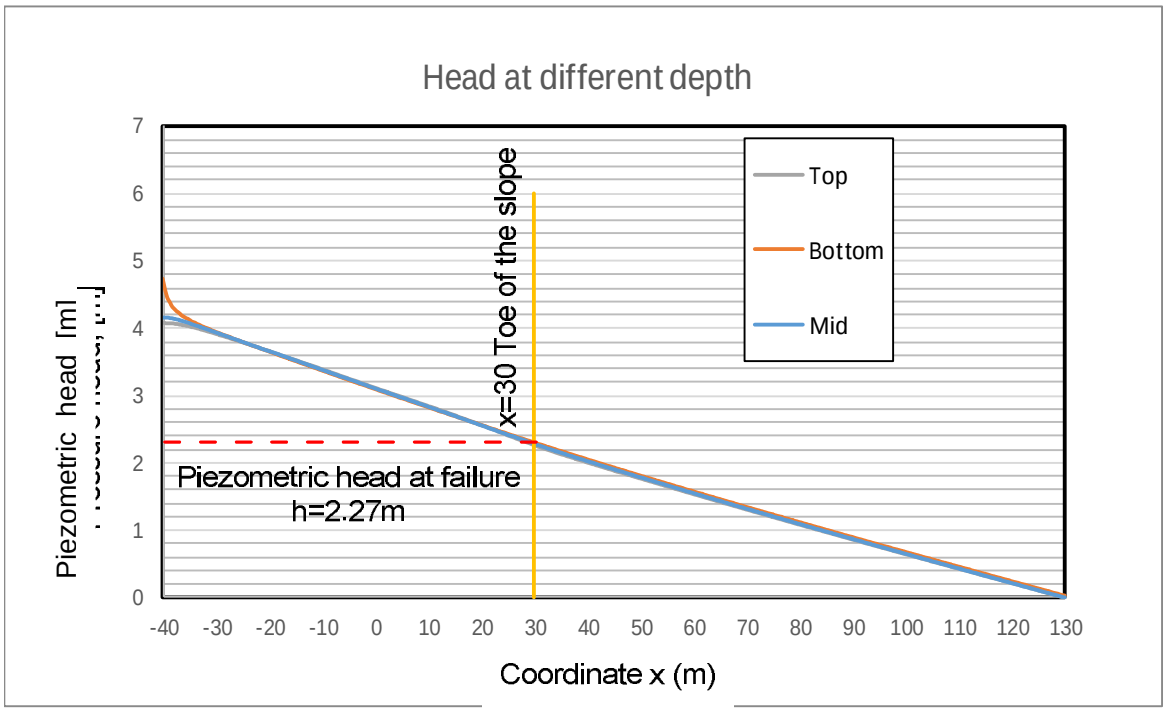

Figure 5.6. Pore pressure and piezometric head at top, middle and bottom of the sand layer

5.2.6 Stresses and strains

The “type 4” failure mode classification is supported by Figure 5.7. This figure shows the value of the mobilized shear strength capacity SHRCAP, which equals the ratio between shear stress and (Mohr-Coulomb) shear strength. The discontinuity at the interface between the embankment clay and the clay layer below is caused by the construction sequence modeling. When SHRCAP=1, the

shear-strength is reached. The plot shows that the shear strength capacity in the cover layer is not reached at any position. The cover layer is therefore in a fully elastic state (assuming that cracking has not occurred). In the embankment and at the interface between the cover layer and the sand develops a shear plane, while the cover layer itself compresses like a spring. Figure 5.9 shows the principal stresses at failure, indicating also that the cover layer is compressed and that no that no major bending/uplift is produced.

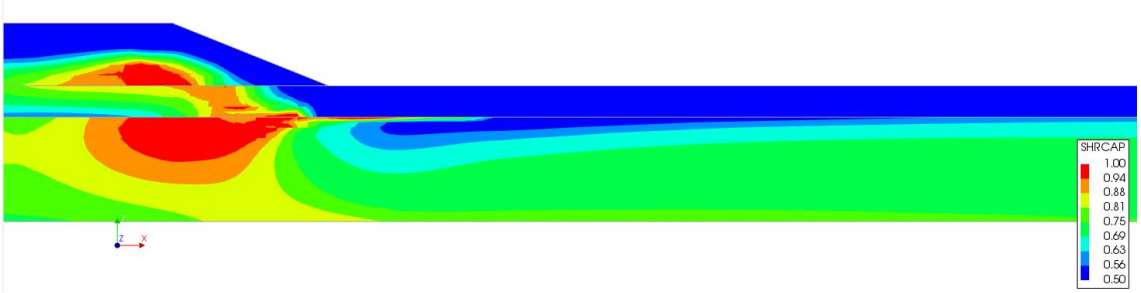

Figure 5.7: Mobilized shear strength ratio at failure

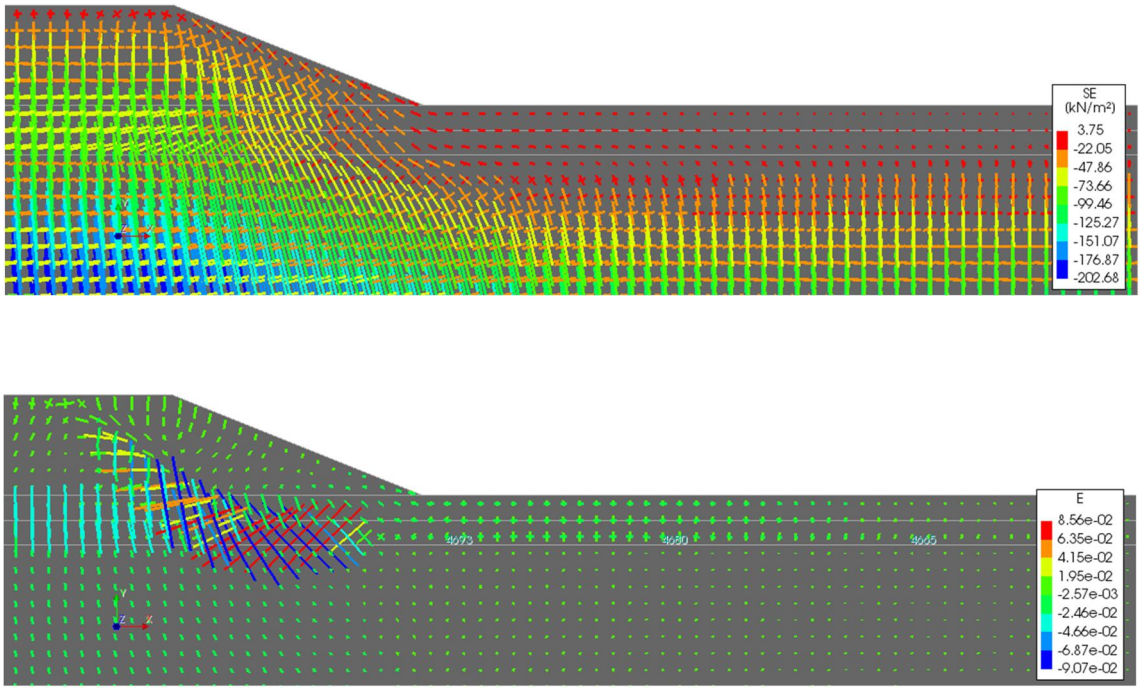

Figure 5.8. Principal stresses (top) and principal strains (bottom)

Figure 5.9 shows the effective normal stress and shear stress along the interface at the time of failure. From this figure we can see that the slip plane reaches the interface between clay and sand at the location of 3 m left from the embankment toe. At this location, the shear stress is circa 17 kPa, which corresponds to the critical cohesion value of 17,5 kPa.

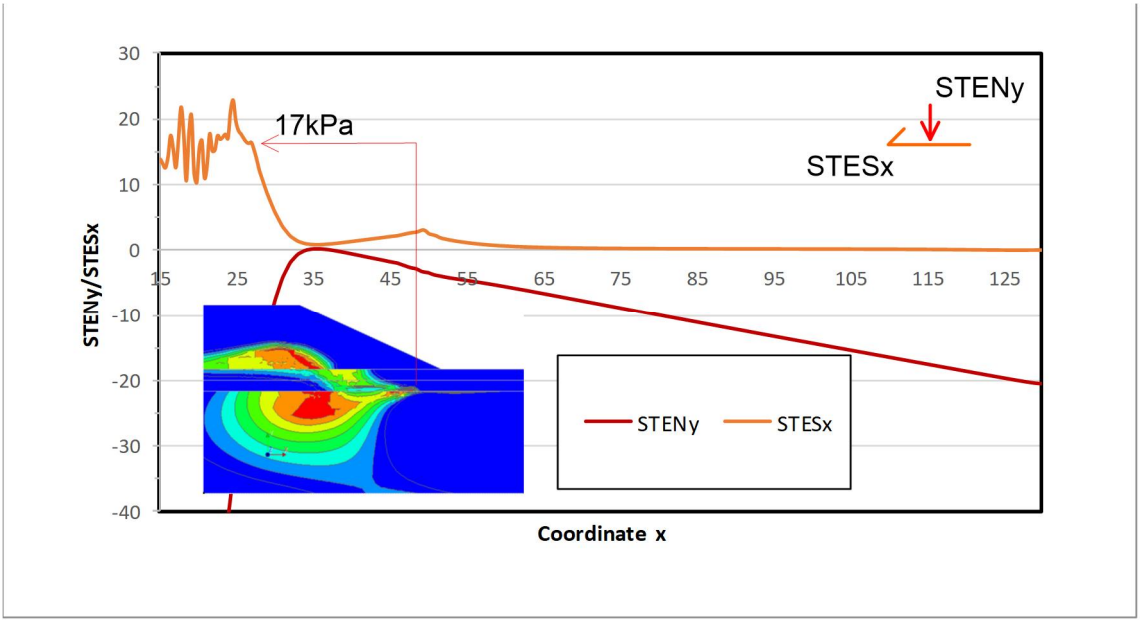

Figure 5.9 Normal stresses (STENy) and shear stresses (STESx) along the interface

Figure 5.10 shows the evolution of effective vertical stresses for three points located at the top part of the sand layer, in a zone close to the toe of the embankment. No uplift occurs at failure. The small perturbations at the beginning are caused by the temporary excess pore pressures resulting from embankment construction and reservoir impounding (Phases 1 to 3 in the analysis).

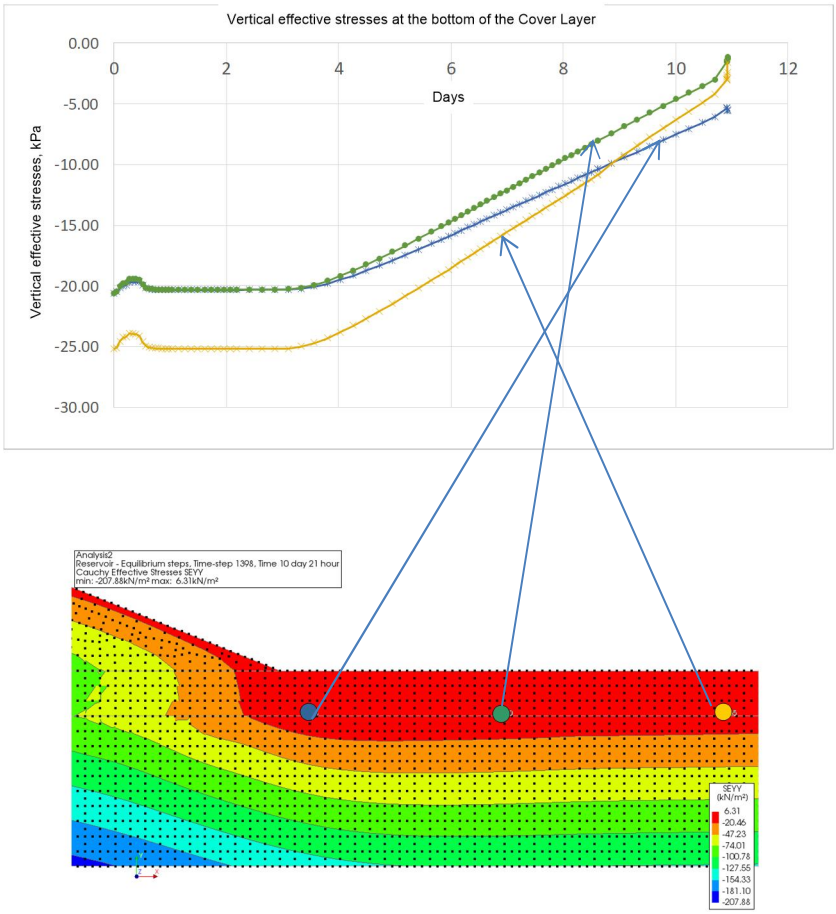

Figure 5.10.Development of the vertical effective stress in three points at the top of the sand layer from the start of the analysis until failure

5.2.7 Global forces

The load transfer mechanism occurring at failure can be interpreted from the graphs of the axial force and bending moment acting in the cover layer. Forces and moments are computed by integration of the horizontal effective stresses acting on the clay layer. Figure 5.11 shows the evolution of the normal force N and bending moment M in the cover layer at the toe of the embankment. The eccentricity value at that location is computed as the ratio between the moment and force. When shear failure occurs, this leads to a sudden increase of the compressive force N in the cover layer.

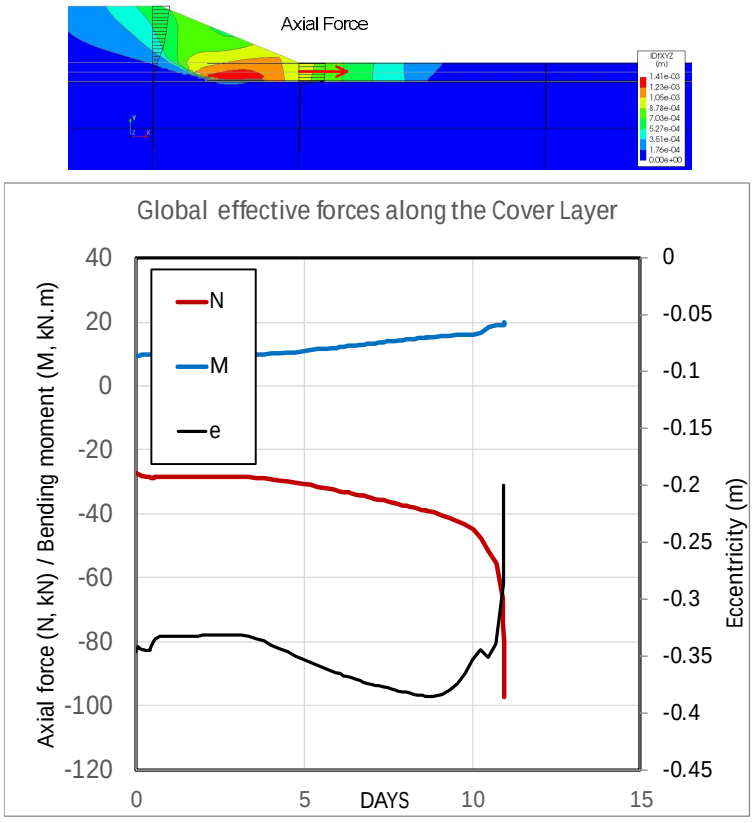

Figure 5.11. Temporal evolution of the effective axial force (negative in compression) and bending moment in the clay layer at the toe of embankment

5.3 Cover layer thickness of 2 m

5.3.1 Geometry, mesh and boundary conditions

The applied geometry, mesh and boundary conditions for this case are shown in Figure 5.12.

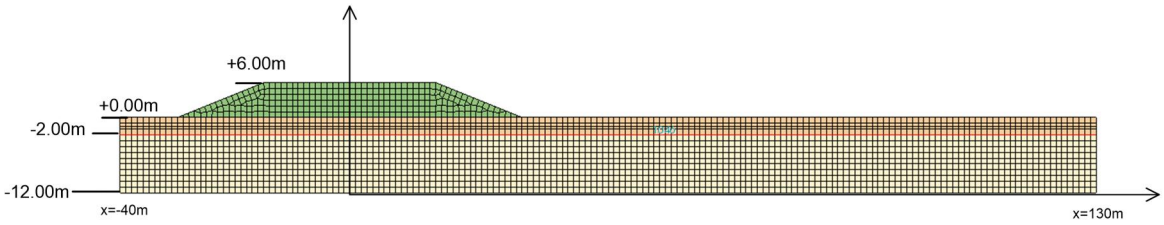

Figure 5.12. Mesh for the Basic Case with a cover layer thickness of 2 m

5.3.2 Piezometric head in the sand layer

Figure 5.13 shows the piezometric head in the sand layer as applied at the left-hand side (x=-40 m), together with the computed head below the embankment center (x=0). When failure occurs, the computed head at x=0 is 1,95 m and the computed head at the toe (x=30 m) is 1,43 m. The “critical piezometric head” equals1,46 m.

$$\phi_{\text{critical}} = -2 + 2 \cdot \frac{17}{9{,}81} = 1{,}46 \text{ m}$$

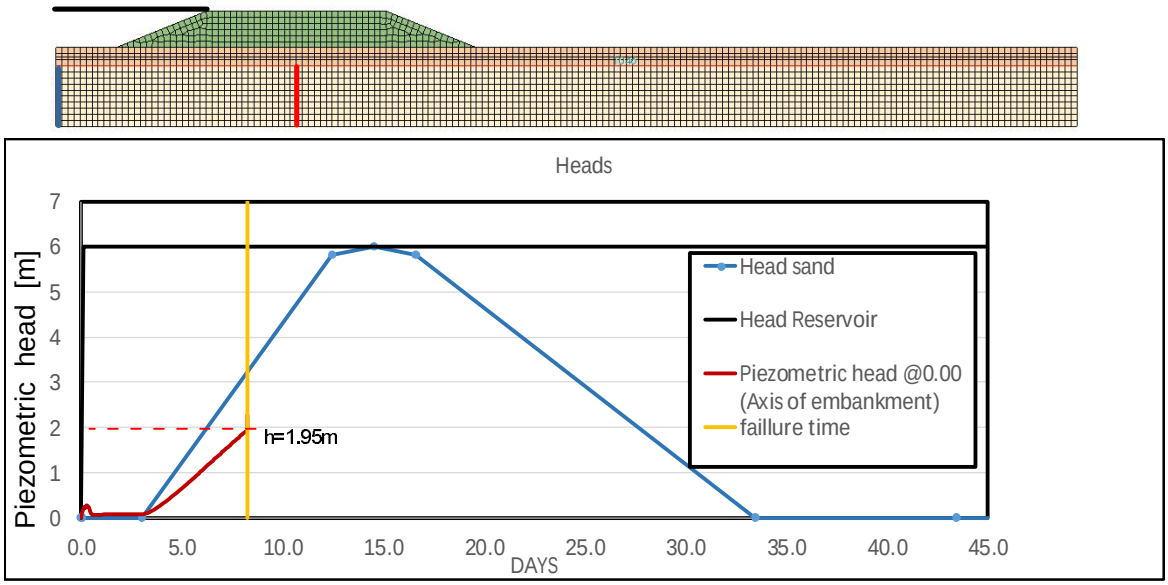

Figure 5.13. Piezometric head variation at the reservoir and in the sand layer. The latter at the left-hand side (x=-40m) and at the embankment axis (x=0).

5.3.3 Material strength parameters

Executing a sequence of analyses while lowering the clay cohesion value in steps of 0,5 kPa resulted in slope instability for a cohesion value of 16,5 kPa. The applied strength parameters for this case are listed in Table 5.2.

Table 5.2 Material Strength parameters (Cover Layer 2 m)

Clay Gama=17		dike / gamma=17		zand		interface	
cohesion	fi	cohesion	fi	cohesion	fi	cohesion	fi
16.5	3	16.5	3	1	32	0	32

5.3.4 Displacements

The temporal displacement evolution of a point located at the toe of the embankment is shown in Figure 5.14. Failure is found at 8 days, when the horizontal displacements at the top of the cover layer start to increase rapidly. Figure 5.15 shows a vector plot and contour plot of the incremental displacements at failure. The displacement pattern and the elastic state of the cover layer (see § 5.3.5) support the conclusion that the failure mode is initially again purely type 4. Figure 5.16 shows the relative displacements along the interface at failure. Shearing along the interface is observed, but no gapping.

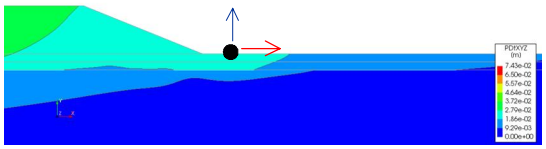

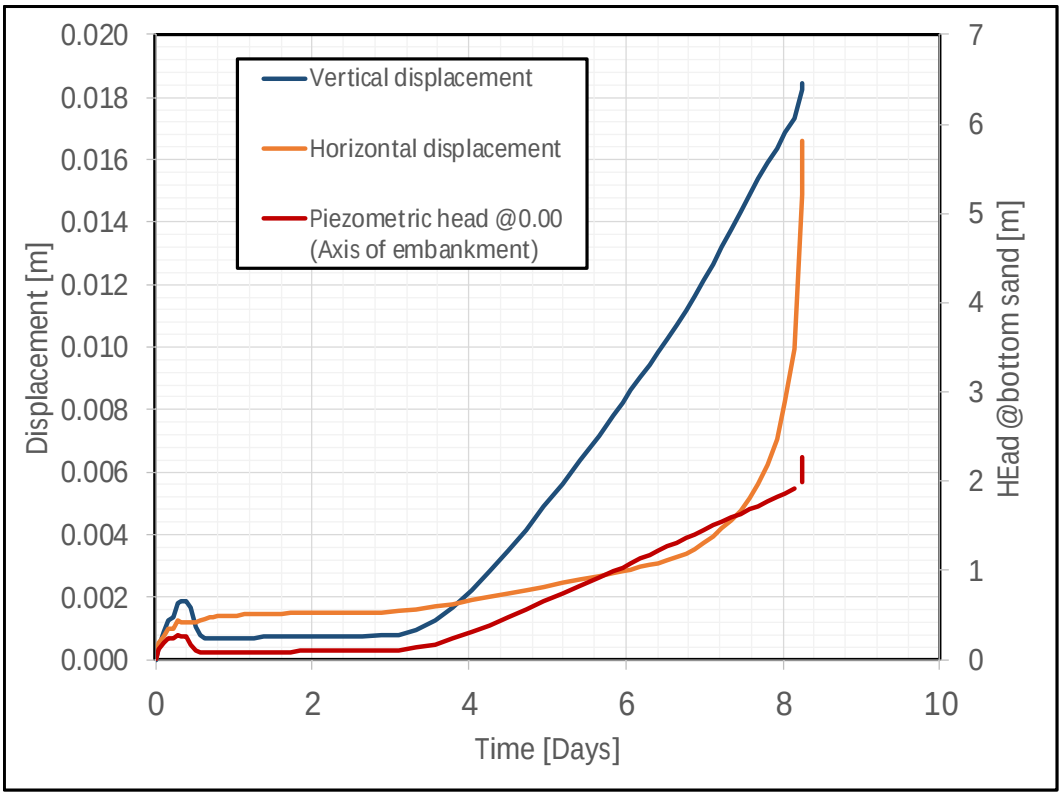

Figure 5.14. Displacements in a point located on top of the cover layer near the toe of the embankment

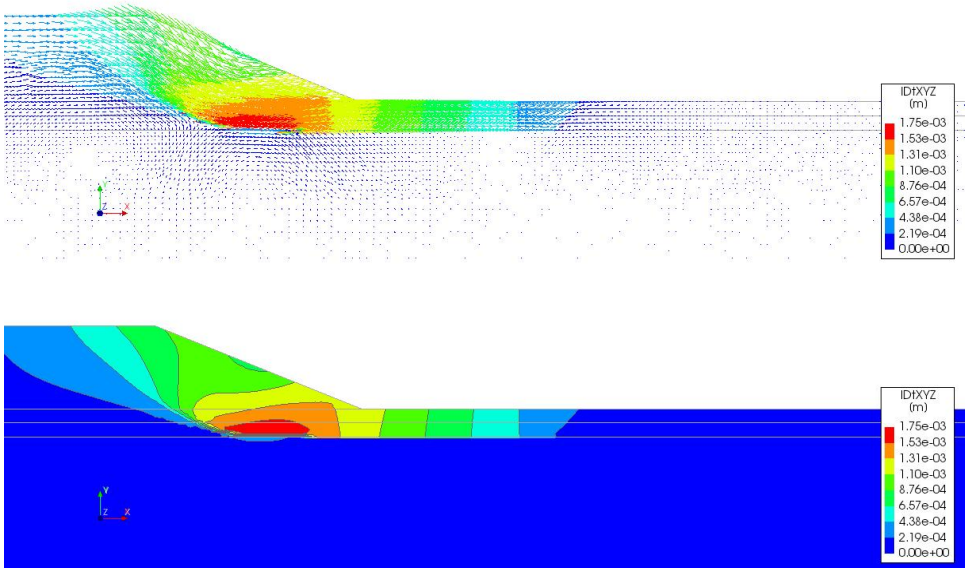

Figure 5.15. Incremental displacements at failure (vector plot and contour plot) (8 days, 5 hours)

Interface displacements

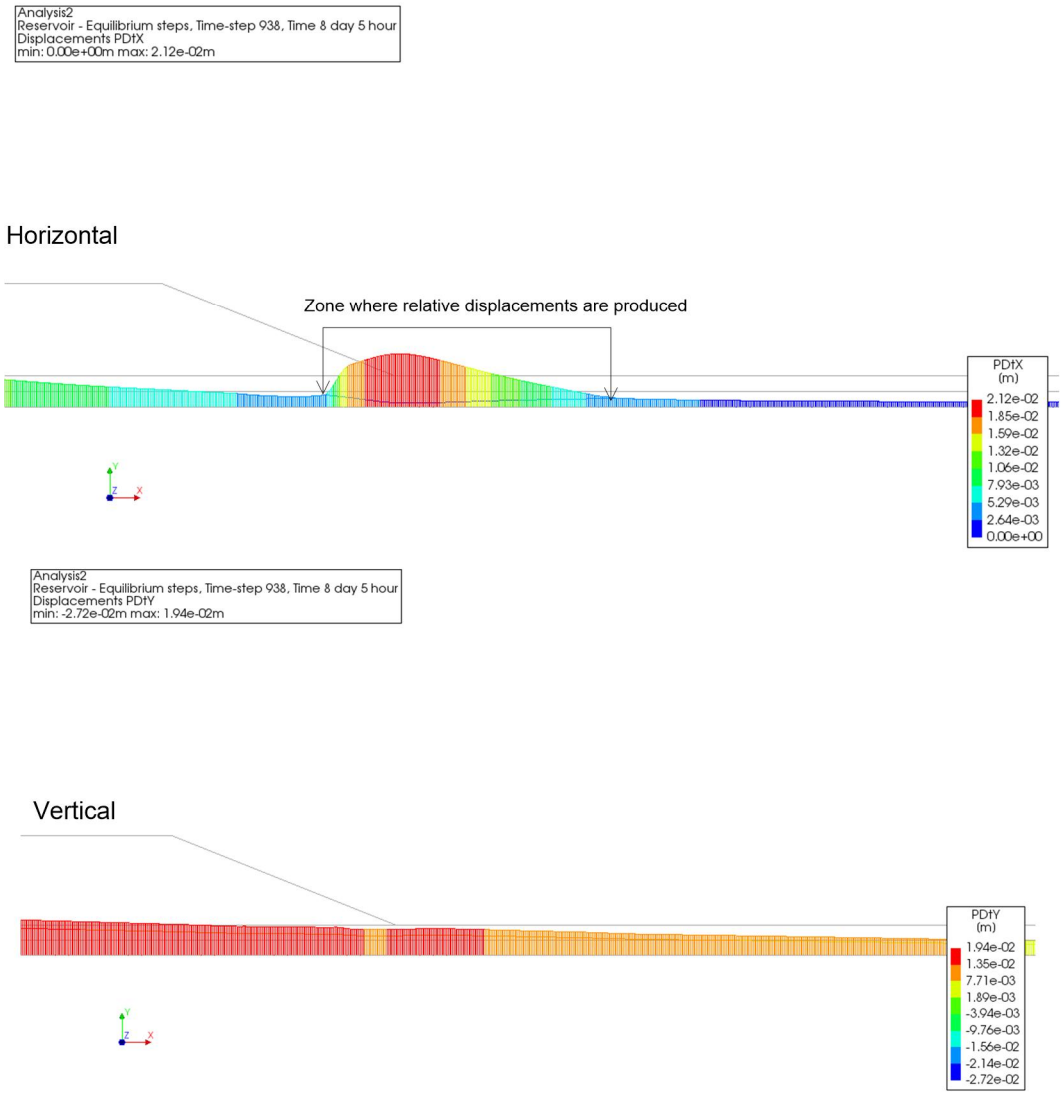

Figure 5.16. Relative displacements along the interface at failure. Top: horizontal slip displacement. Bottom: vertical displacement (not showing a gap)

5.3.5 Pressure field

Figure 5.17 shows the pore pressure and the piezometric head distribution along horizontal lines located at the top, middle and bottom of the sand layer. A linear distribution is again observed, corresponding to the fact that relative gap displacements are smaller than the threshold value b0=3mm.

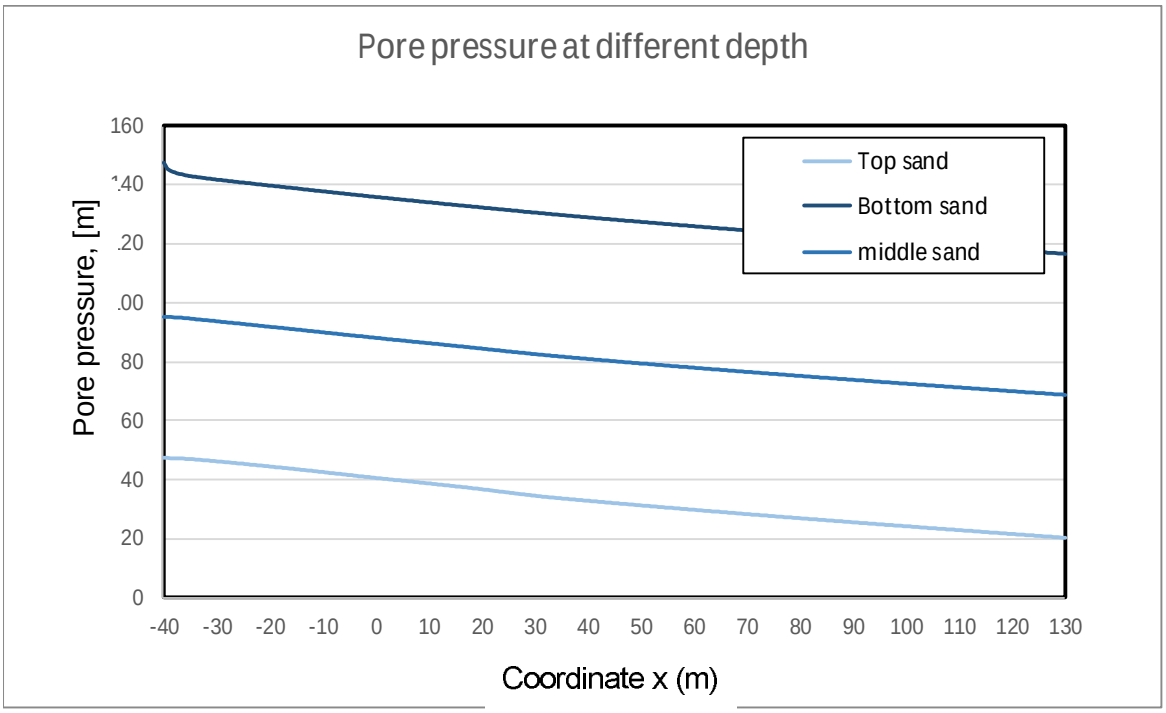

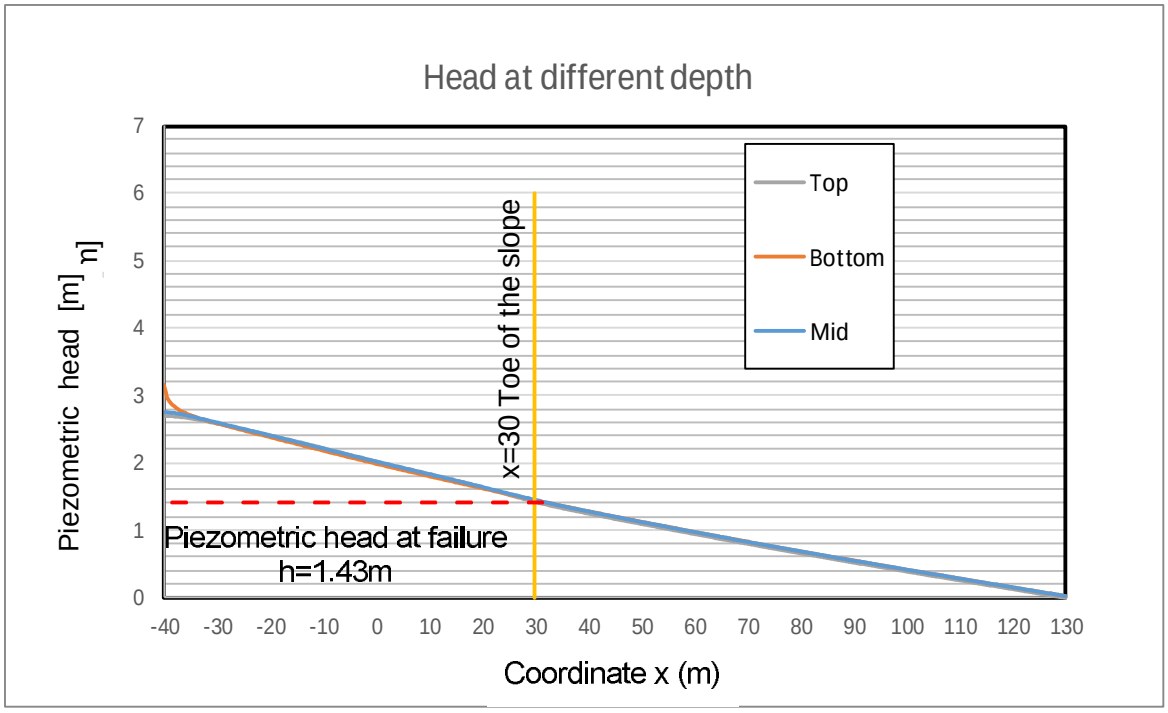

Figure 5.17. Pore pressure and piezometric head at top, middle and bottom of the sand layer

5.3.6 Stresses and strains

The “type 4” failure mode assumption is again supported by the plot of the mobilized shear strength ratio in Figure 5.18. The shear strength capacity in the cover layer is not reached. The figure gives also a graph of the development of normal stress and shear stress along the interface at failure. The normal stress becomes equal to zero along a small zone, starting closely behind the inner toe.

The shear stress in the interface at the start of sliding zone (around 3 m at the left-hand side of the toe) is between 15 to 16kPa, which corresponds to the critical cohesion value of 16,5 kPa. Figure 5.19 shows that the tensile strength in the cover layer is not exceeded.

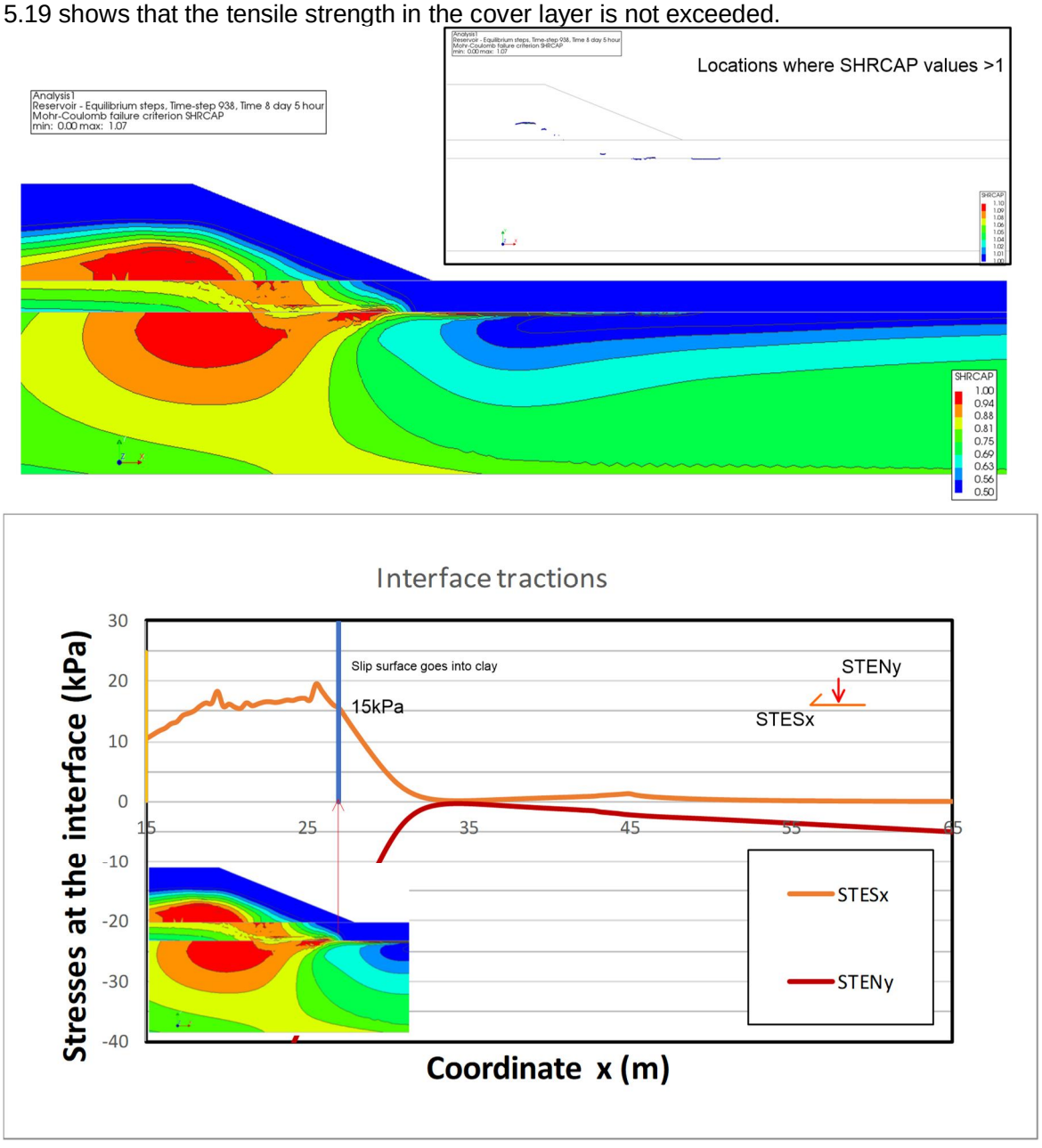

Figure 5.18.Top: Mobilized shear stress ratio. Bottom: distribution of the normal stress (STENy) and shear stress (STENx) along the interface

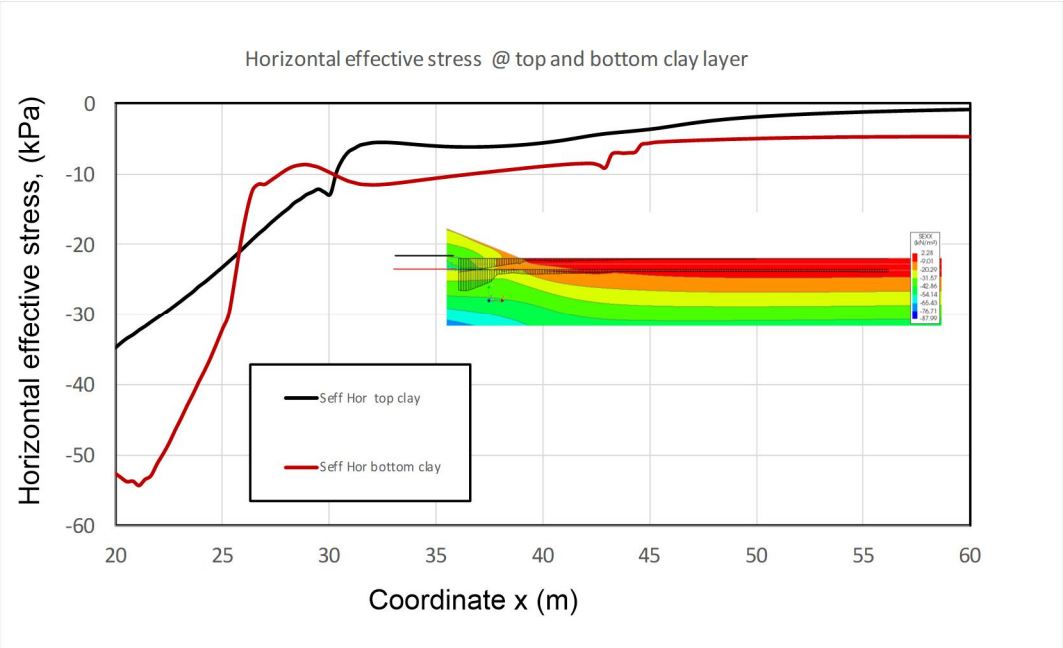

Figure 5.19.Horizontal effective stresses along the top and bottom of the cover layer (bottom right) at failure (8 days and 5 hours)

Figure 5.20 shows the temporal evolution of the effective vertical stress at the top of the sand layer, for three points located closely to the inner toe. This graph illustrates also that the normal stress in the interface becomes equal to zero along a small zone, starting closely behind the inner toe.

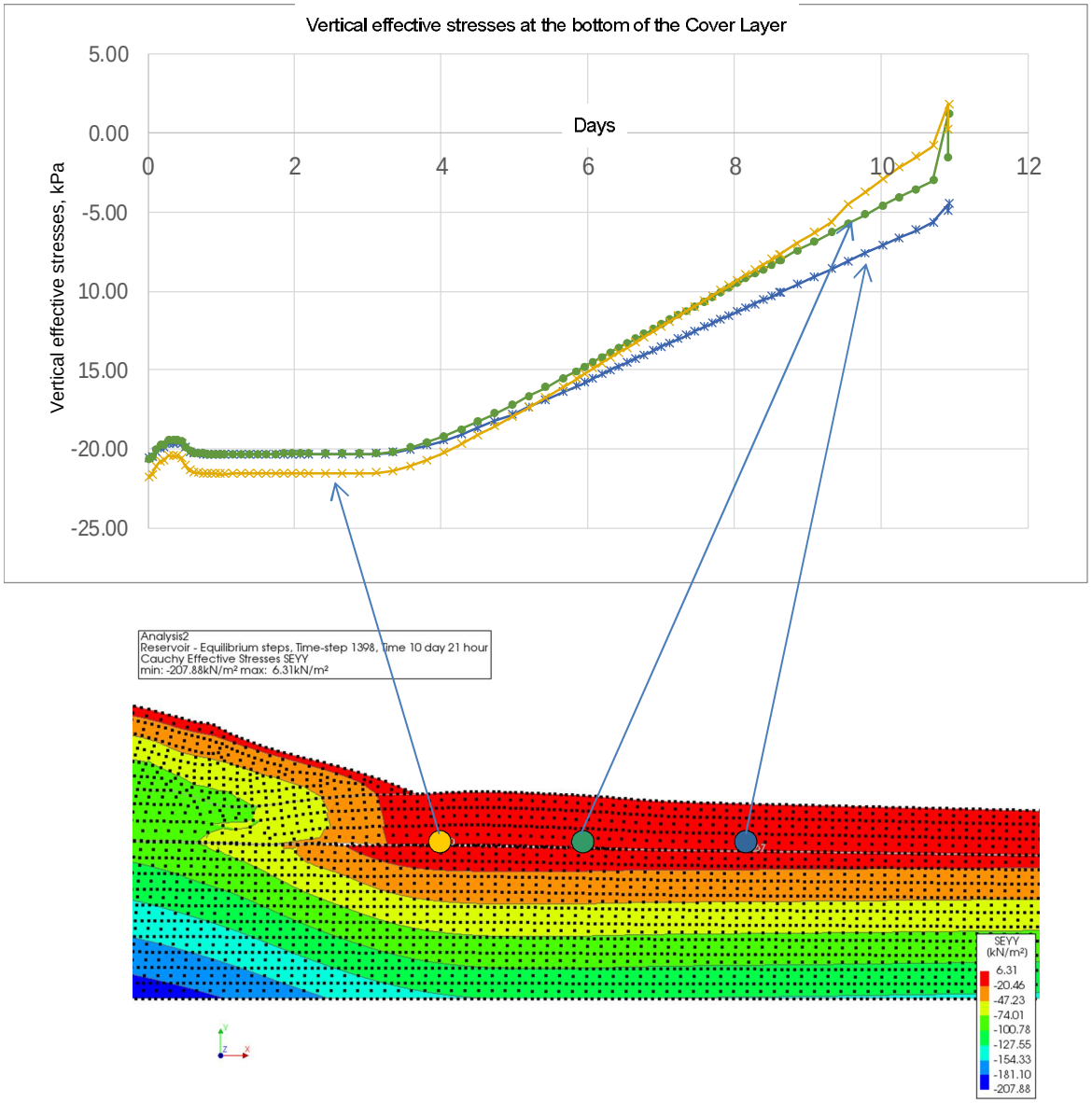

Figure 5.20.Development of the vertical effective stress in three points at the top of the sand layer from the start of the analysis until failure

5.3.7 Global forces

Figure 5.21 shows the evolution of the axial force N, bending moment M and eccentricity value e. The analysis becomes instable at 8 days and 5 hours, when the axial force is becoming more and more compressive. The eccentricity and bending moment do not change strongly.

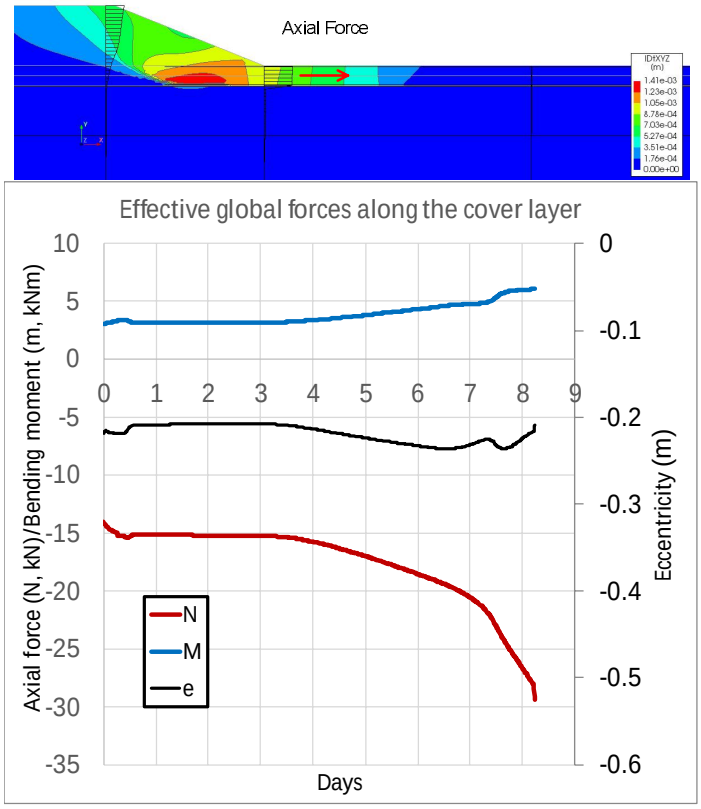

Figure 5.21.Evolution of the effective axial force (negative in compression) and bending moment in the clay layer at the toe of embankment

5.4 Cover layer thickness of 1m

5.4.1 Geometry, mesh and boundary conditions

The applied geometry, mesh and boundary conditions for this case are shown in Figure 5.22.

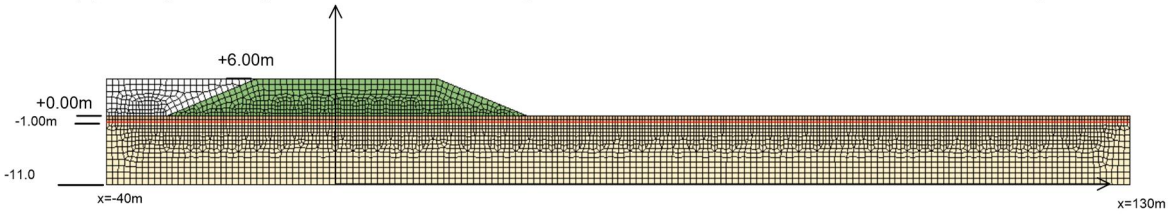

Figure 5.22. Mesh for the Basic Case with a cover layer thickness of 1 m

5.4.2 Piezometric head in the sand layer

Figure 5.23 shows the piezometric head in the sand layer as applied at the left-hand side (x=-40m), together with the computed head below the embankment center (x=0). When failure occurs, the computed head at x=0 is 1,37m and the computed head at the toe (x=30m) is 0,78m. The “critical piezometric head” equals 0,73m.

$$\phi_{\text{critical}} = -1 + 2 \cdot \frac{17}{9{,}81} = 0{,}73 \text{ m}$$

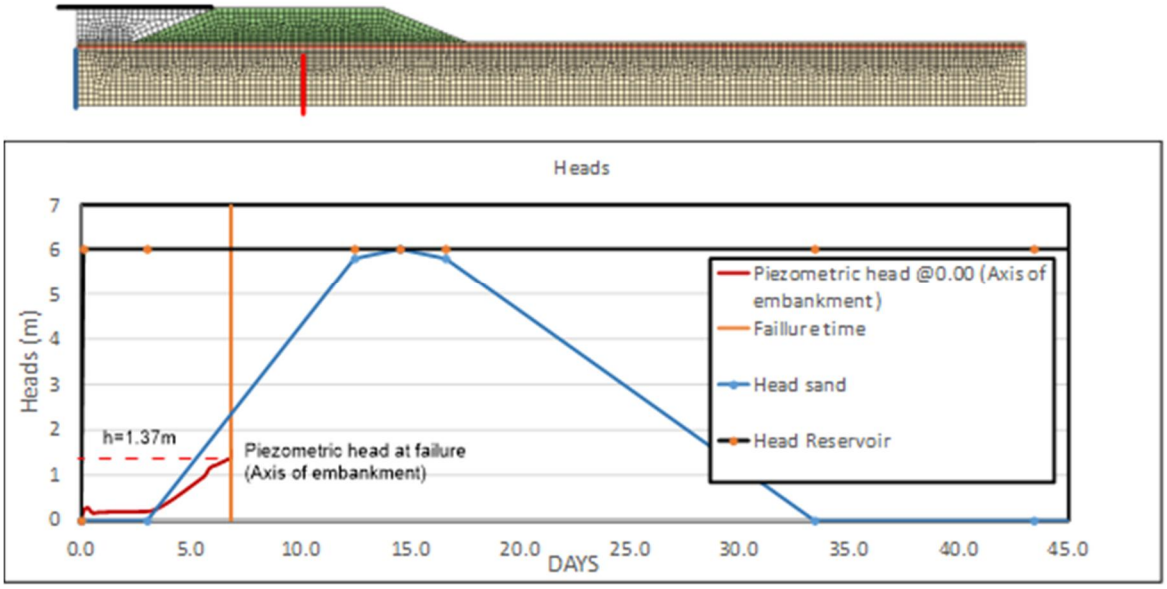

Figure 5.23.Piezometric head variation at the reservoir and in the sand layer. The latter at the left-hand side (x=-40m) and at the embankment axis (x=0)

5.4.3 Material strength parameters

Executing a sequence of analyses while lowering the clay cohesion value in steps of 0,5 kPa resulted in slope instability for a cohesion value of 14 kPa. The applied strength parameters for this case are listed in Table 5.3.

Table 5.3 Material Strength parameters (Cover Layer 1 m)

Clay Gama=17		dike / gamma=17		zand		interface	
cohesion	fi	cohesion	fi	cohesion	fi	cohesion	fi
14	3	14	3	1	32	0	32

5.4.4 Displacements

Figure 5.24 shows the total gap size along the interface close to buckling failure. Uplift occurs along a zone of approximately 22m, starting at the inner toe. The temporal evolution of displacements of a point located at the toe of the embankment is shown in Figure 5.25. A “type 3” buckling failure mode occurs at 6 days and 19 hours, indicated by a strong increase in vertical displacement at that point. Figure 5.26 shows a vector plot of the incremental displacements at failure.

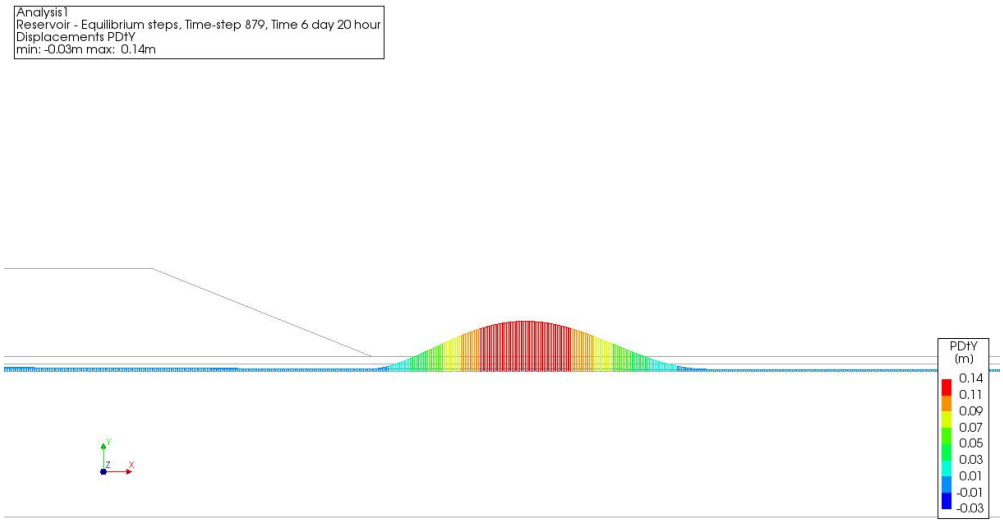

Figure 5.24. Gap opening along the interface at the start of failure (maximum value: 0,14 m)

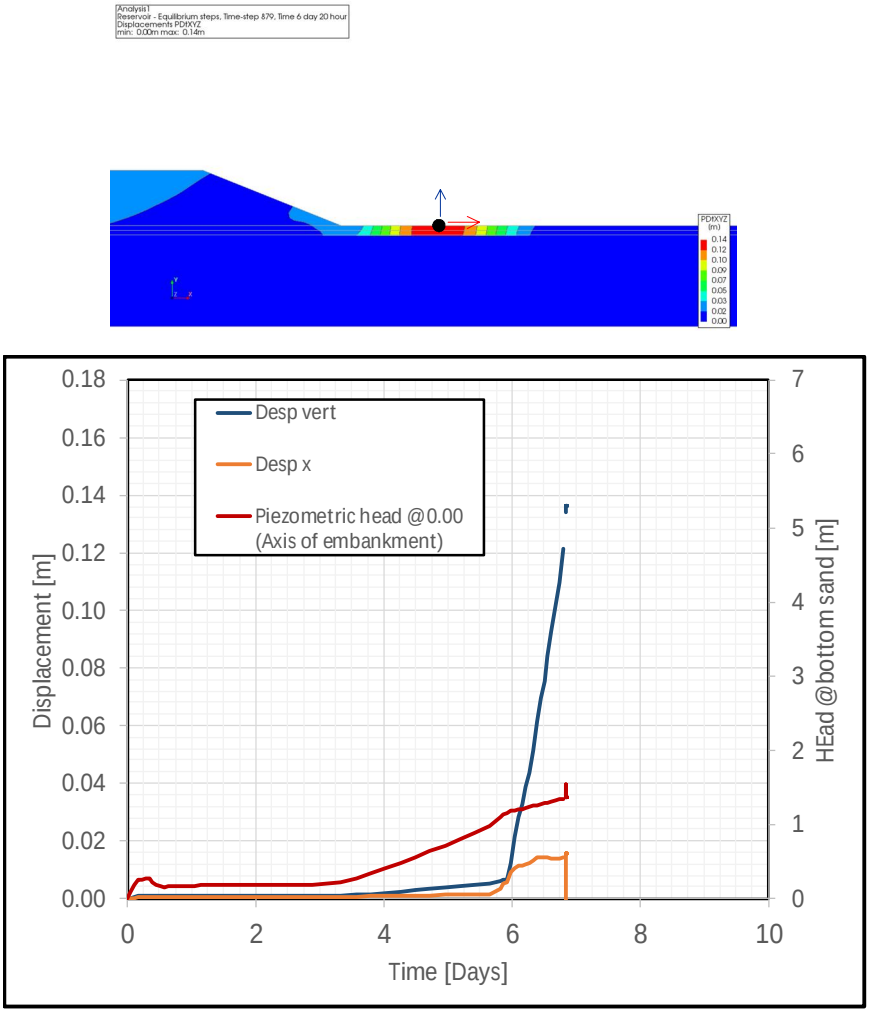

Figure 5.25.The displacements of a point located on top of the cover layer near the toe of the embankment and the piezometric head at the axis of the embankment, as a function of time

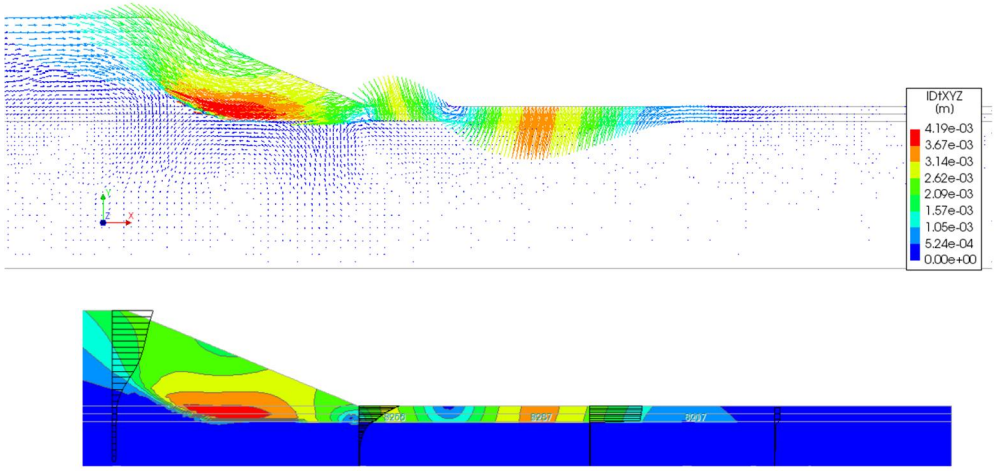

Figure 5.26.Incremental displacements at failure (vector plot and contour plot). Downward incremental displacement of the cover layer close to the toe changes to upward incremental displacement further from the toe, caused by the start of buckling failure, in interaction with the occurance of cracking at the toe

5.4.5 Pressure field and flow field

Figure 5.27 shows the pore pressure and the piezometric head distribution along horizontal lines located at the top, middle and bottom of the sand layer. The influence of the horizontal hydraulic shortcut along the open part of the interface is visible in the top part of the sand. Figure 5.28 shows a detailed view, indicating that the length of zone with the horizontal hydraulic shortcut is a bit smaller than the length of the zone with zero effective stress, because of the threshold value of 3 mm for the gap displacement.

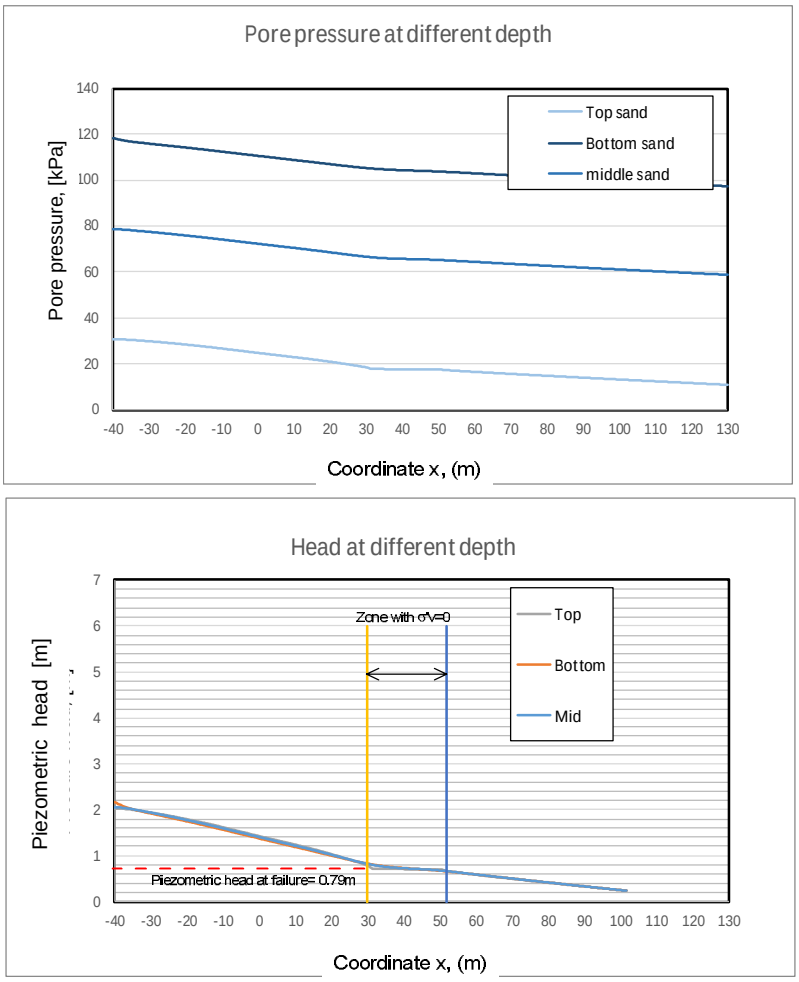

Figure 5.27. Pore pressure and piezometric head at top, middle and bottom of the sand layer

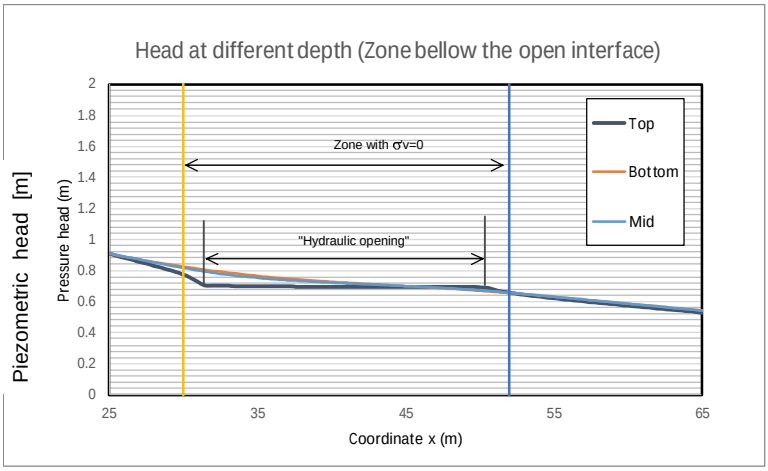

Figure 5.28.Detailed view of the pressure head along the uplifted zone. The zones with vertical effective stress=0 and with "horizontal hydraulic shortcut" are indicated separately

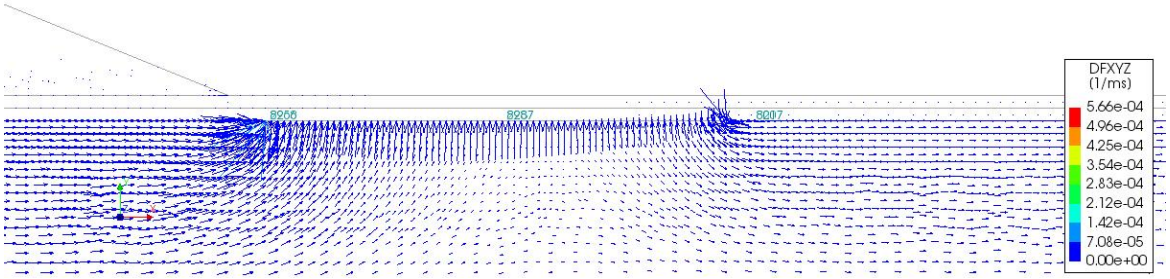

Figure 5.29.Flow pattern at failure. It can be seen that the buckling deformation of the cover layer enforces vertical inflow of water with a magnitude corresponding to the deformation increase, while the horizontal hydraulic shortcut enforces inflow at the left-hand side of the gap and outflow at the right-hand side

5.4.6 Stresses and strains

The plot of the mobilized shear strength ratio in Figure 5.30 shows that the shear strength capacity in the cover layer is not reached. Figure 5.31 shows that the normal stress along the interface becomes zero along a zone of 22m, starting at the inner toe. The shear stress in the interface at the start of sliding zone (around 3m at the left-hand side of the toe) is around 14 kPa, which corresponds to the critical cohesion value of 14 kPa. Figure 5.32 shows the effect of bending on the horizontal stresses in the cover layer, as well as the exceedance of the tensile strength of 3 kPa at the inner toe.

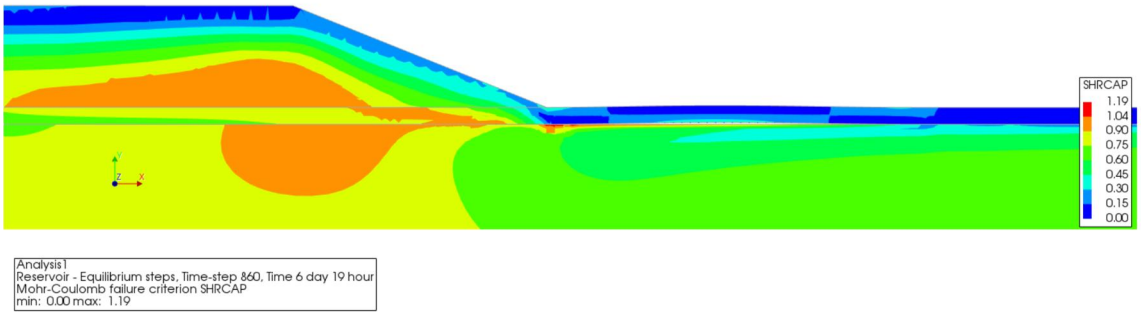

Figure 5.30. Mobilized shear strength ratio at failure (6 days and 19 hours)

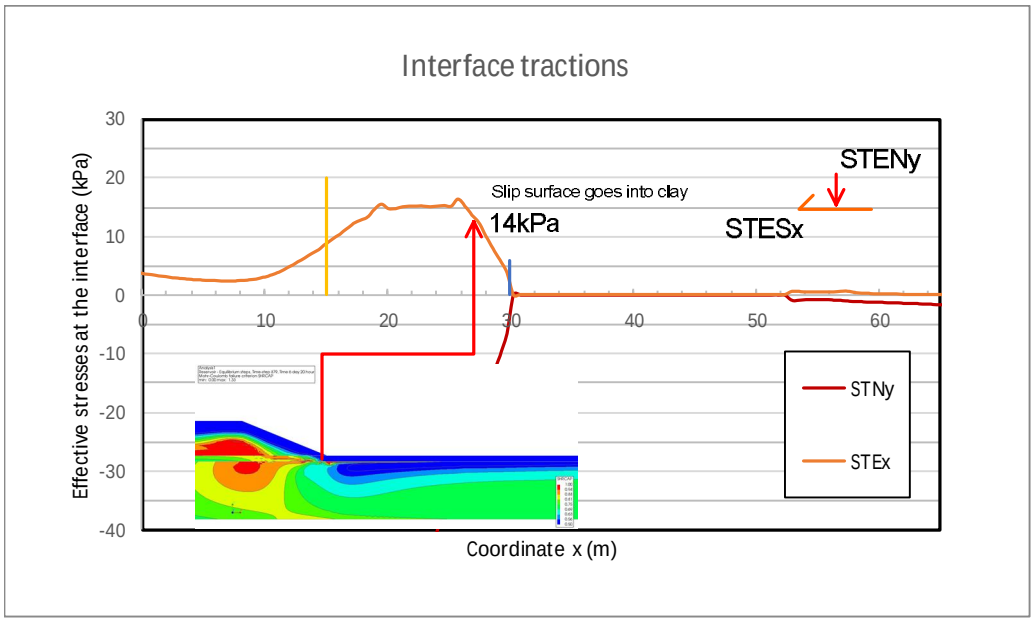

Figure 5.31. Tractions (effective normal and shear stress) along the interface between sand and clay cover-layer at time of failure (6 days and 20 hours.)

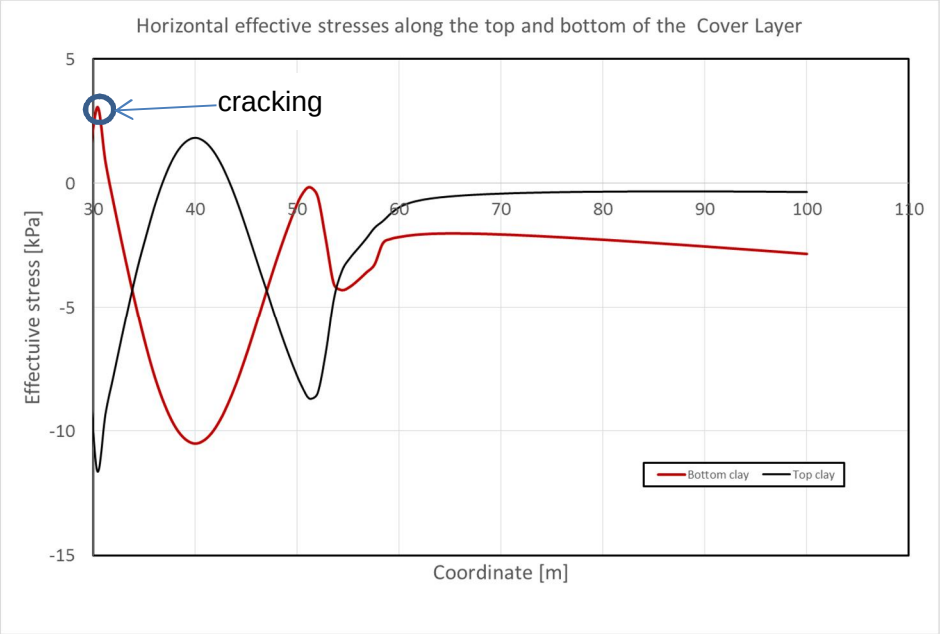

Figure 5.32. Horizontal effective stress along the top and bottom of the cover layer at time of failure, showing the effect of bending. Cracking starts to occur at the inner toe (X=30m), bottom side

Evolution of effective vertical stresses is shown in Figure 5.33 for three points located at the top of the sand layer in a zone close to the toe of the embankment. The opening of the interface is produced at day 5 and 20 hours which corresponds to the time where both the horizontal and vertical displacements start to increase.

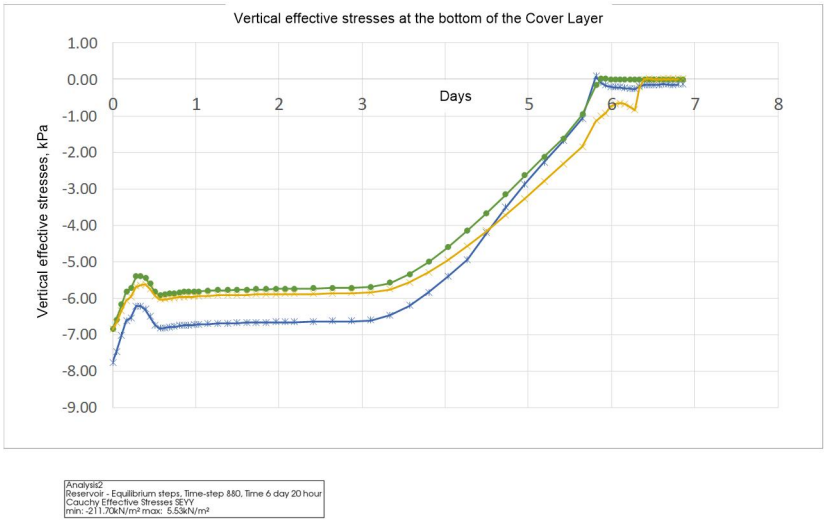

Figure 5.33.Development of the vertical effective stress in three points at the top of the sand layer from the start of the analysis until failure

5.4.7 Global forces

Figure 5.34 shows the temporal evolution of axial force N, bending moment M and eccentricity value e. The axial force increases from day 4 to day 6. After opening of the interface at day 6, the bending moment and eccentricity increase suddenly, while the normal forces decreases slightly.

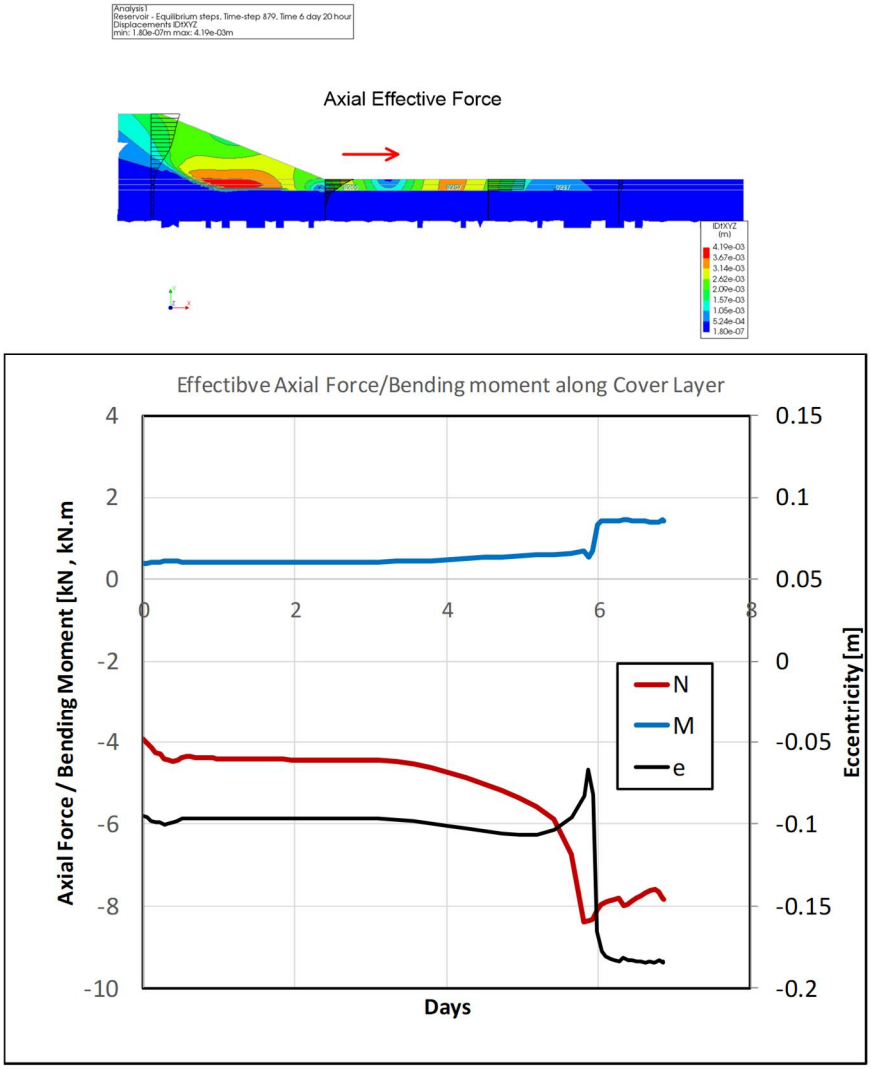

Figure 5.34.Evolution of the effective axial force (negative in compression) and bending moment in the clay layer at the toe of embankment

5.5 Comparison between results from Finite Elements and Limit Equilibrium

The “critical cohesion value” resulting from the Finite Element Analysis (FEA) can be compared to the critical values resulting from Limit Equilibrium Analysis (LEA). The latter values were provided by Deltares and differentiate between a critical value when including the cover layer strength (lower bound) and a critical value when not including the cover layer strength (upper bound). The FEA values for the computed head at the toe at failure can furthermore be compared to the values of the critical piezometric head (ϕ_{critical}). Apparently, both type 4 failure (compression with a thickness equal to 2 and 3 m) and type 3 failure (bucking with a thickness of 1 m) limit the strength contribution of the cover layer.

Table 5.4 summarizes the result of this comparison. It can be observed from this table that failure in FEA occurs when the piezometric head is equal to the critical value. The critical cohesion value from the FEA is between the upper and lower bound of the LEA (for a layer thickness of 2 m close

to the upper value, for a layer thickness of 1m and 3 m approximately in the middle). Apparently, both type 4 failure (compression with a thickness equal to 2 and 3 m) and type 3 failure (bucking with a thickness of 1 m) limit the strength contribution of the cover layer.

Table 5.4 . Comparison of the critical cohesion from LEA and FEA

Cover Layer thickness (m)	FEA (DIANA)				LEA (D-Geo Stability)			
	Piezometric head at failure (m) @x=30m	c (kPa)	ϕ(°)	Mode	Critical piezometric head	c (kPa)		ϕ°
						without cover layer contribution	with cover layer contribution	
3	2.27	17.5	3	4	2.20	20	15.1	3
2	1.43	16.5	3	4	1.47	16.8	13.8	3
1	0.79	14	3	3	0.73	15.1	13.1	3

6 Results from a sensitivity analysis

6.1 Introduction

In addition to the three basic cases with cover layer thickness of 1m (Case 1), 2m (Case 2) and 3m (Case 3), a series of additional analyses has been performed, as far as possible within the project constraints. In these analyses, one single parameter was varied at a time. Variations were done for models with a thickness of the cover layer of 1m, 2m and 3m. Variations were defined according to the following guidelines:

- For the (single) base case: show the effect of a lower and higher stiffness of the cover layer:

Scenario	E (kN/m^2)
A	1000
Reference	3000
B	10000

- For a strength/thickness combination with significant uplift: show the effect of a lower sand permeability/thickness:

Scenario	Sand thickness (m)	k (m/s)
Reference	10	1e-3
a	2	1e-3
b	10	1e-5
c	2	1e-5

Results are presented in the following section for the relevant cases. Table 6.1 presents an overview of the studied cases. The cases are named with a number defined in correspondence with the cover layer thickness and a letter for identification.

Table 6.1 List of cases. Case 3A, 2A and 1A refer to the reference cases

LIST OF CASES							
Name	CL	Description					Comments
		Clay materials			Sand		
		Cohesion [kPa]	ϕi	E [Mpa]	Thickness	Ksand [m/s]	
Case 2A	2	16.5	3	3	10	1.00E-03	
Case 2B	2	15.5	3	10	10	1.00E-03	
Case 2C	2	16.5	3	1	10	1.00E-03	Fails during embankment construction. Not reported in excel
Case 2D	2	20	3	3	10	1.00E-03	Failure do not occurs. Not reported in Excel
Case 2E	2	18	3	3	10	1.00E-03	
Case 2F	2	16.5	3	3	2	1.00E-03	
Case 2G	2	16.5	3	3	2	1.00E-05	
Case 2H	2	16.5	3	3	10	1.00E-05	
Case 1A	1	14	3	3	10	1.00E-03	
Case 1B	1	14	3	3	2	1.00E-03	Not reported in excel
Case 1C	1	14	3	3	2	1.00E-05	
Case 3A	3	17.5	3	3	10	1.00E-03	
Case 3B	3	20	3	3	10	1.00E-03	
Case 3C	3	17.5	3	10	10	1.00E-03	
Case 3D	3	16.5	3	10	10	1.00E-03	

The detailed results of all cases are contained in MS-Excel files, which are delivered together with this report.

6.2 Effect of a clay stiffness increase

6.2.1 Cover layer thickness of 3m

Increasing the clay stiffness from 3 MPa to 10MPa and keeping the clay cohesion value constant at 17,5 kPa (case 3C) changes the deformation behaviour of the cover layer with thickness 3m from type 4 (compression) to type 2 (uplift), without showing progressive buckling failure and slope instability. Uplift occurs from approximately 11 days to approximately 21 days. The maximum vertical displacement of the cover layer in the middle of the uplift zone (0,17m) is found at 16 days and 14 hours. The uplift zone runs at that time from x=30 (toe) to x=80m. Cracking occurs at that time both at the toe (bottom side) and in the middle of the uplift zone (top side). An additional reduction of the cohesion to 16,5 kPa (case 3D) yields a similar result (temporary uplift and cracking, but no progressive buckling failure and slope instability). Further reduction would probably have yielded slope instability in combination with buckling/cracking of the cover layer, but this has not been investigated within the scope of the project.

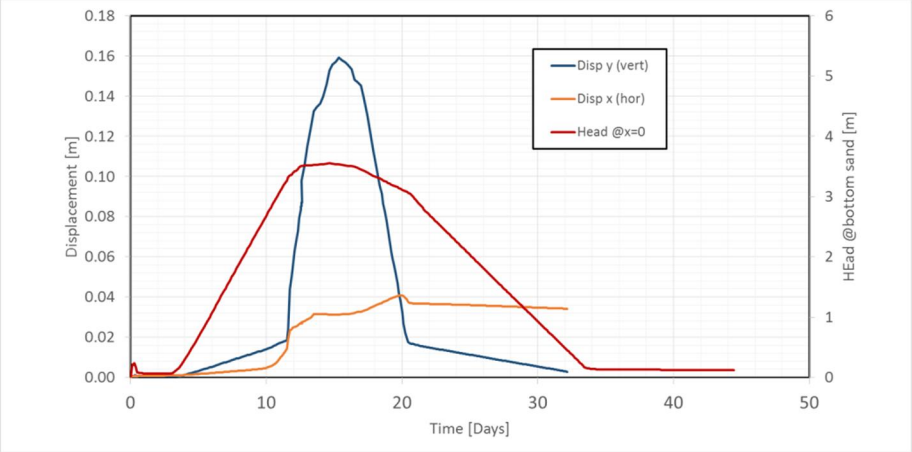

Figure 6.1 Temporal evolution of the vertical and horizontal displacement of a point on the cover layer in the middle of the uplift zone, together with the evolution of the head computed in the sand layer at x=0 m

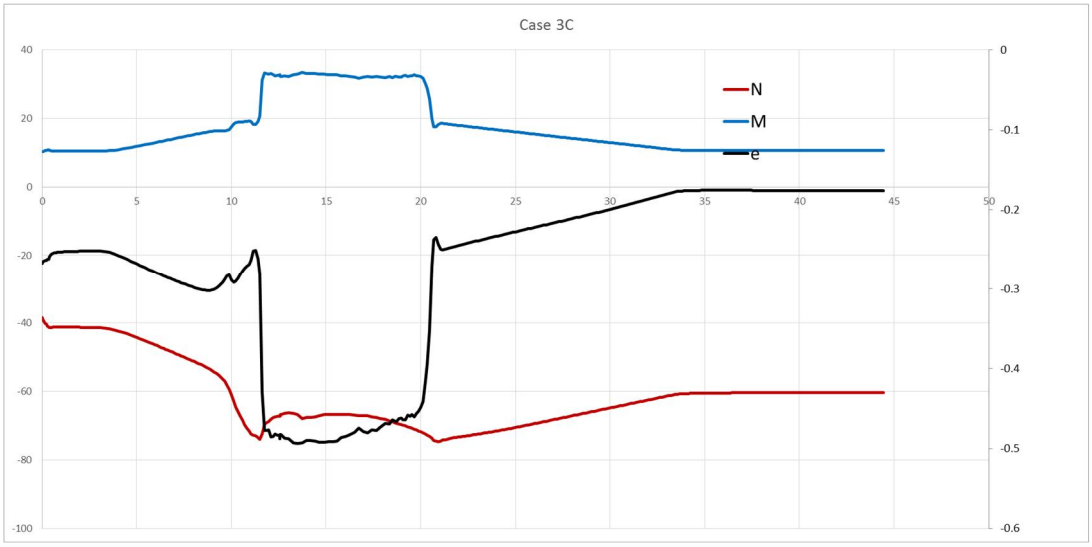

Figure 6.2 Temporal evolution of the normal force (N), Moment (M) and eccentricity (e) at the inner toe. Sudden changes occur at the start of uplift (11 days)

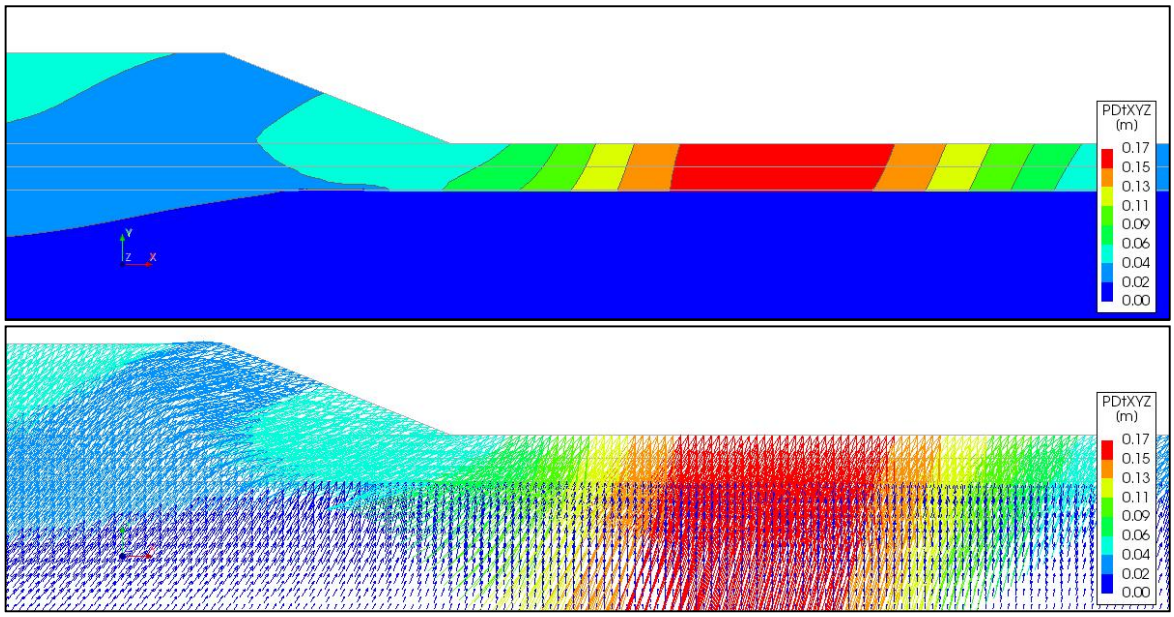

Figure 6.3 Contour plot and vector plot of the total vertical displacements at 16 days and 14 hours

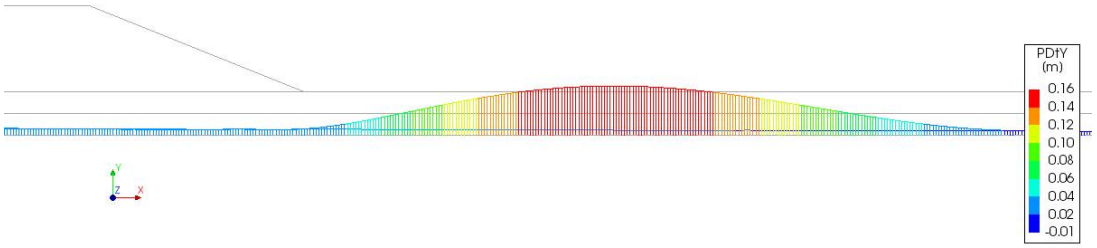

Figure 6.4 Gap opening along the interface at 16 days and 14 hours

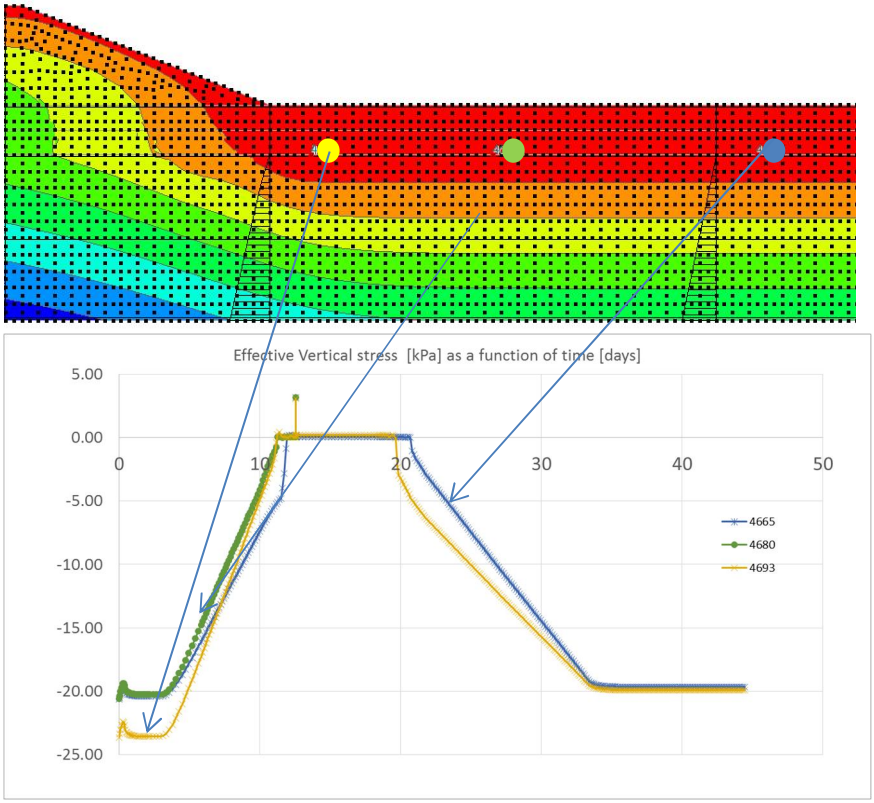

Figure 6.5 Temporal evolution of the vertical effective stress in three points on the top of the sand layer

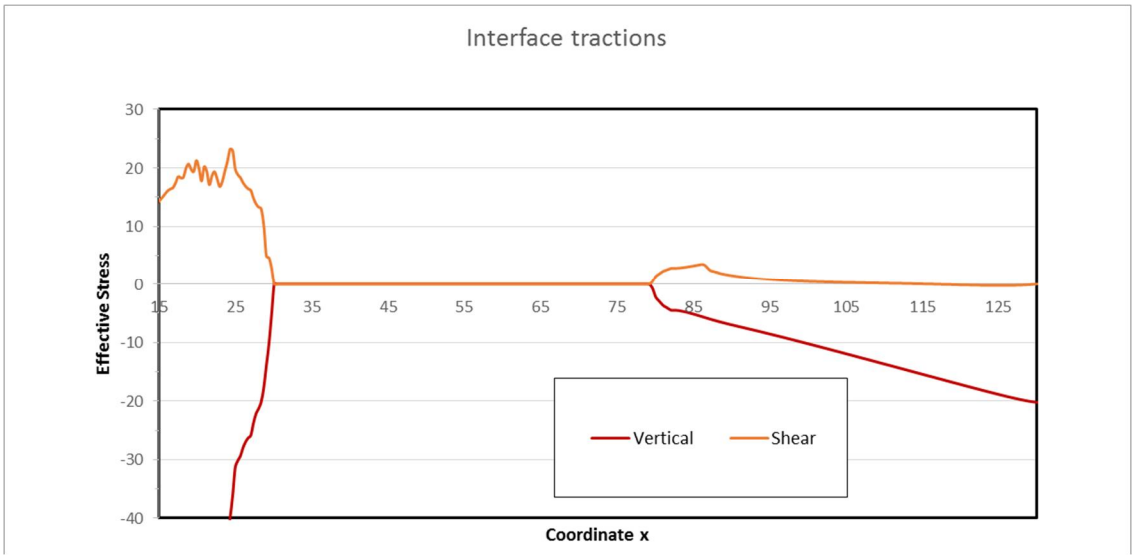

Figure 6.6 Effective vertical stress and shear stress along the interface at 16 days and 14 hours

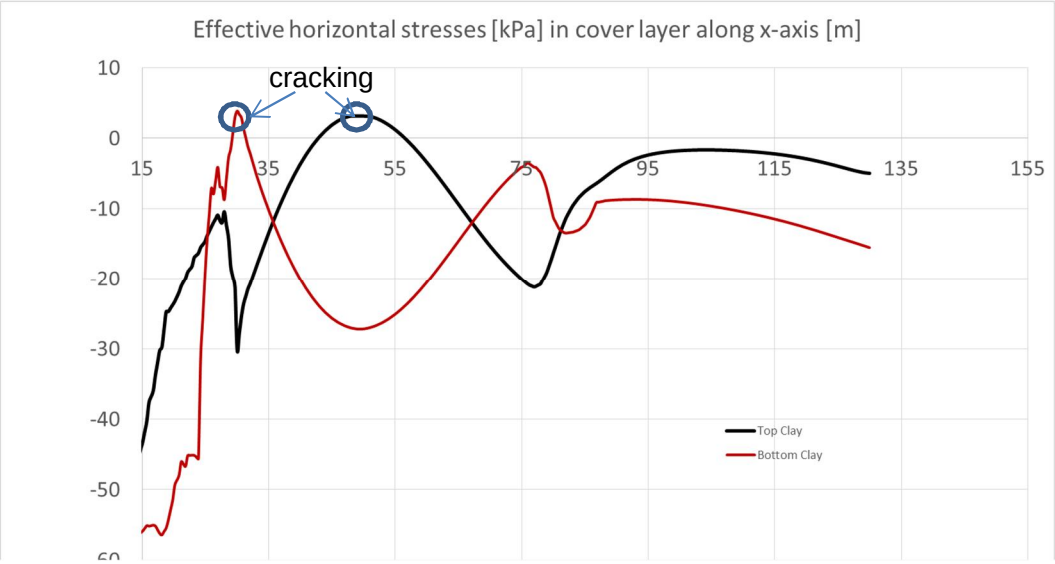

Figure 6.7 Horizontal effective stresses along the top and bottom of the cover layer at 16 days and 14 hours

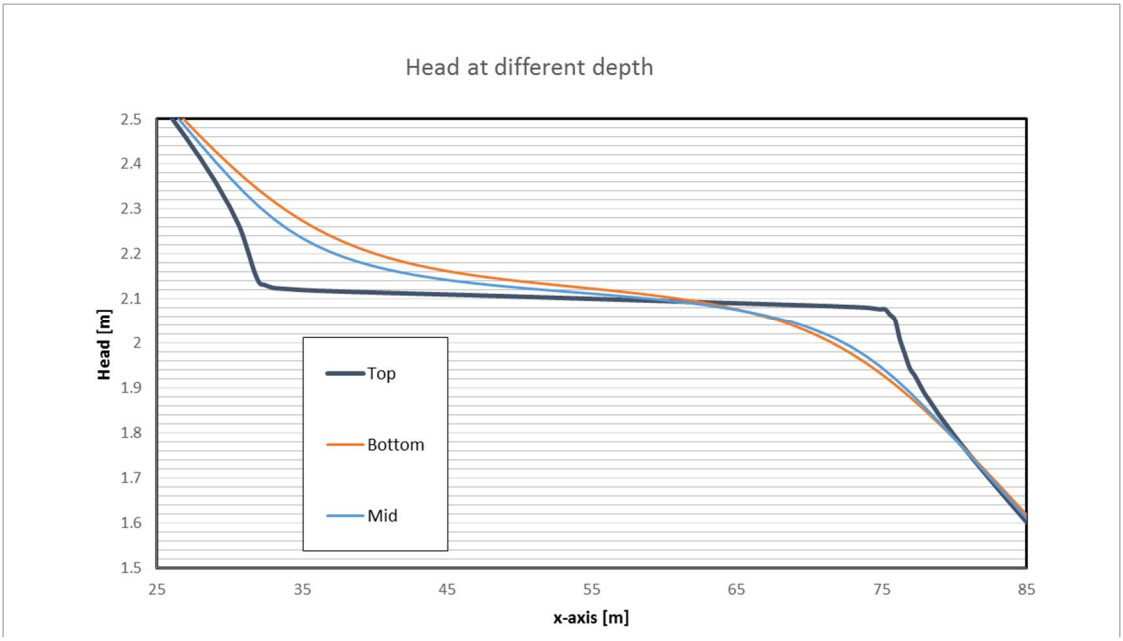

Figure 6.8 Distribution of the piezometric head in the sand layer (top, middle and bottom) along the x-axis, at 16 days and 14 hours

6.2.2 Cover layer thickness of 2 m

After increasing the clay stiffness from 3 MPa to 10 MPa, failure is no longer observed for the case of a cover layer with a thickness of 2m and a clay cohesion value of 16,5 kPA. Additionally reducing the clay cohesion value to 15,5 kPa (case 2B) yields again failure at 9 days. The failure mode resembles mostly type 4 (compression), when looking at the direction of the incremental displacements at failure. At failure are zero effective vertical stresses observed in the interface, in a zone from closely behind the toe (x=30 m) to approximately x=58m. The pore pressure field is also affected by the relatively small gap in that zone, but no significant bending is observed.

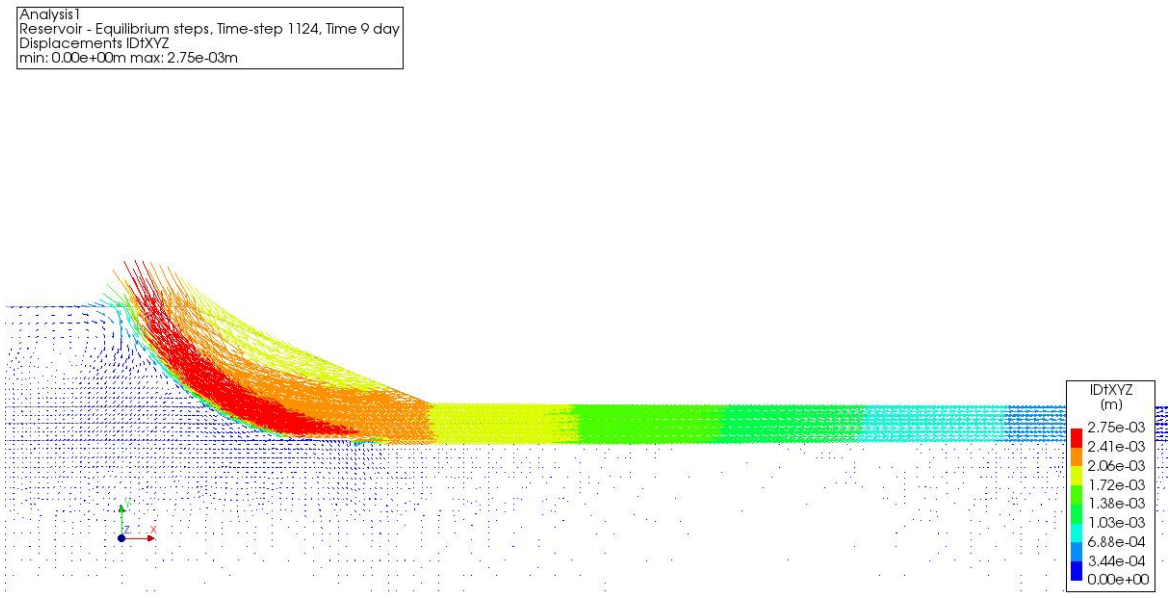

Figure 6.9 Incremental displacements at failure (9 days)

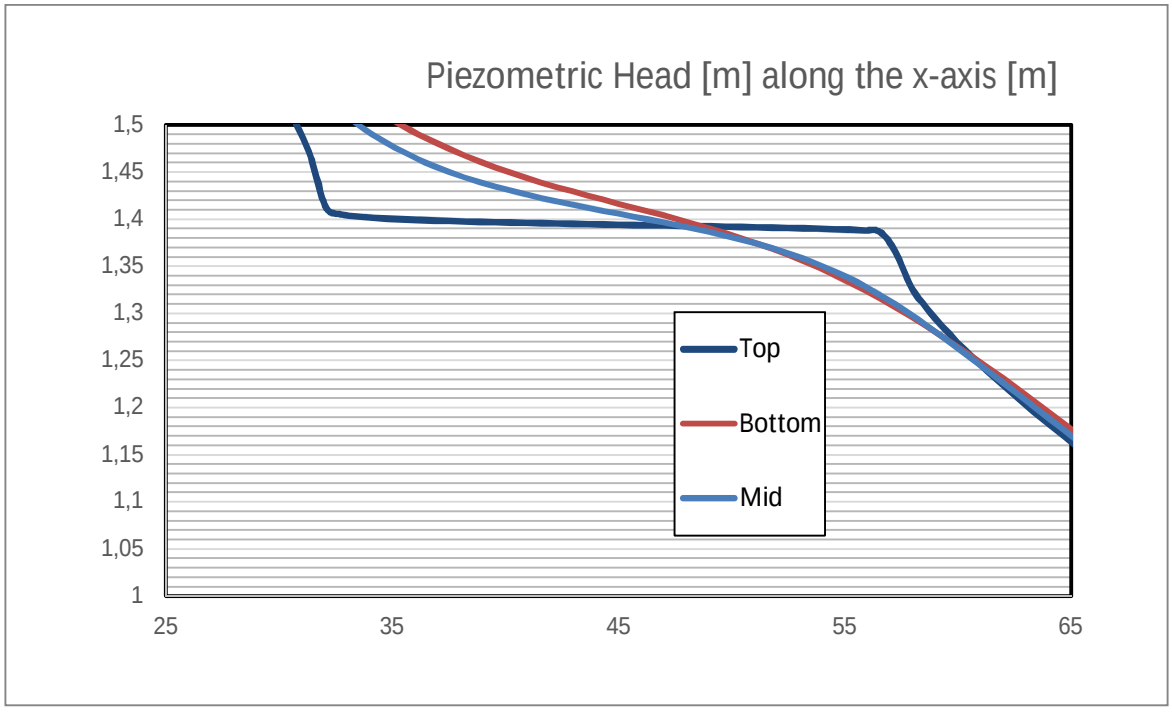

Figure 6.10 Piezometric head in the sand layer along the x–axis for different vertical levels, at failure

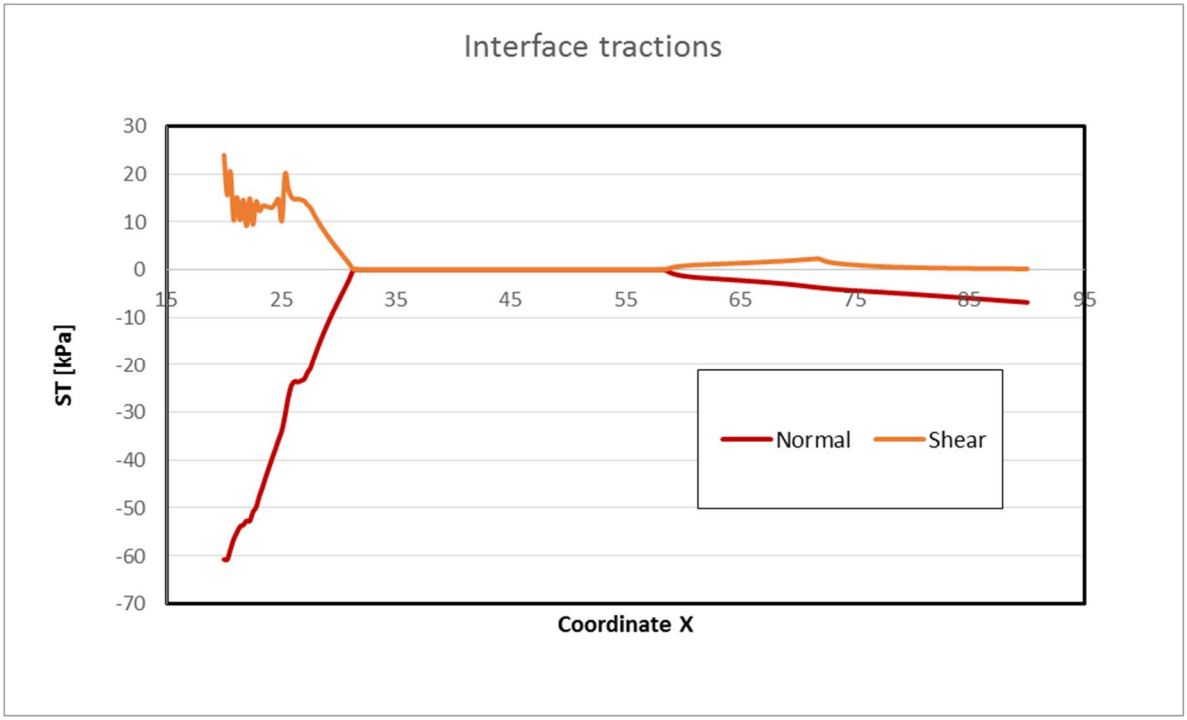

Figure 6.11 Effective vertical stress and shear stress along the interface at failure

6.3 Effect of lowering the cover layer stiffness

If the clay stiffness is reduced from 3 kPa to 1kPa, numerical instable behavior occurs already during embankment construction. This happens for a cover layer thickness of 3m (and clay cohesion value of 17,5 kPa), as well as for a cover layer thickness of 2 kPa (and clay cohesion value of 16,5 kPa). The causes and potential solutions for this behavior have not been investigated further within the scope of the present study.

6.4 Effect of sand layer thickness variation

Reduction of the sand layer thickness from 10m to 2m yields no major differences in case of a cover layer thickness of 2m. Results of the same reduction for a cover layer of 1m are shown below. Failure occurs in this case at 9 days and 5 hours. The smaller sand thickness reduces the hydraulic transmissivity with a factor 5, which leads to a more nonlinear horizontal gradient of the piezometric head under the embankment after gap opening, and therefore to a larger value of the head at x=0 at failure. Uplift, bending and cracking still occurs. The incremental displacements at failure shows however not (yet) a pattern that can be associated with buckling. This might be caused by the transmissivity reduction in the sand, which constrains the flow rate and therefore also the gap growth.

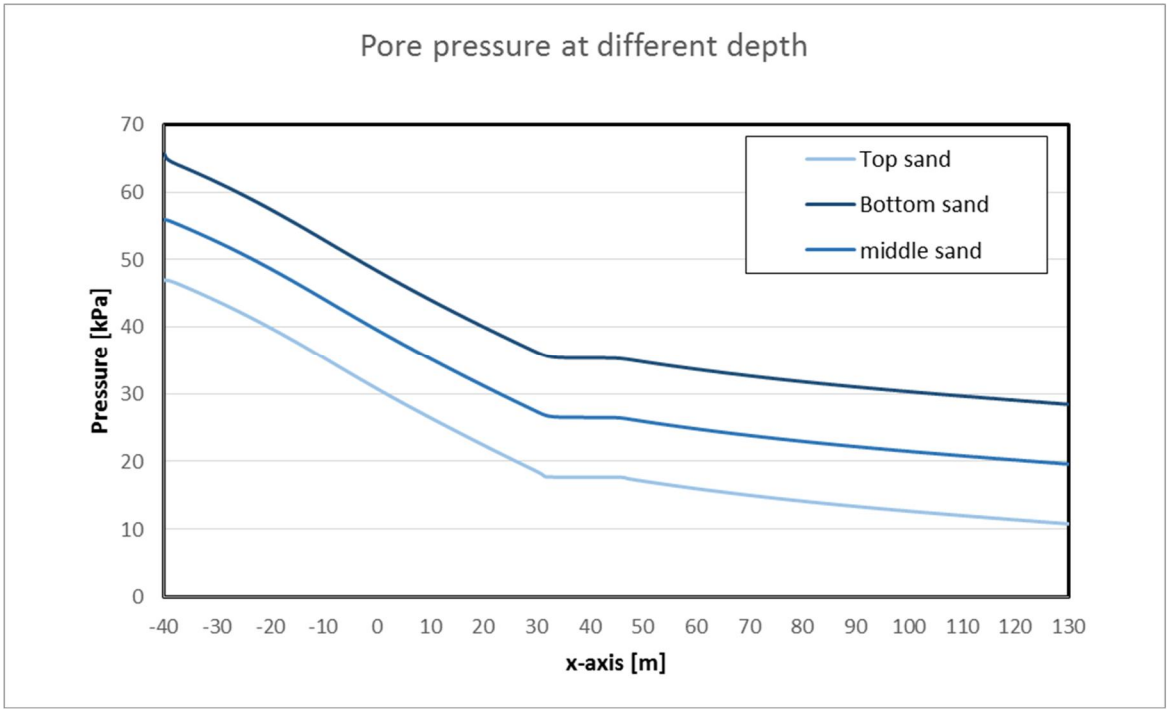

Figure 6.12 Pore pressure at top, middle and bottom of the sand layer

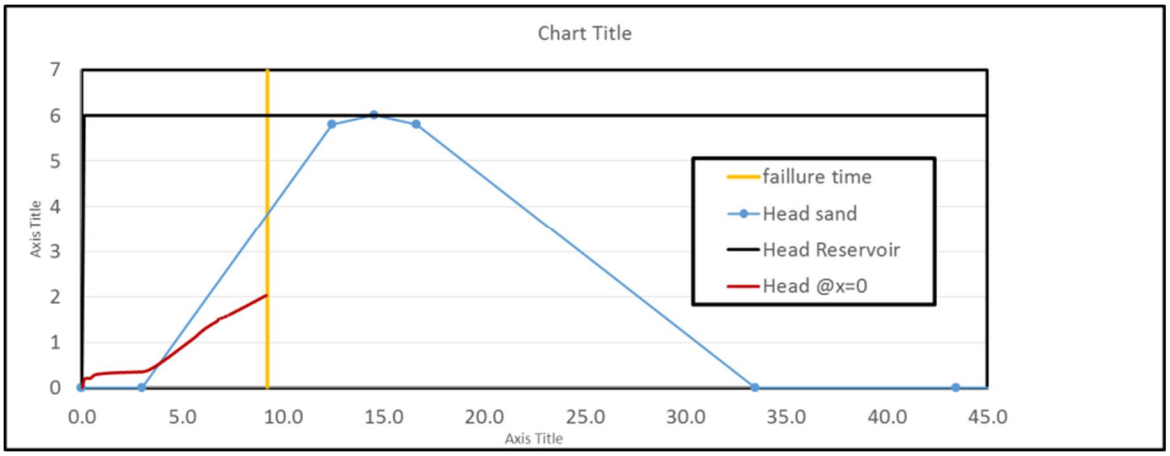

Figure 6.13 Piezometric head variation at the reservoir and in the sand layer. The latter at the left-hand side (x=-40m) and at the embankment axis (x=0)

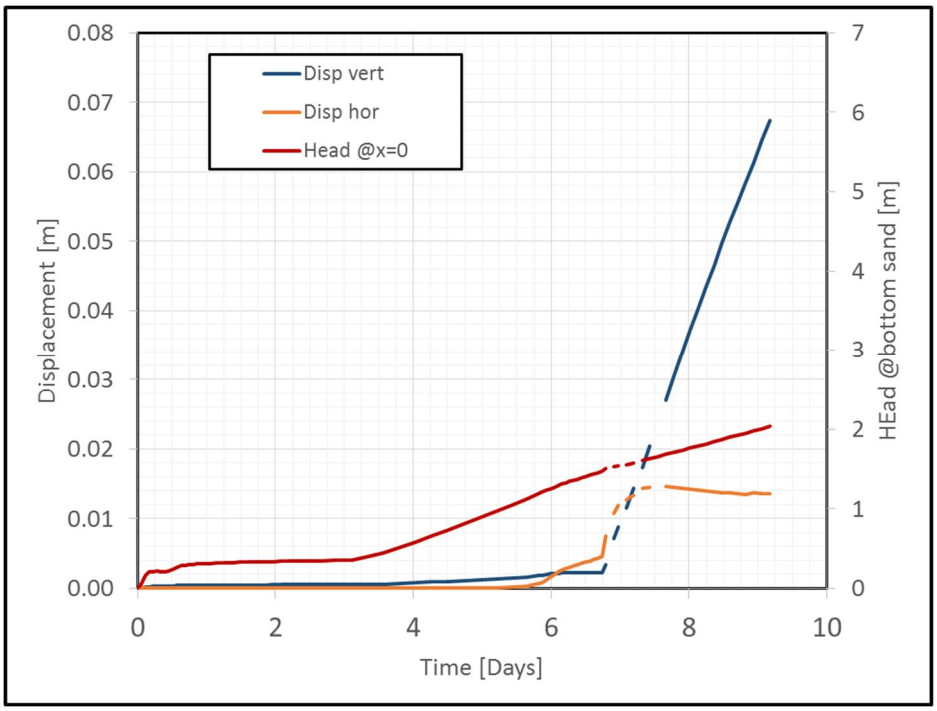

Figure 6.14 Temporal evolution of the horizontal and vertical displacement of a point on the cover layer in the middle of uplift zone, together with the piezometric head in the sand layer at x=0

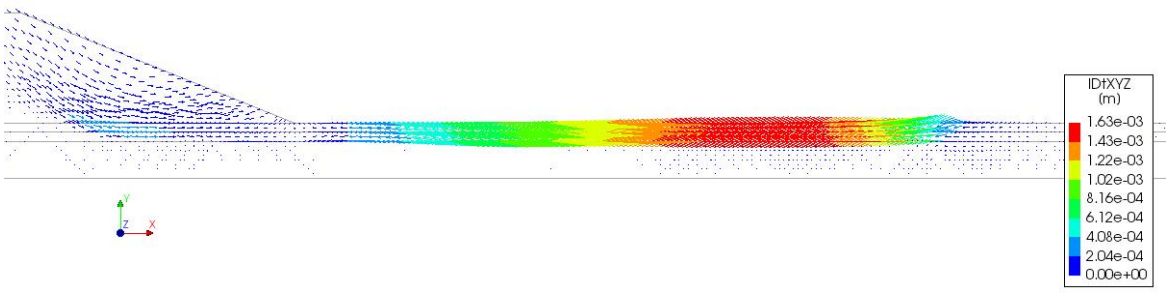

Figure 6.15 Incremental displacements at failure (9 days and 5 hours)

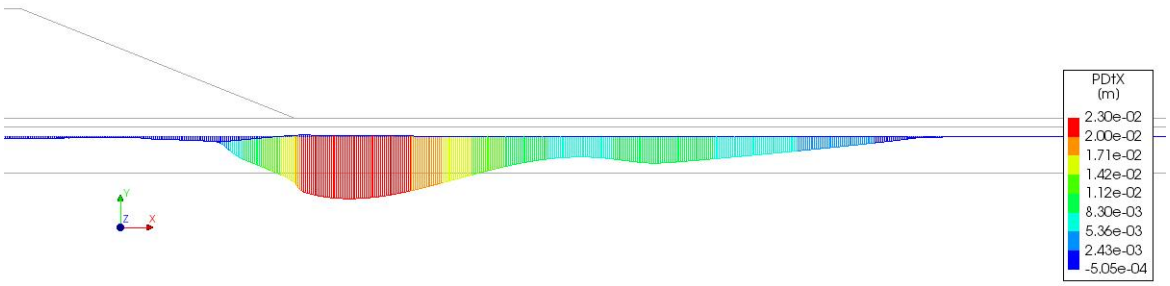

Figure 6.16 Relative slip displacements along the interface at failure (9 days and 5 hours)

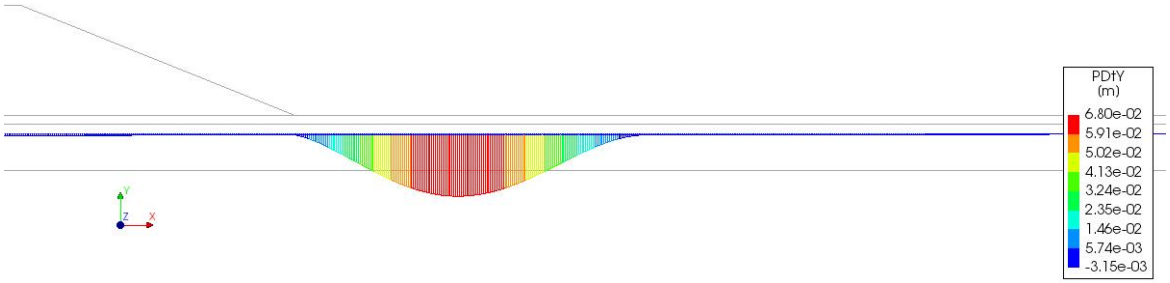

Figure 6.17 Gap opening along the interface at failure

6.5 Effect of permeability reduction

The effect of lowering the sand permeability from 1e-3 to 1e-5m/s was studied considering a cover layer thickness of 2 m, combined with a sand layer thickness of 10m and 2m. The pore pressure distribution along the x-axis becomes nonlinear when reducing the transmissivity with a factor 100. This nonlinearity increases further when reducing the sand thickness additionally. In both cases, the nonlinear behavior reduces the maximum value of the piezometric head at the toe such, that zero effective vertical stresses at the interface do not occur any more for the considered transient hydraulic boundary conditions. Therefore, no slope instability is observed any more.

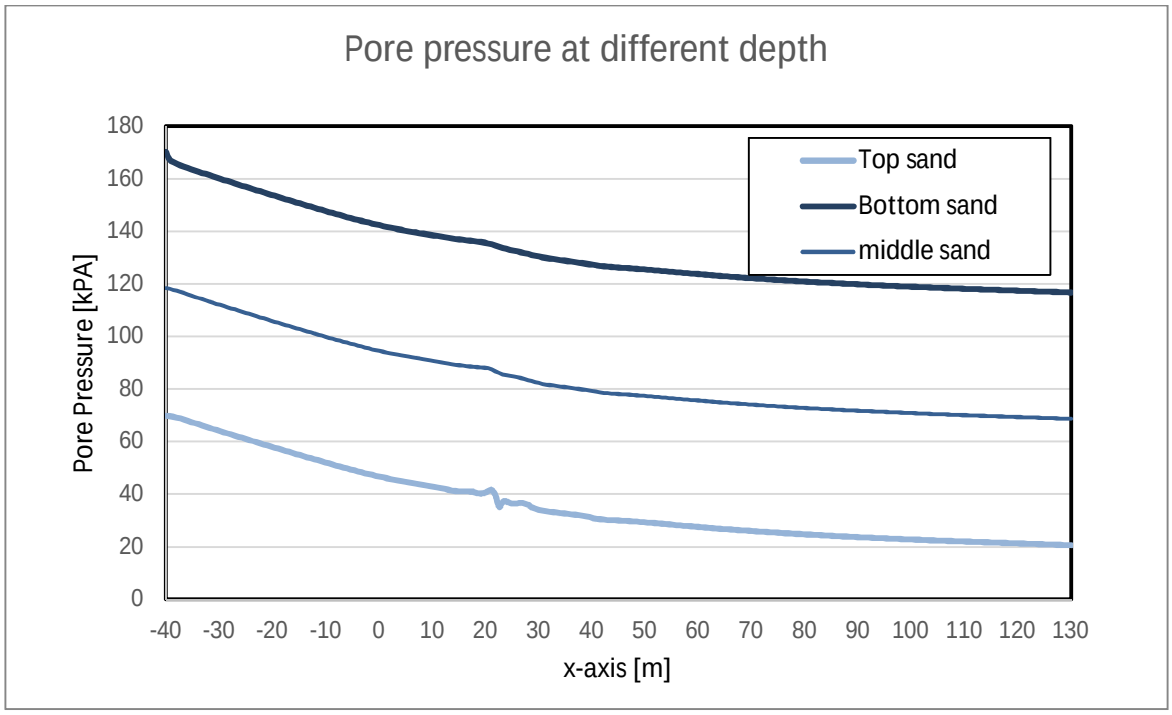

Figure 6.18 Pore pressure at top, middle and bottom of the sand layer for a reduced permeability of 1e-5m/s and a sand layer thickness equal to 10 m

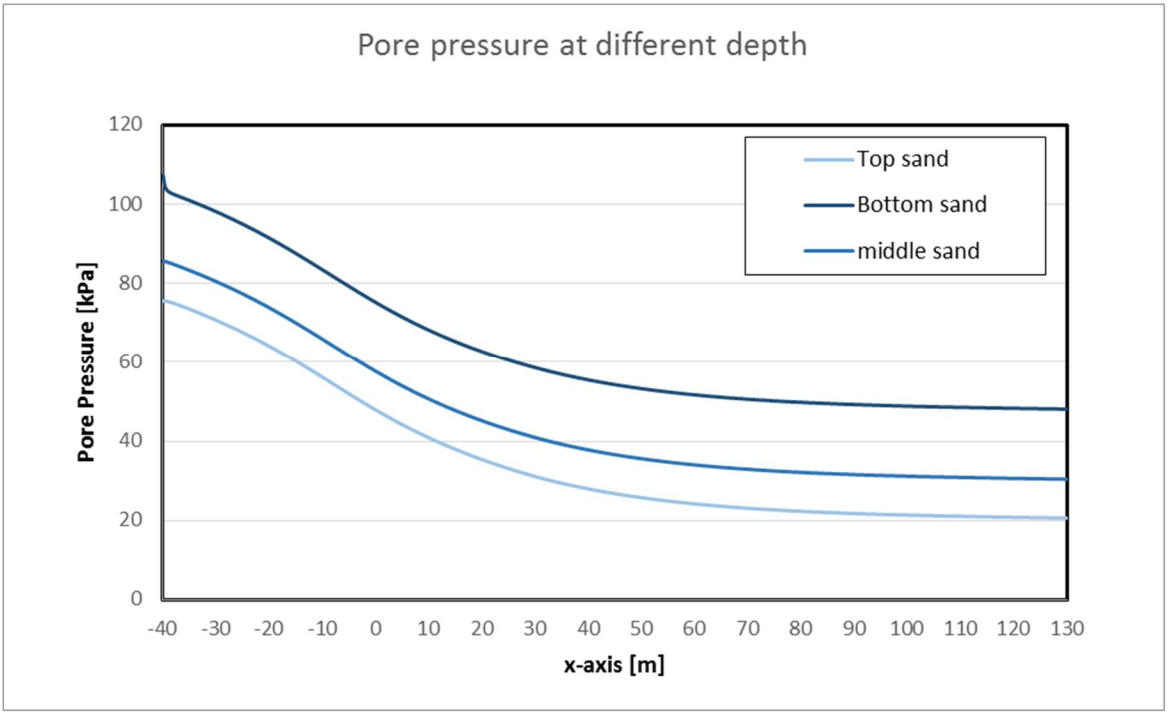

Figure 6.19 Pore pressure at top, middle and bottom of the sand layer for a reduced permeability of 1e-5m/s and a sand layer thickness equal to 2 m

7 Conclusions and recommendations

The results of the reported study can be summarized as follows.

- The reported study is based on a simplified case, consisting of a clay embankment on a clay cover layer, resting in turn on a sand layer.

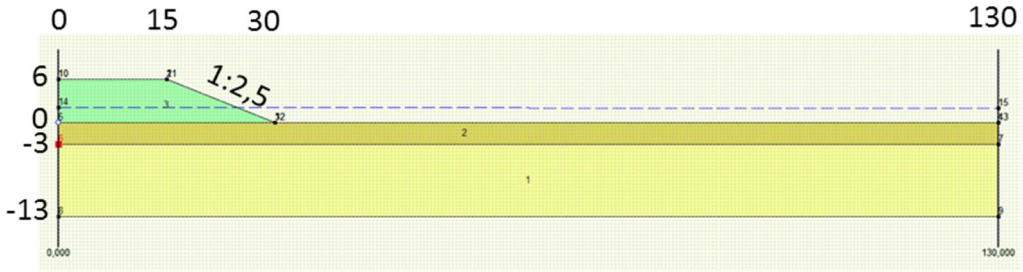

- A “proof of concept” has shown that it is feasible to model for this simplified case the occurrence of uplift and its influence on the pore pressures and slope stability, with inclusion of the effect of geometrically nonlinear displacement of the cover layer and with inclusion of the effect of cracking. The type 3 and type 4 modes as depicted below could both be reproduced.

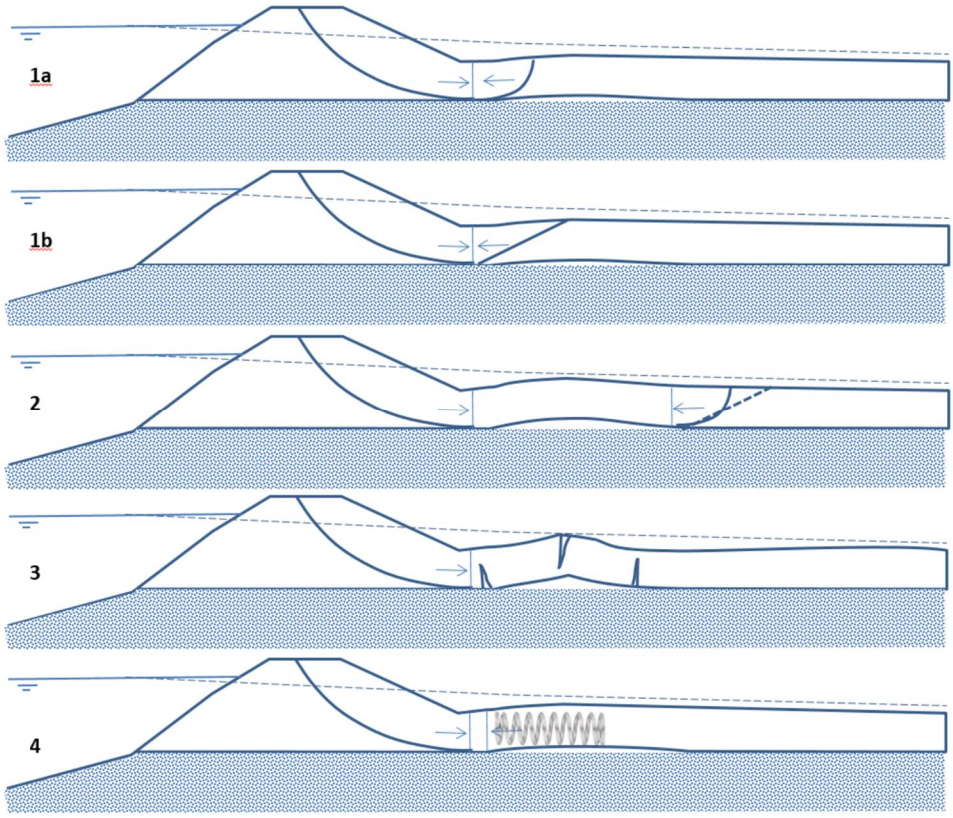

This has been achieved by using a coupled flow-stress formulation, in which an open state of the interface between the cover layer and the sand influences the hydraulic field by water

storage and by a “horizontal hydraulic shortcut”. The clay in the cover layer has been modelled with undrained shear strength, while limiting the tensile strength conservatively, using an additional multidirectional crack model.

- For all thicknesses, failure occurred when the critical piezoemetric head at the toe was close to the theoretical one.
- Variation of the cover layer thicknesses for a clay stiffness of 3 MPa shows that slope instability is numerically initiated at a certain “critical clay cohesion value”, after the preceding occurrence of zero stresses along the interface between cover layer and sand. In case of a cover layer thickness of 3m and 2m, the slope instability is initiated by elastic compression of the cover layer (type 4). In case of a cover layer thickness of 1m, the slope instability is initiated by buckling and cracking of the cover layer (type 3). The values of the critical clay cohesion from Finite Element Analyses (FEA) are in all cases between the upper and lower bound values following from Limit Equilibrium Analysis (LEA). The upper bound has been determined by ignoring the cover layer strength contribution. The lower bound has been determined by including the cover layer strength contribution. In case of a cover layer thickness of 2m, the critical cohesion value from FEA is close to the upper bound. For the layer thickness of 1m and 3m, the critical cohesion value is approximately in the middle between the upper and lower bound.
- Increasing the cover layer stiffness from 3 MPa to 10 MPa improves the stability. In case of a cover layer thickness of 2m, the cohesion can be reduced from 16,5 to 15,5 kPa, before type 4 failure occurs again. In case of a cover layer thickness of 3m, failure has not been observed when reducing the cohesion value from 17,5 kPa to 16,5 kPA, though temporary uplift, bending and cracking did occur.
- Reducing the sand layer thickness from 10m to 2m reduces the transmissivity with a factor 5. Uplift and failure still occurs in this case. In case of a cover layer thickness of 1m however, the observed failure mode is no longer a clear type 3 (buckling and cracking).
- Reducing the sand permeability from 1e-3 to 1e-5m/s yields a more nonlinear horizontal distribution of the piezometric head in the sand, as the transmissivity is reduced with a factor 100. This results in more damping at the toe, preventing uplift to occur.

It should be noticed that in this study no purely passive shear failure in the cover layer has been observed (type 1 or type 2). The numerical results suggest that a type 4 failure mode by compression deformation can occur already at quite large cover thicknesses, in combination with a low clay stiffness. In this study, the type 3 initialization by buckling/cracking occurred only for a small cover layer thickness, a low clay stiffness and a thick sand layer with high permeability.

Regarding the decision rule, it seems debatable that the cover layer strength is reduced abruptly to zero if the uplift safety factor is between 1,2 and 1. Especially because the LEA schematization of cover layer thickness and the piezometric head distribution in the sand layer should be conservative already.

As soon as the uplift safety factor becomes 1, the FEA results show that the equivalent residual strength of the cover layer in the decision rule should not only mimic the effect of a type 3 failure mode, but also the effect of a type 4 mode, as the latter is dominant in most cases. The results show that the critical cohesion value for both modes is found between the upper bound and the lower bound from LEA, moving more to the upper bound when the clay stiffness decreases. Completely ignoring the strength contribution of the cover layer in case of uplift, as in the current decision rule, is therefore on the safe side. However, this study is not conclusive to what extend the current decision rule is on the safe side. The current results are too limited for that purpose and also not supported by physical evidence.

Modification of the decision rule by reduction of the critical thickness or the amount of strength reduction below the critical thickness can therefore not be supported sufficiently by the current results. The results do show however the potential of numerical analysis to gain more understanding and to underpin the final choices for the critical thickness and the equivalent residual strength in the near future. Further sensitivity analysis is recommended for this purpose, as well as further variation studies using more realistic geometries and soil layering, and also using a more sophisticated constitutive model for the clay.

If results from further numerical analyses would show a clear potential for less conservative choices, it is finally also recommended to compare the numerical results with the results from a physical test set-up, in order to understand to which extend they correspond or differ.

Bibliography

Ávila, G. (2004). *Study on the cracking behavior of clay. Application to Bogota Clay. Ph.D. thesis, TU of Catalonia.*

Deltares. (2017). *Base Case Definition, Deltares memo.*

DIANA FEA. (2017). *DIANA User's Manual, Release 10.2.*

Ministerie van Infrastructuur en Milieu. (2016b). *Schematiseringshandleiding Macrostabiliteit, WBI 2017, versie 2.1.*

Tang, C.-S., Pei, X.-J., Wang, D.-Y., Shi, B., & Li, J. (2015). Tensile Strength of Compacted Clayey Soil. *J. Geotech. Geoenviron. Eng. 2015.141*.